NANYANG
TECHNOLOGICAL
UNIVERSITY

Shape Memory Hybrids: Mechanism and Design for Tailored Properties

Ding Zhen

School of Mechanical and Aerospace Engineering
Nanyang Technological University

2012

Shape Memory Hybrids: Mechanism and Design for Tailored Properties

Ding Zhen

School of Mechanical and Aerospace Engineering

A thesis submitted to the Nanyang Technological University
in partial fulfillment of the requirement for the degree of
Doctor of Philosophy

2012

Abstract

The concept of shape memory hybrid (SMH) is proposed. The underlying mechanism and performance are investigated. The flexibility and versatile in design and fabrication of SMHs with tailored properties are demonstrated in a silicone based system.

All types of shape memory phenomena, namely dual-shape memory effect (SME), triple-SME, and mechanical two-way SME, which are most likely found separately in some individual existing shape memory materials (SMMs), but not all in one material, are reproduced in SMHs made of silicone-paraffin wax (S-PW). The underlying mechanisms behind all these phenomena are revealed in details. In addition, the performance of S-PW SMHs is systematically characterized.

Multiple-stimuli-responsive SME is achieved in a silicone-sodium acetate trihydrate (S-SAT) SMH, which is not only thermo-responsive and water-responsive, but also pressure-responsive. The last shape memory feature has never been realized in any existing SMMs. Beside the ability for mechanical two-way actuation, shape fixation of S-SAT SMHs can also be quickly achieved by means of tapping.

Silicone and melting glue (S-MG) SMHs developed here are not only rubber-like at both high and low temperatures, but also have excellent SME and repeated instant self-healing function. It is proved that while micro sized MG inclusions play a part in the SME, tangled molecular chains of MG (and silicone) contribute to the rubber-like phenomenon and repeated instant self-healing function.

Based on the working principle of SMHs, electrically conductive SMHs which are suitable for joule heating and with over-heating protection function, SMHs with a narrow transition temperature range (within 4.5°C), impact-responsive SMHs, high temperature SMHs, and heating/cooling-responsive SMHs are developed.

This project presents a systematic study in design, fabrication and characterization of SMHs with tailored properties and features.

Keywords: shape memory hybrid; dual-SME; triple-SME; two-way reversible SME; Multiple-stimuli-responsive, rubber-like, self-healing, Joule heating.

Acknowledgements

First and foremost, I would like to express my warmest and deepest gratitude to my supervisor, Dr. Huang Wei Min, for his guidance, encouragements, patience and friendship. His keen insights and wide visions gave me a great help for understanding my project and gaining research skills. Working with him has been an invaluable and honorable experience during my graduate education.

I am also grateful to Mr. Zhao Yong, Dr. Wang Changchun, Mr. Wei Jun, Mr. Liew Kok Cherng, and Mr. Hendra Purnawali for their kind helps and beneficial discussions.

I would like to express my sincere gratitude to the technicians in CMMS, Mr. Cheo and Ms. Hali, for their assistance and kindness in various aspects. Technicians of Strength of Materials Lab, Materials Lab and Aerospace Lab are specially appreciated.

Finally, I thank my parents and my wife for their encouragement and patience. Without their unwavering support, it is impossible for me to start and finish my Ph.D. study.

Table of Contents

List of Figures

List of Tables

Abbreviations

BSEI	back-scattered electron imaging
CF	carbon fiber
CNT	carbon nano tube
CSP	copper sulphate pentahydrate
DMA	dynamic mechanical analysis
DSC	differential scanning calorimetry
EDS	energy-dispersive spectrometry
FTIR	Fourier transform infrared
GF	glass fiber
HRS	heat resistant sealant
HSP	heat-shrinkable polymer
LMPA	low melting point alloy
LMPW	low melting point wax
MG	melting glue
PDMS	polydimethyl siloxane
PTC	positive temperature coefficient
PW	paraffin wax
SAT	sodium acetate trihydrate
SCF	short carbon fiber
SCM	shape change material
SEI	second electron imaging
SEM	scanning electron microscope
SMA	shape memory alloy
SMc	shape memory composite

SMC	shape memory ceramic
SME	shape memory effect
SMH	shape memory hybrid
SMM	shape memory material
SMP	shape memory polymer
SRM	stimulus-responsive material
TGA	thermogravimetric analysis

Chapter 1 Introduction

1.1 Background

Shape memory materials (SMMs) are featured by the ability to recover their original shape from a significant and seemingly plastic deformation when a right stimulus is applied (Huang *et al.* 2010a). This is known as the shape memory effect (SME). Heat, light, electrical field, magnetic field, moisture, and solvent are some of such stimuli, among others (Buckley *et al.* 2006; Du and Zhang 2010; Huang *et al.* 2005; Lendlein *et al.* 2005; Liu *et al.* 2005; Razzaq *et al.* 2007). SMMs have been on the forefront of research in the last several decades and have been applied in a wide range of applications in various fields due to their attractive feature of the SME (Funakubo 1987; Huang *et al.* 2011; Miyazaki *et al.* 2009).

The SME has been observed in a few material systems. Technically speaking, SMMs are under the category of stimulus-responsive material (SRM, refer to Fig. 1.1). Depending on the exact type of response, a SRM may change its physical or chemical properties accordingly when the right stimulus is applied. If the response is in the form of shape change, and if such a change in shape is spontaneous and instant, this class of materials is called shape change material (SCM). A typical example of SCMs is piezo-electrical material (Haertling 1999). On the contrary, a SMM is able to maintain the temporary shape virtually forever, unless the right stimulus is applied to trigger the shape recovery (Aschwanden and Stemmer 2006; Lendlein 2010).

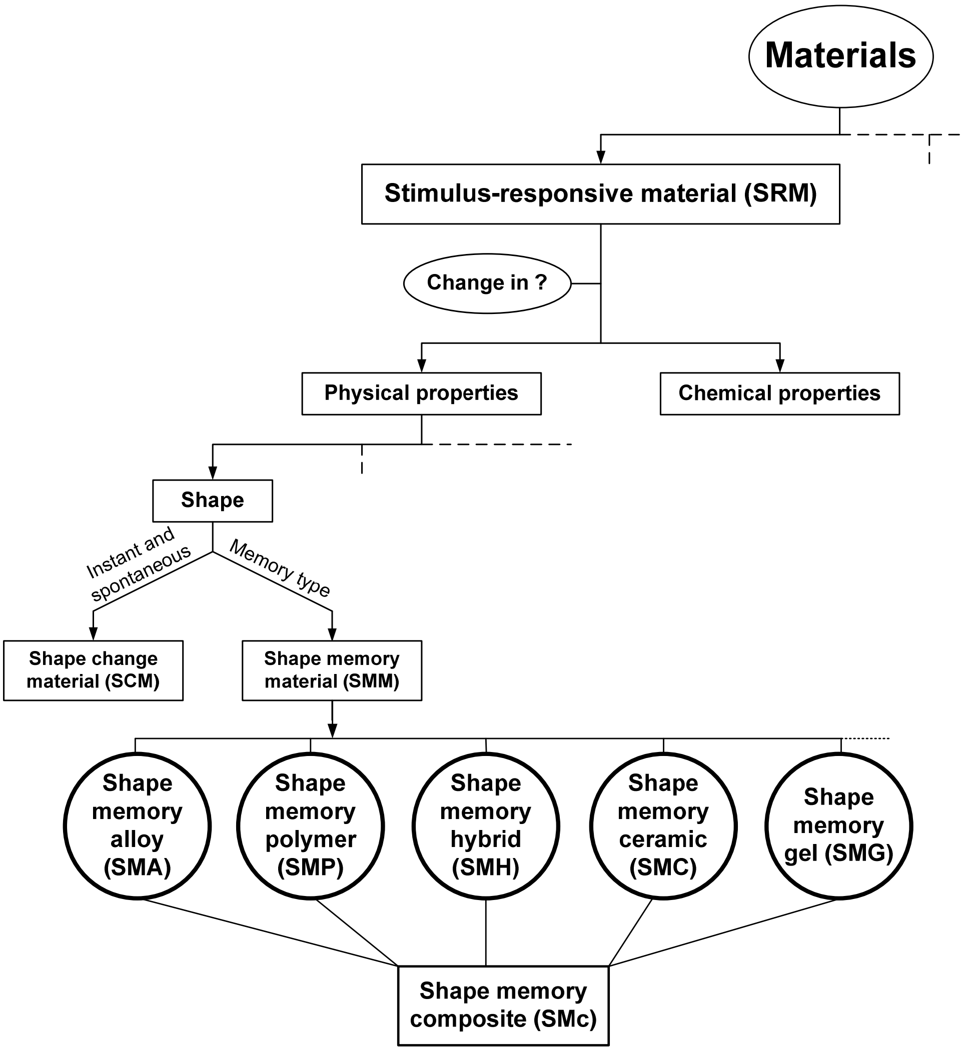

Figure 1.1 Various types of SMMs within the world of materials (Sun *et al.* 2012).

As illustrated in Fig. 1.2, from energy point of view, between two states A and B of a SRM, which is able to react to a particular stimulus by means of shape change, if the energy barrier (*H*) is high enough to prevent free and reversible transition between them, this is a SMM. Otherwise, it is a SCM.

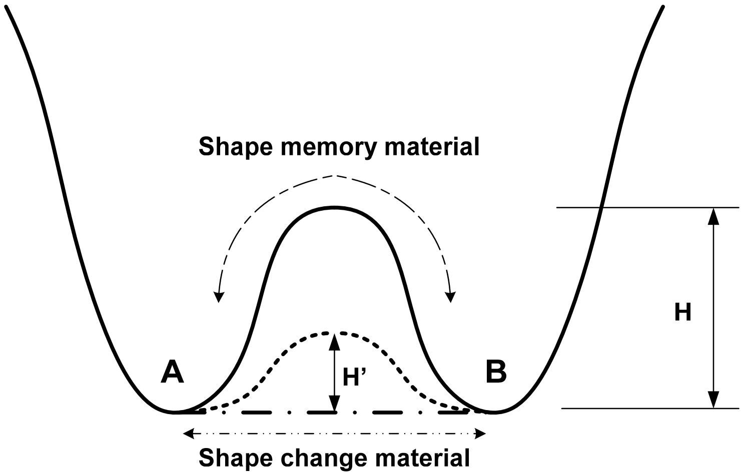

Figure 1.2 Illustration of energy in two states A and B of a material, where H and H’ indicate different levels of energy barrier.

Although the finding of SME in some alloys, namely shape memory alloys (SMAs), could trace well back to as early as 1932 in an gold-cadmium alloy (Chang and Read 1951), it did not attract much attention until 1971 when a significant recoverable strain was observed in a near-stoichiometric NiTi alloy (Funakubo 1987). The underlying mechanism behind the SME in SMAs is a reversible diffusionless solid-solid phase transformation between austenite (high temperature phase) and martensite (low temperature phase) through a fully reversible atomic shear-lattice distortion process.

Today a wide range of SMAs have been developed in forms of solid, film and even foam. Among them, three alloy systems, namely, NiTi-based alloys, Cu-based alloys, Fe-based alloys, are presently more of commercial interest (Otsuka and Ren 1999; Sutou *et al.* 1999; Xie *et al.* 1996; Xu *et al.* 2003). NiTi-based alloys should be the first choice due to their excellent SME, high reliability, high mechanical performance and good biocompatibility (Lagoudas 2008; Otsuka and Ren 1999; Zhou *et al.* 2009). All these SMAs are thermo-responsive, i.e., the required stimulus for the SME is heat (including joule heating and inductive heating etc) (Miyazaki *et al.* 2009). Recently, some ferromagnetic/magneto-responsive SMAs have been developed, in which the additional stimulus is magnetic field (Dong *et al.* 2004; Feuchtwanger *et al.* 2009).

If heat shrinkable polymers are taken into account, the history of shape memory polymers (SMPs) can be traced back to as early as 1906 (Gunes and Jana 2008), even earlier than SMAs. However, technically speaking, we often regard that SMP was firstly introduced in 1984 in Japan (Liang *et al.* 1997), which is a polynorbornene-based SMP invented by Nippon Zeon Co.. Since then significant efforts have been devoted into SMPs due to their various advantages over other SMMs, such as high degree of recoverable strain (up to 800%) (Liu *et al.* 2007), light weight, low cost, low density, tunable mechanical property, easy processing, tailored application temperature, potential biodegradability and biocompatibility, etc (Sun *et al.* 2012).

The underlying mechanism behind the SME in SMPs is different from that of SMAs. A dual-segment/domain system, in which one is always elastic within the working regime of our interest, and the other is able to soften/harden upon presentence/removal of the right stimulus, is one basic mechanism, while reversible dual-phase system (e.g., between glassy state and rubbery state in elastomers) is the other.

Till today, a variety of SMPs have been reported and well documented in the literature, while new ones keep on emerging every week, if not every day (Mather *et al.* 2009; Rousseau 2008). Among them, a polyurethane SMP originally invented by Dr. S. Hayashi at Nagoya R&D Center of Mitsubishi Heavy Industry (Japan), and a polystyrene based SMP from Cornerstone Research Group (USA) have been widely applied and successfully marketed at present (Dietsch and Tong 2007)

Polymeric gel has an elastic crossed-lined network which has fluid filling interstitial spaces and is thus ready to change its size (up to three orders of magnitude) according to environmental conditions, such as temperature, light, pH, solvent, and electric field, etc (Li *et al.* 1997; Osada and Matsuda 1995; Wei *et al.* 1998a). However, gels are normally considered as a SCM. On the other hand, some gels do exhibit the SME due to, for example, a reversible order-disorder transition (Gong 2010; Mitsumata *et al.* 2001). Gels can servers as a system of converting chemical energy into mechanical energy, but their mechanical stability and performance as an actuation material are rather poor (Lendlein and Kelch 2002; Osada *et al.* 1992).

Shape memory ceramic (SMC) may have a multi-phase system in which the elastic phase drives the viscous phase for shape recovery, or have the reversible martensitic transformation just like that in SMAs, or have a ferroelectric/ferromagnetic transition which is accompanied by recoverable strain change (Schurch and Ashbee 1977; Swain 1986; Wei *et al.* 1998a). Although the recoverable strain in SMCs is normally small, their response speed can be very high. In addition, due to their ceramic nature, they are more suitable for high temperature applications.

The recently emerging type of SMM is shape memory hybrid (SMH), which consists of two or more components but without any SME as an individual within the working environment of our concern. Although relatively much newer, SMH is essentially more attractive since it is easily accessible to ordinary people (instead of professionals only) to design his/her own SMMs even without much background knowledge of materials and materials processing. SMHs share largely the similar working principle as that of SMPs. However, naturally SMHs can be easily designed to have a much wider range of tailored functions and features to meet the requirements in engineering applications (Fan *et al.* 2011; Huang *et al.* 2010a; Sun *et al.* 2012). To explore and demonstrate the mechanisms and advantages of SMHs are the focuses of this current study.

It should be pointed out that the concept of SMH is different from shape memory composite (SMc) as SMc has at least one SMM (most likely, SMA and/or SMP) as its component (Ratna and Karger-Kocsis 2008; Tobushi *et al.* 2009; Wei *et al.* 1998b). Consequently, as revealed in Fig. 1.1, SMc is not an independent subgroup of SMM.

1.2 Typical innovative applications of SMMs

The SME in SMMs has attracted not only great attention within a few scientific research communities, but also engineers and even medical doctors towards many real applications, which range from industry (for instances, aerospace engineering and robots) to our daily life (for instances, medical devices and smart textile) (Kudva *et al.* 2001; Lagoudas 2008; Thompson 2000; Wache *et al.* 2003). Many applications, which are difficult to be handled by traditional materials/mechanisms, can now be achieved comfortably by utilizing the SME in SMMs. Some typical and novel applications of SMMs, in particular SMAs and SMPs, are briefly presented here.

- **SMAs**

SMAs have many specific advantages, such as high recovery stress (as high as 500 MPa), superelasticity, good corrosion resistance, stiff at high temperatures while soft at low temperatures, and good biocompatibility (for NiTi SMAs) etc. Consequently, a number of SMA based devices have been successfully commercialized.

One of the most well-known examples is the hydraulic tube coupling which is made of SMAs and used in F-14 aircraft (Otsuka and Ren 1999). The tube coupling is compliant in martensite at a low enough temperature and thus can be easily extended in diameter to assemble two detached tubes together. Upon heating to high temperatures, which is high enough to trigger the phase transformation from martensite to austenite, the coupling shrinks back to its original small size, and thus tightly embraces two tubes together. As compared with conventional ones, lower in weight and higher in reliability are the major benefits of SMA coupling.

The dream of “The material is the machine”, i.e., to integrate the sensing and reaction (in terms of actuation) functions together within a piece of material, has been achieved, at least partially, in SMAs. SMA components (serving as both sensor and actuator) have been applied in variable geometry chevrons in a Boeing 777-300ER with GE-115B engines (Mabe *et al.* 2006). Utilizing the advantages of SMAs, such as, compact design (due to the integration of both sensing and actuation functions), light weight and robust in performance, simple in working mechanism, variable geometry chevrons can greatly reduce jet noise during takeoff, landing and cruise.

- **SMPs**

SMPs have been utilized in a wide variety of applications in various fields, such as, heat-shrinkable tube, active disassembly, engine valves, breathable temperature-dependent moisture-permeable fabrics, rewritable digital storage media, doll hair, temperature actuators/sensor etc (Chiodo *et al.* 1999; Liu *et al.* 2007; Ota 1981; Ratna and Karger-Kocsis 2008).

Biomedical applications of SMPs have emerged as a very hot topic recently, in particular for minimally invasive surgery, due to their excellent biocompatibility and some unique properties, such as tunable mechanical properties and transition temperatures, large recoverable strain, etc (Lendlein *et al.* 2010; Maitland *et al.* 2009; Small *et al.* 2010; Xue *et al.* 2010).

As a typical example, the suture made of a biodegradable SMP developed by (Lendlein and Langer 2002) perfectly illustrates the great potential of SMPs in biomedical applications. Sutures for wound closure should be properly designed, especially for the recoverable force, neither too weak to cause a scar tissue, nor too strong to result in necrosis. High recoverable strain and compatible recovery stress in SMPs provide the just right solution. A piece of 200% pre-stretched SMP wire loosely sutures belly tissue and abdominal muscle together. After heating, SMP wire shrinks and tightens with a force of 0.1 N. Since the SMP is biodegradable, it is unnecessary to have another operation for removal.

Conventional aircrafts have only one profile during takeoff/landing and cruise, although drag in different flight stages is remarkably different. As such, different flight profiles, e.g., one for long range cruise and the other for maneuverable fighting, are ideal. Consequently, the wings of an aircraft need to have the ability to change the shape accordingly to maximize performance. Researchers at Cornerstone Research Group, Inc., USA have demonstrated such morphing wings by using a light-activated SMP. Using light instead of heat for actuation essentially gets rid of the additional weight for thermal heating and increases the responsive frequency (Havens *et al.* 2005).

1.3 Objectives of this study

Own to their metal nature, SMAs are able to provide a high actuation stress (up to 500 MPa), but limited recoverable strain (less than 8%) (Sun *et al.* 2012). In addition, the material cost and processing cost of SMAs is high. On the other hand, SMPs are much cheaper than SMAs in terms of both materials cost and processing cost. However, the relatively lower recovery stress in SMPs (*normally only* a couple of MPa at the most) greatly limits the range of possible applications. Table 1.1 compares the major advantages and disadvantages of SMAs and SMPs.

Table 1.1 Comparison of major advantages/disadvantages of SMAs and SMPs.

	SMAs	SMPs
Advantages	▪ High recovery stress ▪ High strength ▪ High recovery speed ▪ Easy to achieve reversible actuation	▪ High recoverable strain ▪ Low density ▪ Low cost ▪ Easy to achieve multiple-SME ▪ Multiple-stimuli (heat, chemicals, and light etc.)
Disadvantages	▪ Low recoverable strain ▪ High cost ▪ Difficult to achieve multiple-SME ▪ Limited type of stimulus (heat and magnetic field only)	▪ Low recovery stress ▪ Low strength ▪ Low recovery speed ▪ Difficult to achieve reversible actuation

From application point of view, the existing SMMs, mainly SMAs, SMPs and other traditional ones, cannot easily meet all engineering requirements in many occasions. On the other hand, although SMPs are more versatile, even for a professional material/polymer researcher, a long journey of trial and error is normally required in order to tailor their properties. As for new features/functions, the effort may not always be rewarded in the end. Of course, it is easy to conclude that this kind of development work is not easily accessible to other professionals without necessary knowledge and experience on polymers. Apparently, it will greatly widen the application field of SMMs if there is a systematic approach, which is easily accessible to ordinary people (in particular, other professionals, who know exactly what they need in their applications), to design and fabricate his/her own SMM to precisely meet the exact requirements, not only mechanical requirement but also function requirement, etc. The concept of SMH appears to be the right approach for this purpose.

The objectives of this study are

- To systematically investigate the underlying mechanism of SMH.
- To demonstrate the full capability of SMH, not only to reproduce all types of shape memory phenomena, but also to realize some features/functions which are not possible in other types of SMMs.
- To develop a series of silicone-based SMHs to verify the design concept of SMHs with tailored function(s) and properties.

1.4 Outline of the dissertation

Chapter 1 briefly introduces the backgrounds and applications of SMMs, and presents the objectives of this study and outline of this dissertation.

Chapter 2 is a concise while comprehensive review about SMAs and SMPs, which includes all types of shape memory phenomena, various actuation techniques and characterization technologies, and research directions for further development.

Chapter 3 systematically investigates the underlying mechanism of SMHs. Finite element analysis is also carried out for verification.

Chapter 4 demonstrates that all types of shape memory phenomena can be realized in a silicone-wax hybrid system.

Chapter 5 presents all features of a multiple-stimuli-responsive silicone-sodium acetate trihydrate SMH.

Chapter 6 discusses silicone-melting glue SMH which is not only rubber-like at both high and low temperatures, but also has repeated and instant self-healing function.

Chapter 7 shows more novel SMHs which have tailored features that are difficult to be realized in other SMMs.

Conclusions and future works are presented in Chapter 8.

Chapter 2 Literature Review

In this chapter, a concise while comprehensive literature review is presented to provide the background knowledge of SMMs, which covers both actuation and characterization techniques, and all shape memory phenomena and their underlying mechanisms. While shape memory alloys (SMAs) are mentioned rather briefly, the emphasis is more focused on shape memory polymers (SMPs), since they are more relevant to the current study.

2.1 Shape memory effect in shape memory alloys

The underlying mechanism behind the shape memory effect (SME) in SMAs is the reversible martensitic transformation between the high temperature austenite and the low temperature martensite (Lagoudas 2008; Lin and Wu 1992; Otsuka and Ren 1999). It can be better understood by following the thermomechanical process revealed in Fig. 2.1, which is in a stress-strain-temperature space, together with the corresponding microstructures.

Let us start from point 1 which is at high temperatures and the sample is stress-free. Upon cooling the martensitic transformation starts at the martensite start temperature (M_s), and completes at the martensite finish temperature (M_f). The resultant martensite is thermally induced and twinned. Apart from surface relief (and thermal contraction), there is not any macroscopic shape change at all. Upon loading (e.g., stretching) at point 2, twinned martensite elastically deforms slightly followed by detwinning which is accompanied by significant quasi-plastic deformation. As such, after unloading from point 3, a large residual strain is observed at point 4. Different from conventional materials, the residual strain is recoverable upon heating, which starts at the austenite start temperature (A_s) and finishes at the austenite finish temperature (A_f).

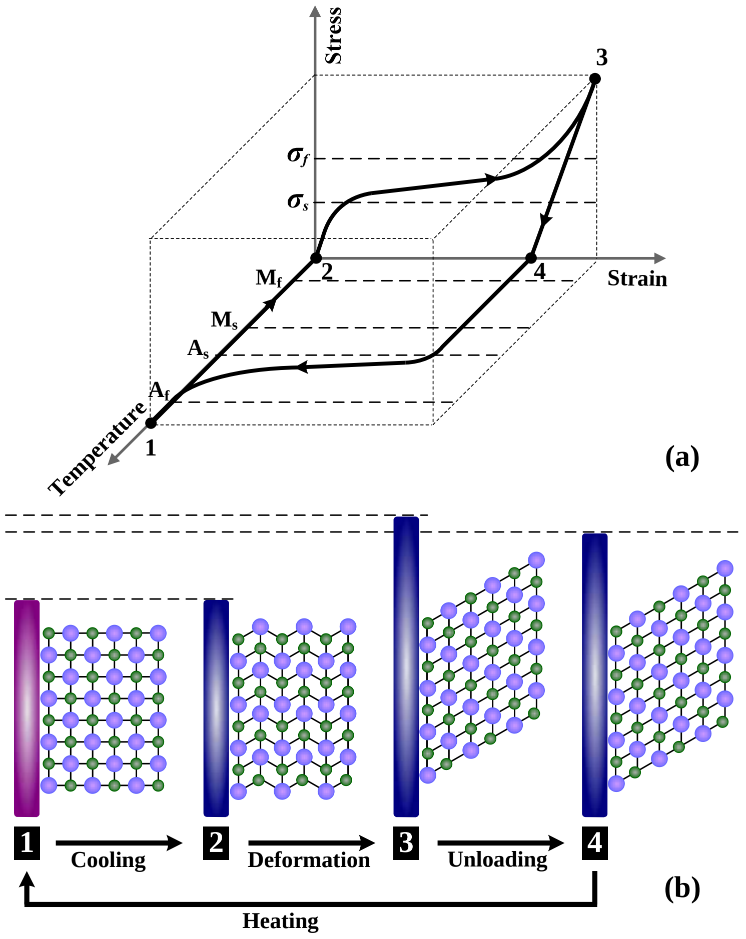

Figure 2.1 The SME in SMA (a) and corresponding change in phase/length (b).

If distortion is conducted at high temperatures, which requires a much higher stress since austenite SMA is much harder than martensite SMA, SMA is able to instantly return the original shape. This is known as superelasticity, which is a phenomenon belonging to shape change materials (SCM).

The ability to remember the original austenite shape is an intrinsic feature of SMAs, so called one-way SME. However, after certain training, which is a process to introduce an internal stress field into a piece of SMA with the one-way SME, the SMA is able to switch between the high temperature shape and low temperature shape upon thermal cycling. This feature is known as the material two-way SME (Huang 1999; Huang and Toh 2000), which is different from the mechanical two-way SME, in which a SMA (only with one-way SME) biases against an elastic spring or another piece of SMA (Huang 2002). Strictly speaking, with the material two-way SME, a SMA should fall into the category of SCMs. However, we still follow the traditional definition in the course of this work.

On the other hand, shape recovery in SMAs is normally from the distorted shape (or temporary shape) to the original shape. As there are only two shapes involved, one may call such SME as dual-SME. Since we can introduce a gradient shape recovery temperature field (either permanent or temporary) into a SMA (Huang *et al.* 2004; Liu and Tan 2000; Mahmud *et al.* 2008) or utilize some special mechanisms (Huang *et al.* 2004), it is possible to have one or more intermediate positions/shapes between the temporary shape and original shape during shape recovery. This is defined as the triple-SME (if only one intermediate shape) or multiple-SME (if the intermediate shapes are multiple).

In the above discussion, the stimulus to trigger the SME is heat, i.e., thermo-responsive. In some other SMAs, a magnetic field can be used as the stimulus without heating involved. This type of SMAs is knows as magnetic SMA (Dong *et al.* 2004; Feuchtwanger *et al.* 2009; Miyazaki *et al.* 2009). So far, all current magnetic SMAs are too brittle and cannot be used for actuation in engineering applications as thermo-responsive SMAs.

Despite some merits, such as high recovery stress, high strength, high recovery speed, high transition temperature, and easily realized two-way (material or mechanical) SME, some intrinsic drawbacks of SMAs limit their application. For examples, the recoverable strain in dual-SME (or in mechanical two-way SME) is less than 8%, while in material two-way SME, the recoverable strain is much smaller (Sun et al. 2012). Currently, the stimuli to initiate shape recovery of SMAs are only limited to heat and magnetic field. Both the fabrication and procession cost of SMAs is very high. The high density of SMAs is a serious deficiency when light weight is required. In addition, SMAs are not biodegradable.

2.2 Shape memory effect in shape memory polymers

Most of the common terminologies used in the field of SMMs have been introduced in Section 2.1, when SMAs are briefly introduced. In this section, we will focus on the details of SMPs since from the mechanism point of view, shape memory hybrids (SMHs) share many similarities with SMPs.

2.2.1 Elastomer and SMP

Even now within the community of SMMs, many people are still confused by the difference between elastomers and SMPs, since they all seemingly have the SME, at least at certain level. In the literature, most researchers claimed that all SMPs are closely analogous elastomer (Gunes and Jana 2008; Leng and Du 2010).

In fact, there are two basic mechanisms for the SME in polymeric materials, namely dual-phase and dual-component (either segment or domain). While reversible glass transition (thus, dual-phase) can be applied as the mechanism for the SME in elastomers, dual-segment system is behind the SME in polyurethanes.

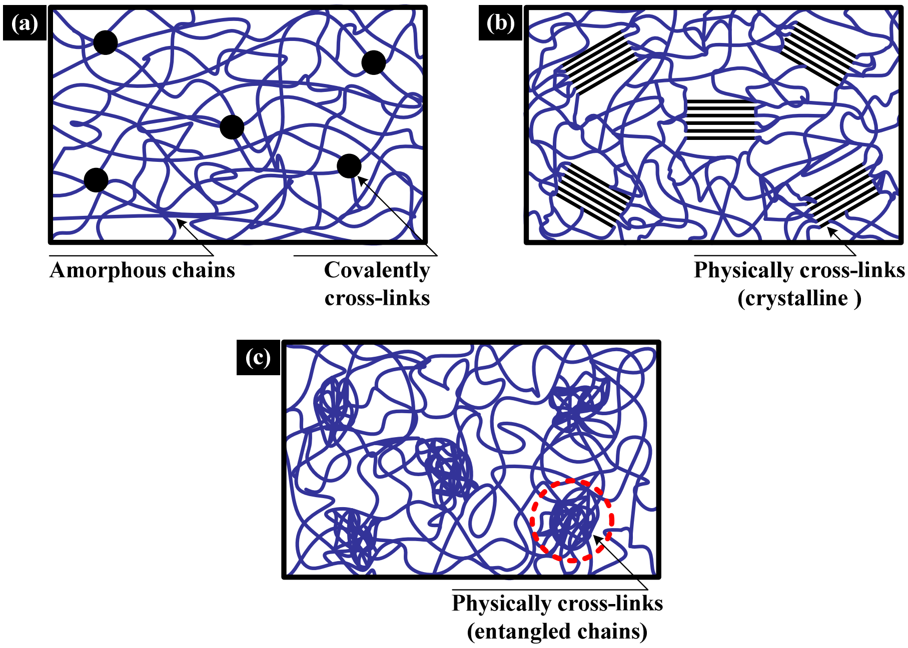

Figure 2.2 Typical types of cross-links in elastomers. (a) covalent; (b) crystalline domain; and (c) entangled chain.

In an elastomer with good cross-links (either chemically or physically. Refer to Fig. 2.2 for three typical scenarios of cross-links), at above the glass transition temperature (T_g), the polymer is in the rubbery state and can be easily and elastically deformed. Upon cooling to below T_g, the deformed shape can be maintained due to the mobility of molecular chains is frozen. Upon heating to above the T_g, micro Brownian motion takes action again, so that the elastomer is able to recover toward its original shape. However, the exact recovery ratio is highly dependent on the type/level of cross-link and the amount/type of pre-deformation. Silicone (Fig. 2.2a) is a typical example.

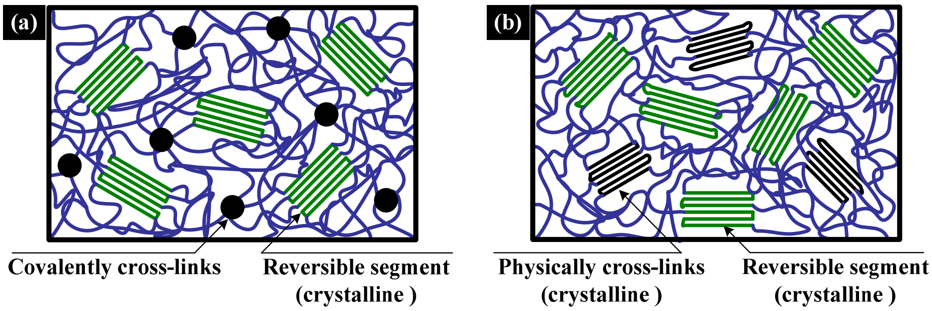

Figure 2.3 Typical illustrations of elastic component and transition component in SMPs. (a) covalently cross-linked elastic component, and (b) physically cross-linked component.

On the other hand, in dual-component SMPs, there is a transition component (which might be segment or domain. Refer to Fig. 2.3 for typical morphologies), so that at the presence of the right stimulus, the transition component is significantly softened (by means of glass transition or melting in thermo-responsive SMPs) and the elastic component (which might be segment or domain) can be easily deformed. After removal of the stimulus and the constraint, the recovery of the elastic component is prevented by the re-hardened transition component. Only by means of reapplying the right stimulus, which softens the transition component again, is able to release the elastic energy in the distorted elastic component, and thus induces the shape recovery. The exact shape recovery ratio is dependent on the elasticity of elastic component..

On the other hand, practically, we can apply the dual-component concept to an elastomer (which is naturally dual-phase as discussed above) by means of deforming at a middle point within the glass transition range, so that the glassy part serves as the transition component, while the rubbery part functions as the elastic component. This is another approach to achieve the SME, which is seemingly more relevant to the dual-component mechanism rather than the dual-phase mechanism.

It should be pointed out that while we discuss the SME in elastomers, we actually focus on the glass transition for shape fixing and shape recovery (thermo-responsive SME) or shape fixing only (e.g., chemo-responsive SME). However, in a dual-component polymer, we have at least melting of the transition component as an additional option. Since the conventional definition of SMP covers any polymeric material with the SME based on either dual-phase mechanism or dual-component mechanism, it is apparent that in terms of the SME, different from those claimed in the literature (Lendlein and Kelch 2002; Leng and Du 2010), all elastomers, whatever thermo-plastic or thermo-set, should be a subset of polymeric material under SMP.

It should be pointed out that the exact performance in terms of the SME in a SMP depends on not only the material itself, but also the applied stimulus and distortion. Since the current project is actually based on the concept of dual-component system, hereinafter, our discussion will be focused on dual-component mechanism.

According to Liang et al (Liang *et al.* 1997), the polynorbornene-based SMP invented in 1984 by Nippon Zeon Co. in Japan is considered as the first generation of SMP. This SMP and the other two invented subsequently (namely a trans-isopolyprene-based developed by Kuraray Company, Japan and a styrene-butadiene-based developed by Asahi Company, Japan) all have the problem of limited processability. The thermoplastic polyurethane SMP invented by Dr S Hayashi does not have such problem at all (Hayashi 1990) and has been very well commercialized right now. Another relatively new but also successfully marketed SMP is a thermo-set polystyrene from Cornerstone Research Group, USA (Dietsch and Tong 2007).

2.2.2 Types of SME in SMPs

Different from SMAs, while all current SMPs and their composites have the one-way SME, only a couple of them have the mechanical two-way SME. This is due to that normally a polymer is softer upon heating, which is opposite to that in SMAs. In addition to dual-SME, triple-SME and multiple-SME can be easily achieved in SMPs with/without introducing a gradient transition temperature field (Bellin *et al.* 2006; Sun and Huang 2010; Xie 2010). All these SME phenomena in thermo-responsive SMPs are schematically illustrated in Fig. 2.4.

In comparison with the conventional dual-SME, multiple-SME is more attractive, which significantly enhances the technical potential of SMPs for a wider range of applications.

Instead of introducing a gradient transition temperature field (Huang *et al.* 2005) which may have some difficulties to achieve in many engineering applications, thermally induced triple(and multiple)-SME can be more conveniently achieved by means of incorporation of additional component(s) (either segment or domain or both of them) with different transition (glass transition or melting) temperature(s) (Behl *et al.* 2009; Bellin *et al.* 2006; Luo and Mather 2010; Pretsch 2010), or by utilizing one transition which has a relatively wide temperature range (Xie 2010). Recently, multiple-SME activated by applying different radio-frequencies for heating different components has been demonstrated (He *et al.* 2011).

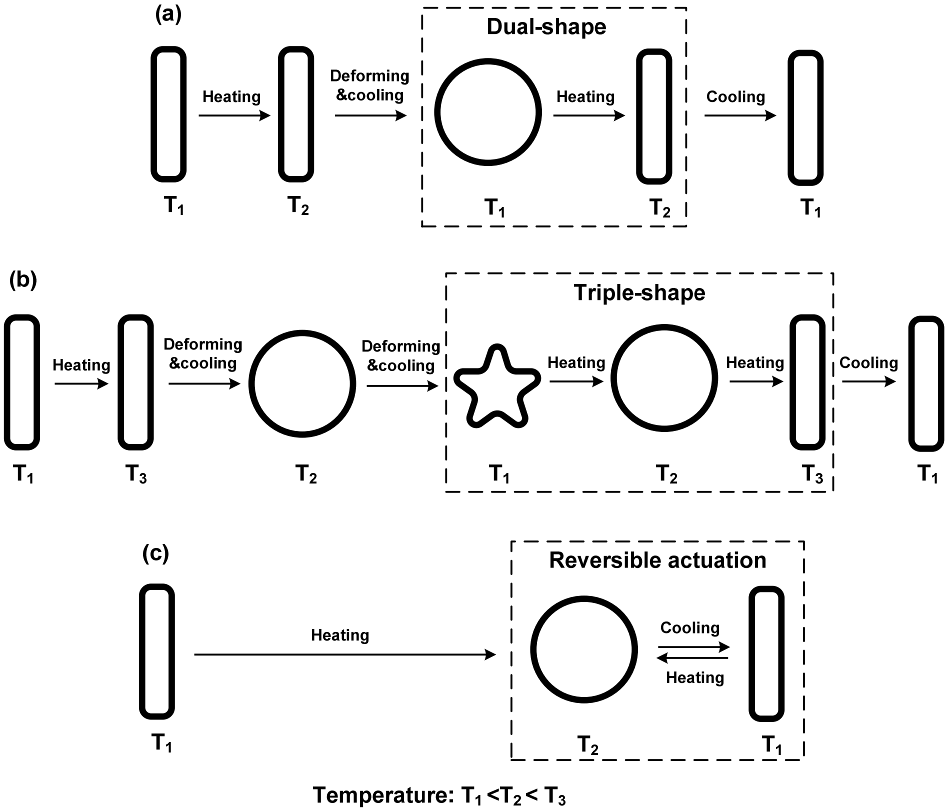

Figure 2.4 Schematic illustration of different SME phenomena in thermo-responsive SMPs. (a) one-way dual-SME; (b) one-way triple-SME; (c) mechanical two-way SME.

Although (Behl *et al.* 2009) claims that the triple-SME can be programmed in one-step, traditional programming procedure for the triple-SME involves two steps as illustrated in Figure 2.4(b).

On the other hand, bi-layer polymer composites consisting of two different polymers can be designed to have the triple-SME with tailored shape fixity (Xie *et al.* 2009). However, such materials should be under the category of shape memory composite (SMc), which is beyond the scope of current study.

Unlike that in SMAs, which is hard at high temperature austenite phase and soft at low temperature phase, so that they are just the right material for mechanical two-way SME upon thermal cycling, thermo-responsive SMPs are normally soft at high temperatures and hard at low temperatures, unless in some special polymeric materials, such as liquid crystalline elastomer (Rousseau and Mather 2003), which become stiffer when heated due to alignment of crystals/molecular chains. In addition, a special semicrystalline network with crystallization-induced elongation upon cooling and melting-induced shrinkage upon heating has been used to fabricate mechanical two-way SMPs (Chung *et al.* 2008; Lee *et al.* 2008). All above mentioned mechanical two-way SME is between two shapes, i.e., mechanical two-way dual-SME. Recently, a SMP with reversible triple-SME under a constant load upon thermal cycling has been developed (Zotzmann *et al.* 2010). This SMP has the same underlying mechanism as the semicrystalline network reported in (Chung *et al.* 2008; Lee *et al.* 2008), which have the mechanical two-way dual-SME.

Polymeric laminated composites made of an one-way SMP layer atop an elastic substrate was reported to seemingly have the material two-way SME (Chen *et al.* 2008). However, it is actually activated by the difference in thermal expansion coefficient between the SMP and substrate, a well-known phenomenon in bi-layered structures.

2.2.3 Actuation mechanisms and methods for SME

Typical stimuli for activating SMPs including heat (thermo-responsive), electrical current (electro-responsive), magnetic field (magneto-responsive), chemicals (chemo-responsive), and light (photo-responsive) etc. (Cho *et al.* 2005; Huang *et al.* 2005; Jiang *et al.* 2006; Mohr *et al.* 2006). However, based on the exact mechanism, they are all under the following three categories.

- Thermally induced SME

At present, thermally induced SME in SMPs refers to heating for actuation, either by means of direct heating or indirect heating. After blending with conductive fillers, the electrical conductivity of polymers can be enhanced and thus be suitable for joule heating (Cho *et al.* 2005; Leng *et al.* 2008a). Induction heating by means of applying an alternating magnetic field in a polymer embedded with magnetic fillers has been proposed for remote wireless activating SMPs (Mohr *et al.* 2006). Buckley *et al.* (2006) have demonstrated that with 10% volume fraction of nickel zinc ferrite ferromagnetic particles, SMPs can be heated for shape recovery. In addition, the feature of self-thermoregulation in them prevents overheating, which is very important in medical applications. In most of the reported works, very high frequency is required, but Zheng *et* *al.* (2009) showed that 20 kHz is enough for poly(D,L-lactide)/Fe_3O_4 nanocomposites**.** Light illumination is an alternative, which can be applied in either contact mode (Maitland *et al.* 2002; Small Iv *et al.* 2005) or contactless mode (Koerner *et al.* 2004) for heating.

-Chemically induced SME

Instead of heating for softening the transition component of a SMP or for the glass transition in an elastomer, we can always find some right chemicals to soften the polymer by means of, for instance, plasticizing, such as in a water/moisture-responsive polyurethane (Huang *et al.* 2005; Yang *et al.* 2005; Yang *et al.* 2004; Yang *et al.* 2006) and ethanol-responsive poly(methyl methacrylate) (Zhao *et al.* 2011).

-Light directly induced SME

Instead of light induced heating for thermally induced SME, light directly induced SME has been realized in a few polymeric systems (Jiang *et al.* 2006; Lendlein *et al.* 2005). Upon exposing to ultraviolet light with a wavelength λ>260 nm, the photo-responsive components in these polymeric systems are cross-linked (filled diamonds), which results in a temporary shape. These newly formed photo-responsive cross-links are reversibly cleaved upon irradiation by ultraviolet light with a wavelength λ<260, which results in the shape recovery.

2.2.4 Characterization of thermo-mechanical response

We take thermo-responsive dual-component SMPs as an example. Apart from conventional differential scanning calorimeter (DSC), thermogravimetric analysis (TGA) and dynamic mechanical analysis (DMA), some standard approaches and techniques have been applied for the characterization of the thermo-mechanical response of SMPs, including the SME.

-Thermo-mechanical cycling

A typical thermo-mechanical procedure to characterize the SME in SMPs is illustrated in Fig. 2.5, in which there are four major steps as following.

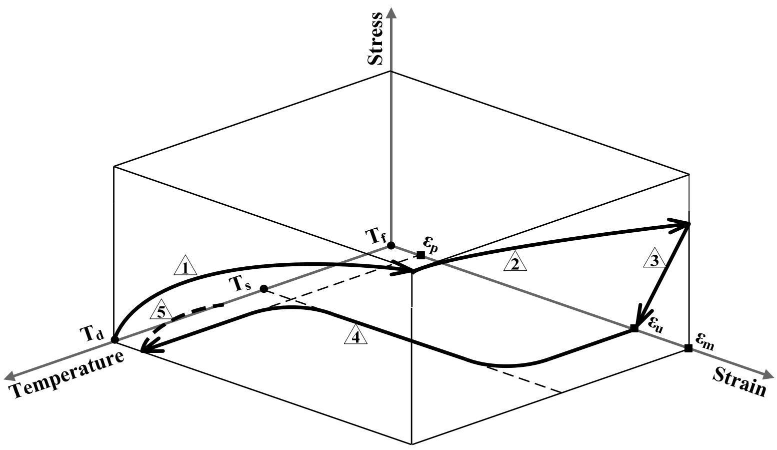

Figure 2.5 Schematic representation of stress-strain-temperature diagram of a thermo-responsive SMP in a thermo-mechanical cycle.

Step 1) Mechanical loading at high temperatures

After pre-heating a piece of freestanding SMP to $T_d (= T_s + \Delta T)$, where T_s is the middle point of a phase transition which might be the glass transition (T_g) or melting (T_m) of the transition component. Typically, ΔT is 10~20^{o}C to ensure T_d is above the transition finish temperature. At T_d, deform the SMP to a prescribed maximum strain of ε_m at a constant strain rate.

Step 2) Cooling with constraint applied

This is a step to freeze the transition component. Cooling is conducted with ε_m maintained to a specified low temperature (T_f), which is normally the room temperature or at least below the transition start temperature.

Step 3) Removal of constraint

After removal of the constraint, some instant elastic recovery occurs. The residual strain is defined as ε_u. Technically, this shape is called the temporary shape, and Steps 1-3 are known as the programming process (or programming for short).

Step 4) Heating for the SME

After heating for thermally induced SME, the remaining strain, if any, is defined as ε_p. This step is technically called the shape recovery process.

These four steps may be repeated many times.

Depending on the exact polymer, there are many versions which can be derived from the above standard cycle. For instance, some SMPs can be programmed in the glassy state at low temperatures (Abrahamson *et al.* 2003; Koerner *et al.* 2004; Rodriguez *et al.* 2011; Yang 2007). Very recently, Sun *et al.* (2011) pointed out that the performance of SMPs can be optimized by means of programming at a selected temperature, which is within the transition temperature range.

-Characterization of the SME

Refer to Fig. 2.5. There are three important parameters in characterizing the SME in a SMP, namely the strain recovery ratio (R_r), total strain recovery ratio ($R_{r\text{-}total}$) and strain fixity ratio (R_f). In the case of multiple cycling, they are defined as following,

$$R_r(N) = \frac{\varepsilon_m - \varepsilon_p(N)}{\varepsilon_m - \varepsilon_p(N-1)} \times 100\% \tag{2.1}$$

$$R_{r-total}(N) = \frac{\varepsilon_m - \varepsilon_p(N)}{\varepsilon_m} \times 100\% \tag{2.2}$$

$$R_f(N) = \frac{\varepsilon_u(N)}{\varepsilon_m} \times 100\% \tag{2.3}$$

Here, N is the cycle number, $R_r(N)$ measures the shape recovery ability in the N^{th} cycle, while $R_{r\text{-}total}(N)$ measures the shape recovery against the original shape. R_f indicates the ability to fix the temporary shape. As revealed in (Sun *et al.* 2011), in order to achieve higher R_f, a higher T_d should be applied.

-Programming mode in characterization of the SME

Although the exact programming mode is determined by the actual application, some standard programming modes have been applied to characterize the SME in SMPs.

While uniaxial tension and uniaxial compression are commonly used programming modes (Huang *et al.* 2006; Li *et al.* 1999; Tobushi *et al.* 2004; Tobushi *et al.* 2001), which can determine a range of short/long term properties even by means of DMA test, bending test (as illustrated in Fig. 2.6) is also popular in many engineering practice (Zhang and Ni 2007).

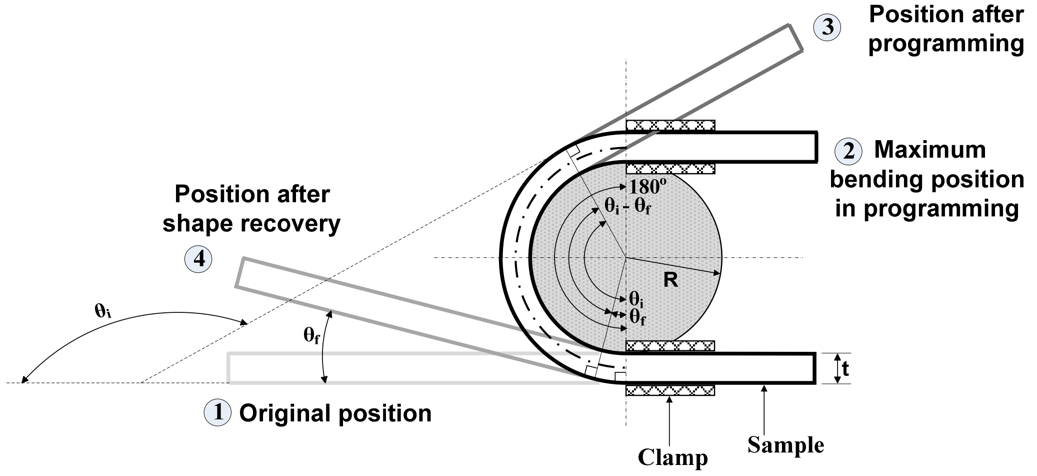

Figure 2.6 Schematic illustration of characterization in bending mode.

As revealed in Fig. 2.6, at T_d, one end of a SMP strip (with a thickness of *t*) is fixed to a shaft (with a radius of R) by a clamp, and the other end is bent by 180^{o} and fixed by the other clamp. Here180^{o} is the maximum bending angle between two ends of the SMP strip at a specific (high) temperature in programming. The surface strain ε_s, which is in tension or in compression, can be estimated by

$$\varepsilon_s = \frac{t}{2R+t} \tag{2.4}$$

After being cooled to T_f, the top clamp is removed. The residual angle between two ends of the SMP strip after programming, θ_i, is measured. After heating for shape recovery, the remaining angle between two ends of the SMP strip, θ_f, is recorded. Subsequently, the shape fixity ratio R_f and shape recovery ratio R_r can be determined by,

$$R_f = \frac{\theta_i}{180^o} \tag{2.5}$$

$$R_r = \frac{\theta_i - \theta_f}{\theta_i} \qquad (2.6)$$

2.3 Developments for new features and enhanced performance

The advantages of low cost, low density, versatility and flexibility to achieve tailored properties have prompted SMP to be a major player in the field of SMMs in recent years. Despite of a number of great achievements in the past years, we can see that it is highly in demand for further developments in SMMs to meet the needs from many engineering applications, which include new features (e.g., new types of stimulus and new functions) and enhanced performance (e.g., high reaction speed and actuation stress).

On the one hand, in 2008, Prof. B. K. Kim suggested a few new types of stimulus as a part of future developments (Kim 2008). Merely within three years, except pressure-responsive, all others have been realized. On the other hand, while by default, at present thermo-responsive is meant for heating for shape recovery, cooling for shape recovery can provide a useful alternative, which may add in a new dimension in applications of SMMs.

Multiple-stimuli-responsive feature is also desired in many applications to provide additional flexibility in applications. Among a couple of others, thermo/moisture-responsive polyurethane SMP is a typical example (Huang *et al.* 2010b; Yang 2007), which has been developed. A thermo-responsive SMM, which can be either heated or cooled for shape recovery, provides an option for engineers to select the most suitable means for actuation in a particular application.

SMMs with additional functions atop the SME are highly in demand in engineering practices. SMPs with color change feature upon heating for thermally induced SME have been developed (Kunzelman *et al.* 2008). Unlike traditional self-healing materials (Toohey *et al.* 2007; Wool 2008; Yuan *et al.* 2008), integrated with self-healing function, a SMM is able to achieve both shape recovery and strength recovery. Preliminary investigation has been carried out with limited success in terms of strength recovery ratio (Rodriguez *et al.* 2011).

As reported by Lagoudas (2008), both shape recovery stress (actuation stress) and shape recovery speed (actuation frequency) of SMPs are all on the low range end among all active materials. While reinforcing polymers with conventional fillers is an effective approach to increase the stiffness and actuation stress of SMPs (Rousseau 2008), shape fixity ratio, processability and shape recovery ratio are usually more or less sacrificed. With a low content of carbon nanotube (CNT), one may achieve a significant improvement in stiffness and actuation stress without much deterioration in the SME (Koerner *et al.* 2004). Compared with conventional fillers, CNT has a high aspect ratio and is in nano-scale dimension, which enables for a relatively large number density within a unit volume of polymer even at a low content.

Effective approaches to increase the shape recovery speed of a thermo-responsive SMP include: 1) to reduce the heat capacity of polymer; 2) to increase the thermal conductivity of polymer; and 3) to narrow the transition temperature range etc. Instead of tailoring these properties by means of different receipts in chemical synthesis, blending with fillers can be a simple but very much effective approach for 1) and 2). Liu and Mather (2004) reported that recovery speed was increased significantly by embedding highly thermally conductive boron nitride fillers in a polycyclooctene based SMP. In terms of selection of fillers, beside the exact content, thermal conductivity, shape and size, aspect ratio, surface area, density, and interaction with polymer matrix (e.g., matching of surface tension) etc, are important issues to be considered. However, one should bear in mind that conventional fillers, such as carbon fiber and metal particle, are actually preferred to CNT for high speed purpose due to the compatibilization issue (Gojny *et al.* 2006; Rousseau 2008).

Chapter 3 Basic Concept and Mechanism

In this chapter, we discuss the basic concept of shape memory hybrid (SMH). The mechanism behind the shape memory effect (SME) in SMHs is investigated both schematically and analytically.

3.1 Basic concept of shape memory hybrid

Dual-domain/segment system (hereinafter, called dual-component system for simplicity), in which one is always elastic and the other is able to change its stiffness dramatically upon exposing to the right stimulus, is one of two mechanisms behind the shape memory phenomenon in shape memory polymers (SMPs). We have seen numerous SMPs developed by chemists and polymer scientists in the past years and new SMPs are invented every week, if not every day at this moment (Lendlein 2010; Liu *et al.* 2007; Sun *et al.* 2012). These SMPs, which are the results of hard work, are developed to meet the needs of different applications. A good understanding of the working mechanism and background knowledge is the pre-requirement for those experts, in addition to great efforts in trial and error, which is normally time consuming.

With the nature of the SME in SMPs in mind, we may extend the dual-component concept to achieve so called shape memory hybrid (SMH). In the literature, the term of shape memory composite (SMc) has been used for composites with at least one component, which has the SME, most likely a shape memory alloy (SMA) or SMP. However, for SMHs, as an individual, no component has the SME at all. This is the one key difference between SMH and SMc. Same as that in dual-component SMPs, a SMH has two basic components, one is elastic component (most likely as matrix) and the other is transition component (most likely as inclusions). Additional component(s) may be added in to modify the properties and/or enhance the performance of a SMH.

Ideally, the performance of the resultant SMH can be pretty well predicated based on the properties of the transition component and elastic component, even in the early design stage. Consequently, the time spending on trial and error in synthesis can be significantly shortened. To ensure this, we need to minimize, if not fully avoid, the interaction (mainly chemical) between the elastic component and transition component. Practically speaking, this can be achieved by carefully selecting a right combination of materials for the components and a proper processing procedure. This is the major difference between SMH and SMP.

While in many occasions, the interaction between the elastic component and transition component is an advantage in SMPs and has been utilized to tailor the properties, such as stiffness (e.g., the Young's modulus) and recovery temperature (Sun *et al.* 2011), in SMHs, we largely base on the selection of a right combination of materials for the elastic component and transition component to meet the particular needs of an application. We are able to do so in SMHs because the selection of materials for the components of a SMH is virtually without any limitation at all. Different from SMPs, in which their components are mainly selected from various types of polymers, any material (not only organics and inorganics, but also even metals) can be considered, either as the elastic component or as the transition component, for a SMH (refer to Fig. 3.1). This is an extremely important difference (as compared with that in SMPs), which provides great flexibility in design a SMH for tailored performance.

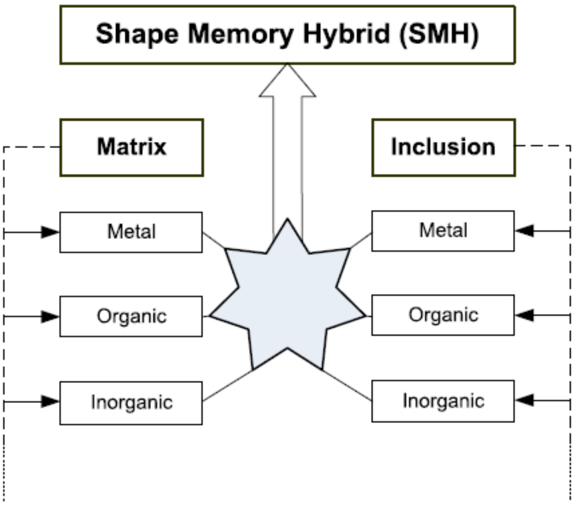

Figure 3.1 Possible components for SMHs (Sun *et al.* 2012).

As we can see, in comparison with that in SMPs, the design of SMHs requires not much chemistry and polymer background and is easily accessible to non-professionals and even medical doctors, who may have extremely limited knowledge on materials. Furthermore, with virtually no limitation in selection of components, we can design SMHs which are not possible if only within the regime of polymers. Of course, there are some principles to follow in design such SMHs and in selection of components for them.

3.2 Mechanism of the SME in SMHs

We take a silicone-wax hybrid (S-W) as an example (refer to Fig. 3.2). For simplicity, here silicone and wax are assumed to be in parallel in a small unit volume of this hybrid. Let us consider the thermo-mechanical behavior of this representative unit volume without considering thermal expansion in both silicone and wax.

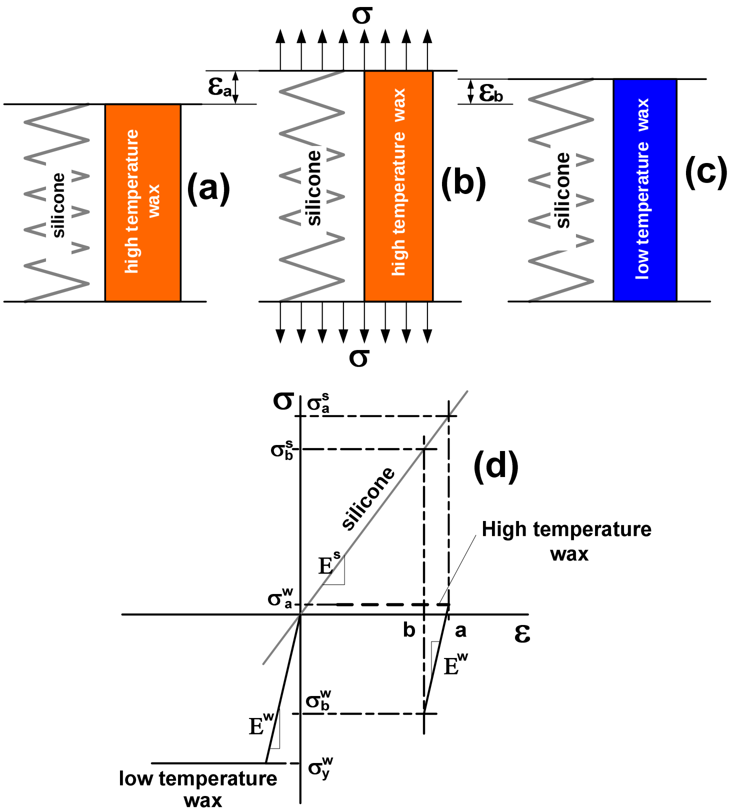

Figure 3.2 Illustration of the SME in S-W. (a) Free standing at high temperatures; (b) upon stretching at high temperatures; (c) after unloading at low temperatures; (d) stress vs. strain relationships.

We may assume silicone as an ideal perfect elastic material. On the other hand, wax is considered to be ideal elastic-plastic at low temperatures, while above its melting temperature, it is almost free to flow under a tiny force.

In terms of force equilibrium, one has,

$$\sigma = A^s\sigma^s + A^w\sigma^w \tag{3.1}$$

where σ is the stress applied on this unit volume of hybrid; σ^s is the stress on silicone; σ^w is the stress on wax; A^s is the cross-sectional area fraction of silicone; and A^w is the cross-sectional area fraction of wax.

Note that here our discussion is limited to small deformation, and engineering strain and engineering stress are applicable. Thus, it is apparent that $A^s + A^w = 1$. Hereinafter, superscripts *s* and *w* stand for silicone and wax, respectively.

Upon loading to a strain of ε_a at high temperatures, which is above the melting temperature of wax, the corresponding applied stress σ_a may be expressed as,

$$\sigma_a = A^s\sigma_a^s + A^w\sigma_a^w = A^sE^s\varepsilon_a + A^w\sigma_a^w \tag{3.2}$$

Here, E is the Young's modulus. As assumed, E^s is about a constant within the working temperature range. σ_a^w is the (tiny) stress required for wax to be free to flow at above its melting temperature.

Subsequently, the hybrid is cooled down and then the applied load is removed. Consequently, the residual strain is denoted as ε_b, the corresponding external stress $\sigma^b = 0$, and if $\sigma_b^w > \sigma_y^w$ (which is the yield stress of wax at low temperatures),

$$\sigma^b = A^s\sigma_b^s + A^w\sigma_b^w = A^sE^s\varepsilon_b + A^w\left[\sigma_a^w - E^w\left(\varepsilon_a - \varepsilon_b\right)\right] = 0 \tag{3.3}$$

Hence,

$$\varepsilon_b = \frac{A^w\left(E^w\varepsilon_a - \sigma_a^w\right)}{A^sE^s + A^wE^w} \tag{3.4}$$

To maximize ε_b in Eqn. (3.4) for better shape retaining means $\varepsilon_b \to \varepsilon_a$, which requires that,

- σ_a^w *is minimized and* $A^sE^s << A^wE^w$ **(Condition I)**

By ignoring the possible Bausinger effect when $-\sigma_y^w < \frac{A^s}{A^w}E^s\varepsilon_b$ as the stress state of wax is transferred from tension at high temperatures to compression at low temperatures, one has,

$$\sigma_y^w = \sigma_b^w = [\sigma_a^w - E^w(\varepsilon_a - \varepsilon_b)] \tag{3.5}$$

Eqns. (3.3) and (3.5) yield,

$$\sigma_y^w = -\frac{A^sE^s}{A^w}\varepsilon_b \tag{3.6}$$

From Eqns. (3.4) and (3.6), one can further deduce that,

$$\sigma_y^w = -\frac{(E^w\varepsilon_a - \sigma_a^w)}{1 + \frac{A^wE^w}{A^sE^s}} \tag{3.7}$$

To avoid further deformation from happening for good shape fixity requires that,

- $\sigma_y^w < -\frac{\left(E^w\varepsilon_a - \sigma_a^w\right)}{1 + \frac{A^wE^w}{A^sE^s}}$ **(Condition II)**

Upon heating $E^w \to 0$, $\sigma_y^w \to 0$, thus $\varepsilon_b \to 0$. Hence, shape recover occurs in the hybrid as illustrated in Fig. 3.2.

The basic mechanism behind the shape memory phenomenon and the requirements for good SME (Conditions I and II) are schematically discussed above based on the assumption that the elastic component is perfectly linear elastic. These principles can be further extended to other hybrid systems as well, and also largely applicable to other shape memory phenomena (such as, moisture-responsive, pressure-responsive, etc).

3.3 Numerical simulation

Above discussion in Section 3.2 provides us some basic understanding of SMHs. Simple numerical simulation (via finite element analysis) is further performed in this section to reveal more technical details of the SME in SMHs. Again, we take S-W as an example.

- *Model and constitutive law*

As discussed, silicone (elastic component) always is linear elastic within the whole process, while wax (transition component) actively plays its role to lock and unlock the stored elastic energy in silicone during programming and thermally induced shape recovery processes, respectively.

In order to catch the major features in a qualitative manner, let us consider an ideal case, in which all inclusions (wax) are in spherical shape and of the same size, and are distributed uniformly and periodically within the silicone matrix. Based on this conception, a representative 1/8 cell (assumed to be in a size of 1×1×1 mm^3) taken from a bulk sample can be used as a representative unit for simulation (Fig. 3.3). Again, thermal expansion is totally ignored in this simulation.

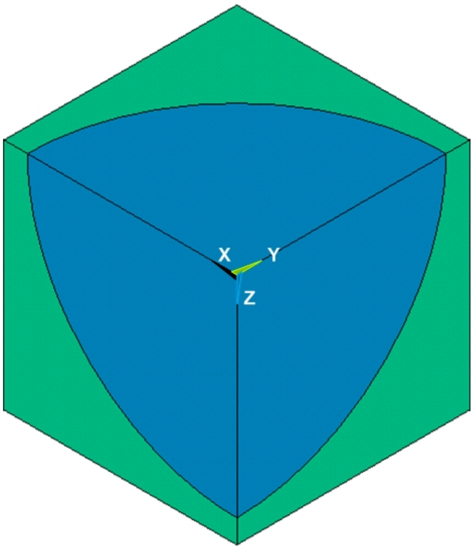

Figure 3.3 1/8 cell representative model for numerical simulation. Blue: transition inclusion; green: elastic matrix.

A simple isotropic linear elastic model is adopted for both matrix and inclusion. Large displacement induced geometrical nonlinearity, viscosity in polymers at high temperature, stress relaxation and creeping in polymers are ignored in current study. By extending the generalized Hooke's law for an isotropic material into three dimensions, its pseudo-vector-matrix form may be expressed as,

$$\begin{Bmatrix} \varepsilon_x \\ \varepsilon_y \\ \varepsilon_z \\ \gamma_{yz} \\ \gamma_{xz} \\ \gamma_{xy} \end{Bmatrix} = \begin{bmatrix} \frac{1}{E} & \frac{-\nu}{E} & \frac{-\nu}{E} & 0 & 0 & 0 \\ \frac{-\nu}{E} & \frac{1}{E} & \frac{-\nu}{E} & 0 & 0 & 0 \\ \frac{-\nu}{E} & \frac{-\nu}{E} & \frac{1}{E} & 0 & 0 & 0 \\ 0 & 0 & 0 & \frac{1}{G} & 0 & 0 \\ 0 & 0 & 0 & 0 & \frac{1}{G} & 0 \\ 0 & 0 & 0 & 0 & 0 & \frac{1}{G} \end{bmatrix} \begin{Bmatrix} \sigma_x \\ \sigma_y \\ \sigma_z \\ \tau_{yz} \\ \tau_{xz} \\ \tau_{xy} \end{Bmatrix} \tag{3.8}$$

where ε and γ are normal strain and shear strain, respectively; σ and τ are normal stress and shear stress, respectively; E and ν are the Young's modulus and Poisson's ratio, respectively; and $G = \frac{E}{2(1+\nu)}$ is shear modulus.

Refer to Fig. 3.3. E and v of elastic matrix (silicone) are assumed to be 2 MPa and 0.45, respectively. Both are more or less temperature independent at least within the temperature range of our interest (i.e., between 20°C and 100°C). On the other hand, E and v of transition inclusion (wax) should be highly temperature dependent. They are assumed to be 20 MPa and 0.3, respectively, at low temperatures (below the melting temperature of wax, T_m); and 0.2 MPa and 0.4, respectively, at high temperatures (above T_m).

- ***Boundary conditions and loads***

A commercial finite element software, namely *ANSYS*, is used in this simulation. Three-dimensional 10-node tetrahedral element is used. The total number of elements is around

50000, and total number of nodes is around 70000 in all cases reported here (refer to Fig. 3.4a). According to Fig. 3.3, symmetric displacement conditions are applied on three special surfaces (namely x=0, y=0, and z=0); and thus displacement coupling conditions are applied on nodes in three other surfaces (namely x=1, y=1, and z=1), as shown in Fig. 3.4(b).

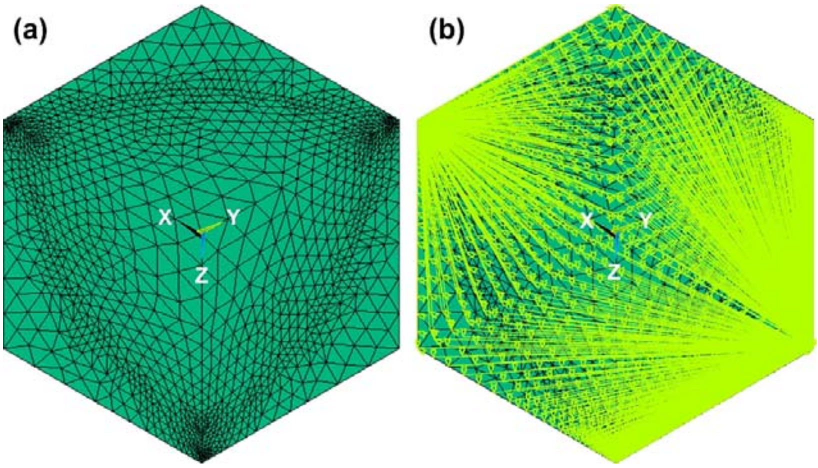

Figure 3.4 Mesh (a) and constraints (b).

Shape recovery after being programmed by means of uniaxial compression (along Z-axis) is simulated, i.e., a uniform compressive displacement is applied on the top surface (z=1). In all cases investigated here, the maximum applied compressive strain is 20%. Again, unless otherwise stated, the strain and stress reported here are engineering strain and engineering stress.

- ***Simulation procedure***

(1) Deformation at T_d

Since T_d is above the melting temperature of wax, the Young's modulus of the transition component is 0.2 MPa at T_d. After the surface of z=1 is compressed, we can obtain the resultant stress/strain field.

(2) Instant recovery after unloading at room temperature

Upon cooling to room temperature, the Young's modulus of wax is back to 20 MPa. After that, the applied constraint on z=1 surface is removed. Instant recovery, which is essentially elastic, occurs during unloading. Consequently, stress/strain distribution in both silicone and wax is altered.

(3) Shape recovery after heating to T_d

Upon heating to T_d, wax softens again and thus removes its constraint on silicone, which results in shape recovery in this representative unit. In this step of simulation, initial loads are residual stress after instant recovery, and the properties of wax should be changed accordingly.

In considering running time, memory usage and convergence speed, an iterative solver, namely PowerSolver, PCG, was used in simulation.

- ***Results***

Figure 3.5(a-d) reveals a typical shape evolution process resulted by simulation. The SMH (Fig. 3.5a) is compressed by 20% at T_d (Fig. 3.5b). When it is cooled down to room temperature ($<T_m$), constraint is removed. Instant recovery is elastic, but only partially due to the constraint from hard inclusion (Fig. 3.5c). This is the programming process, in which instant recovery (related to shape fixity ratio) is one of the important parameters. It is apparent that given particular materials, shape fixity ratio depends on the volume

fraction of transition component. Figure 3.5 (e) and (f) reveal the stress fields at the maximum compression at T_d and after programming.

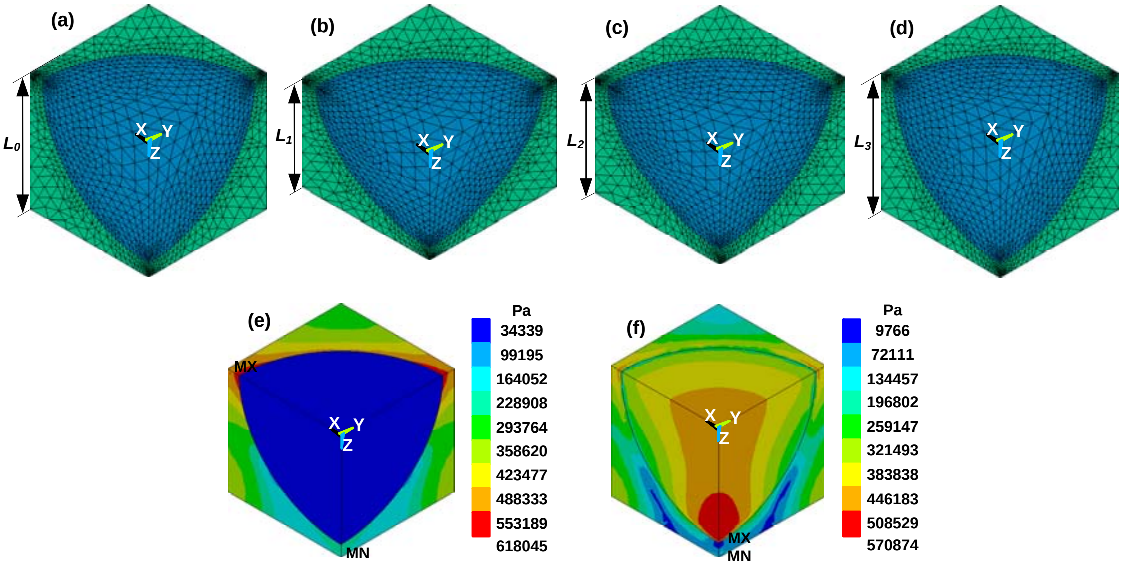

Figure 3.5 Shape evolution. (a) Initial shape; (b) after being compressed to maximum strain; (c) after unloading; (d) after shape recovery. (e) von Mises stress at maximum compression; (f) von Mises stress after unloading.

The next step is the shape recovery process. There are two typical recovery modes (Yang *et al.* 2006). One is called free recovery, in which the sample is free from any constraint during heating; while the other is called constrained recovery, in which the shape of sample is fixed upon heating.

In the case of free recovery, shape recovery ratio, which can be worked out from Fig. 3.5(d), is the major concern. In constrained recovery, the shape recovery stress is of our interest.

Shape fixity ratio, R_f, and shape recovery ratio, R_r, can be calculated by,

$$R_f = \frac{L_0 - L_2}{L_0 - L_1} \times 100\% \tag{3.9}$$

$$R_r = \frac{L_3 - L_2}{L_0 - L_2} \times 100\% \tag{3.10}$$

where L_0 is the original height (Fig. 3.5a); L_1 is the height at the maximum deformation (20% compression in this particular case) (Fig. 3.5b); L_2 is the height after unloading, i.e., the residual height in Fig. 3.5 (c); and L_3 is the height after shape recovery by heating (Fig. 3.5d). Eqns. (3.9) and (3.10) can be easily obtained from Eqns. (2.2) and (2.3).

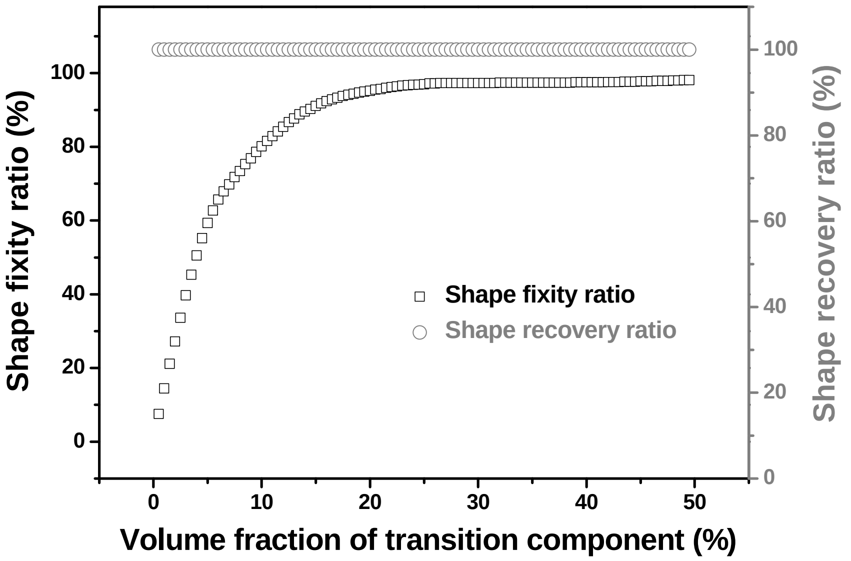

Figure 3.6 Shape fixity/recovery ratio vs. volume fraction of transition component relationship.

Figure 3.6 reveals the relationship between shape fixity/recovery ratio and volume fraction of transition component. It can be seen that shape fixity ratio increases with the increase of volume fraction of transition component. With a volume fraction above about 20%, a shape fixity ratio over 90% is obtained. On the other hand, shape recovery ratio is always 100%, even when the volume fraction of transition component reaches 49.5%, which is the highest volume fraction in this simulation.

Although a higher volume fraction of transition component is in favor for a higher shape fixity ratio, from engineering practice point of view, it actually prevents good shape recovery, since the continuity of elastic matrix is largely destroyed when the volume fraction of transition component is too high, and thus full shape recovery becomes difficult. As such, in current simulation, the maximum volume fraction of transition component is limited to below 50%.

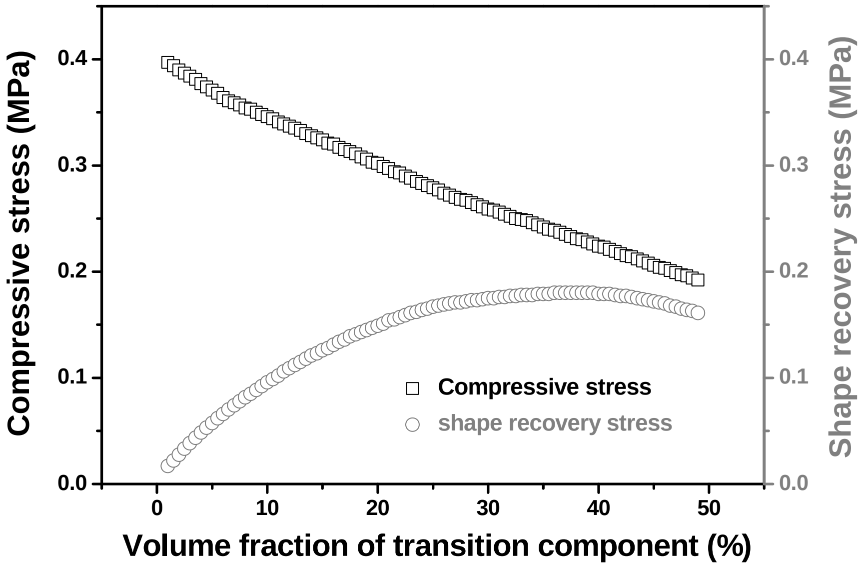

Figure 3.7 Maximum compressive stress in programming (at 20% compression and T_d) and compressive stress after constrained recovery against volume fraction of transition component relationships.

Figure 3.7 presents the maximum compressive stress in programming to 20% compression at T_d and the compressive stress in constrained recovery upon heating to T_d at different volume fractions of transition component. It is clear that a lower compressive stress is required in a S-W with more wax content following virtually a liner fashion. On the other hand, recovery stress does not follow a monotonic trend against wax content. It increases with the increase in volume fraction of transition component until about 40% of transition component. At this point (i.e., 40% volume fraction of wax), the maximum recovery stress is about 80% of the maximum compressive stress in programming. With more than 40% of wax, recovery stress starts to decrease gradually.

Although the simulation above is still preliminary and largely meant for qualitative understanding of the performance of SMHs based on some special situations, Fig. 3.6 and Fig. 3.7 do reveal the general trend and provide us with basic knowledge in design of SMHs.

3.4 Summary

In this chapter, the concept of SMH is proposed. The underlying mechanism behind the SME in SMHs is discussed schematically and then further investigated by mean of numerical simulation (via finite element analysis). The conditions to achieve good SME in SMHs are obtained. The influence of volume fraction of transition component on shape fixity ratio, shape recovery ratio, maximum programming stress and recovery stress are studied. This chapter provides a basic understanding of SMHs and serves as a platform for chapters followed.

Chapter 4 Multi-functional Silicone-Wax Shape Memory Hybrids

In this chapter, we demonstrate the simplicity in design and fabrication of multi-functional shape memory hybrids (SMHs) to realize all types of shape memory phenomena using two commonly used materials, namely silicone and wax, which as an individual does not have any shape memory effect (SME) at all within the temperature range of our concern.

4.1 Materials and sample preparation

High stability and excellent elasticity is required for the elastic component in a SMH in order to achieve high shape recovery. Silicone, also known as polysiloxane or polymerized siloxane, is an inorganic polymer, in which the backbone is assembled by means of alternating silicon and oxygen atoms without any carbon atoms. Different organic side groups, such as methyl, ethyl and phenyl, can either link to the silicon atoms of the backbone, or bond two or more backbones together. A typical structure of silicone is illustrated in Fig. 4.1 (a).

In general, a silicone's properties can be tailored in a wide range by means of adding in different types of side groups, varying the length of silicon-oxygen backbone, and adjusting the extent of crosslinking. From liquid and gel to soft rubber and hard solid, silicones can be in various forms. Silicone is thermally and chemically stable and water repellent, in addition to its well-known high elasticity.

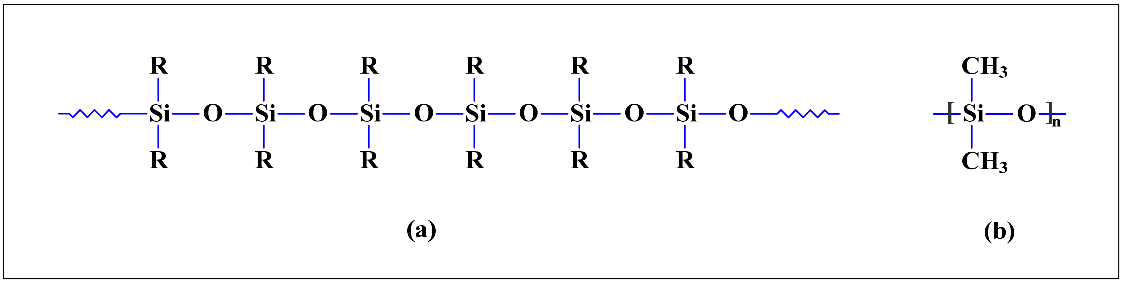

Figure 4.1 Schematic illustrations of silicone structure in generic form (a) and the special form of Sylgard 184 silicone (b).

As for SYLGARD® 184 silicone elastomer kit from Dow Corning Corporation, U.S.A, it is highly elastomeric with a linear polydimethylsiloxane (PDMS) structure as illustrated in Fig. 4.1 (b). It is highly compatible with many materials and can well maintain its excellent elasticity within a wide temperature range from -50°C to 200°C. Some major technical data of this silicone are listed in Tab. 4.1. SYLGARD® 184 silicone elastomer kit comes with two parts, namely base material and curing agent, both in liquid form. A volume ratio of 10 (base material) to 1 (curing agent) is recommended for mixing of them before curing. The densities of both are essentially about the same. In addition to mixing ratio, the required curing time also varies depending on the curing temperature. For instance, it is recommended to be 24 hours at 23°C, 4 hours at 65°C, 1 hour at 100°C, and 15 minutes at 150°C. Such variation provides us with additional flexibility in fabricating various types of hybrids based on this silicone. Given these advantages, SYLGARD® 184 was selected for the elastic component.

Table 4.1 Technical data of SYLGARD® 184 (from Dow Corning Corporation).

Property	Unit	Value
Viscosity at 23^{o}c (base)	mPa.S	5500
Mixing ratio by weight (base: curing agent)		10:1
Viscosity at 23^{o}c, immediately after mixing with curing agent	mPa.S	4000
Pot life at 23^{o}c	Hours	2
Tensile strength (cured 4 hours, at 65^{o}c)	MPa	7.1
Elongation at break (cured 4 hours, at 65^{o}c)	%	140
Specific gravity at 23^{o}c (cured 4 hours, at 65^{o}c)		1.05
Volume resistivity (cured 4 hours, at 65^{o}c)	Ohm.cm	2.9×10^{14}
Coefficient of thermal conductivity	W/(m K)	0.17
Linear coefficient of thermal expansion (cured 4 hours, at 65^{o}c)	10^{-6}/K	325

Alkane hydrocarbon is also known as paraffin. The general formula of paraffin is C_nH_{2n+2}. Paraffin wax is a solid form of paraffin with *n* between 20 and 40. Paraffin wax has a saturated structure and is very inert to most commonly used chemical reagents. On the other hand, paraffin wax has a high fraction of crystalline and its melting temperature can be modulated by changing *n* in the molecular formula. Another common feature in waxes is their high thermal expansion coefficient, especially during melting [volume expansion up to 22% according to (Bueche 1973)].

Paraffin wax (PW) (Agar L4133 Pelleted Paraffin Wax, Agar Scientific Limited, England) and low melting point wax (LMPW) (Agar L4182 Low Melting Point Wax, Agar Scientific Limited, England) have nominal melting temperatures of $56^{o}C$ and $45^{o}C$, respectively. They were selected as the transition component in current study.

For hybrids made of immiscible polymers, dispersion and coalescence of inclusions are two counteracting processes during mixing. Deformation and breakup of inclusions under an external force, such as stirring and/or vibration, tends to result in a mixture with fine sized inclusions. On the other hand, the inherent immiscibility tends to merge inclusions together, i.e., coalescence of dispersed inclusions (Lin and Guo 2007; Mighri and Huneault 2006).

In hybrid fabrication, transition inclusion (i.e., LMPW, PW) and base material (liquid silicone elastomer base) were weighted according to the specified volume ratio and then put into a beaker together. Subsequently, the mixture was heated slightly above the melting temperature of wax in an oven. Stirring at a high speed and for about ten minutes at the elevated temperature was proved to be an effective approach for good dispersion of wax. To prevent wax from aggregating together, we must keep on stirring during cooling until the wax inclusions turn into solid. After the mixture was cooled down to room temperature (about $23^{o}C$), curing agent was added in and mixed thoroughly again. Subsequently, the mixture was poured into a Polytetrafluoroethylene (PTFE) mold with the specified dimensions.

During mixing, many air bubbles may be generated and moisture from air may be trapped inside. A vacuum de-airing process was necessary by means of placing the mold in a vacuum chamber with a pressure of 8 mbar at room temperature for ten minutes, and then in air for another two minutes. Due to high viscosity nature of the mixture, this process may be repeated several times to ensure perfect mixing. In the last step, the mold was kept in air at room temperature for twenty four hours for curing.

Table 4.2 Compositions of hybrids.

Sample name	Silicone	PW	LMPW	GF
S-PW15	85%	15%	-	-
S-PW20	80%	20%	-	-
S-PW25	75%	25%	-	-
S-PW30	70%	30%	-	-
S-PW35	65%	35%	-	-
S-PW40	60%	40%	-	-
S-PW15-LMPW15	70%	15%	15%	-
S-PW29-GF1	70%	29%	-	1%

A series of samples with different volume fractions of transition inclusions were fabricated. Table 4.2 lists the compositions and abbreviations of some typical samples. Unless otherwise stated, volume ratio is applied in this whole dissertation. Here, GF stands for glass fiber (about 2 mm long and 7 μm in diameter). The fabrication procedure of S-PW29-GF1 is about the same as other hybrids. GF was loaded into the mixture right before adding in curing agent to ensure that there was no GF inside the transition inclusions.

4.2 Thermal behavior

4.2.1 Differential scanning calorimetry

Differential scanning calorimetry (DSC, TA DSC Q200) tests were carried out to measure the transition temperatures of fabricated hybrids. Pure silicone and PW were also tested for comparison. Samples weighted about 10 mg were tested between -10°C to 110°C at a heating/cooling ramp of 8°C min^{-1}. Experimental results are summarized in Figure 4.2. As expected, silicone is very stable within this temperature range, while peaks/troughs are observed in hybrids and PW. With more PW content, peak/trough becomes larger, but still mainly within the same temperature range as PW and even the shape is similar. Obviously, these peaks/troughs are the result of the filled PW.

The corresponding latent heat of hybrids and PW can be estimated from their respective heating curve in Fig. 4.2. The results are summarized in Fig. 4.3. As we can see, if mass percentage of PW is adopted, latent heat in hybrids is a linear function of PW content. According to Fig. 4.2 and Fig. 4.3, we may conclude that silicone and PW are immiscible, i.e., silicone and PW are well separated, and there is not much strong interaction between them even at the interface. As such, different from shape memory polymers (SMPs) in which the transition temperature may highly depend on the volume fraction of transition segment (Lendlein and Kelch 2002), the transition temperature of these hybrids is more or less determined only by the softening (melting) temperature of the transition component. This provides us with the advantage that one can well predicate the performance/ properties of a SMH even in the early design stage.

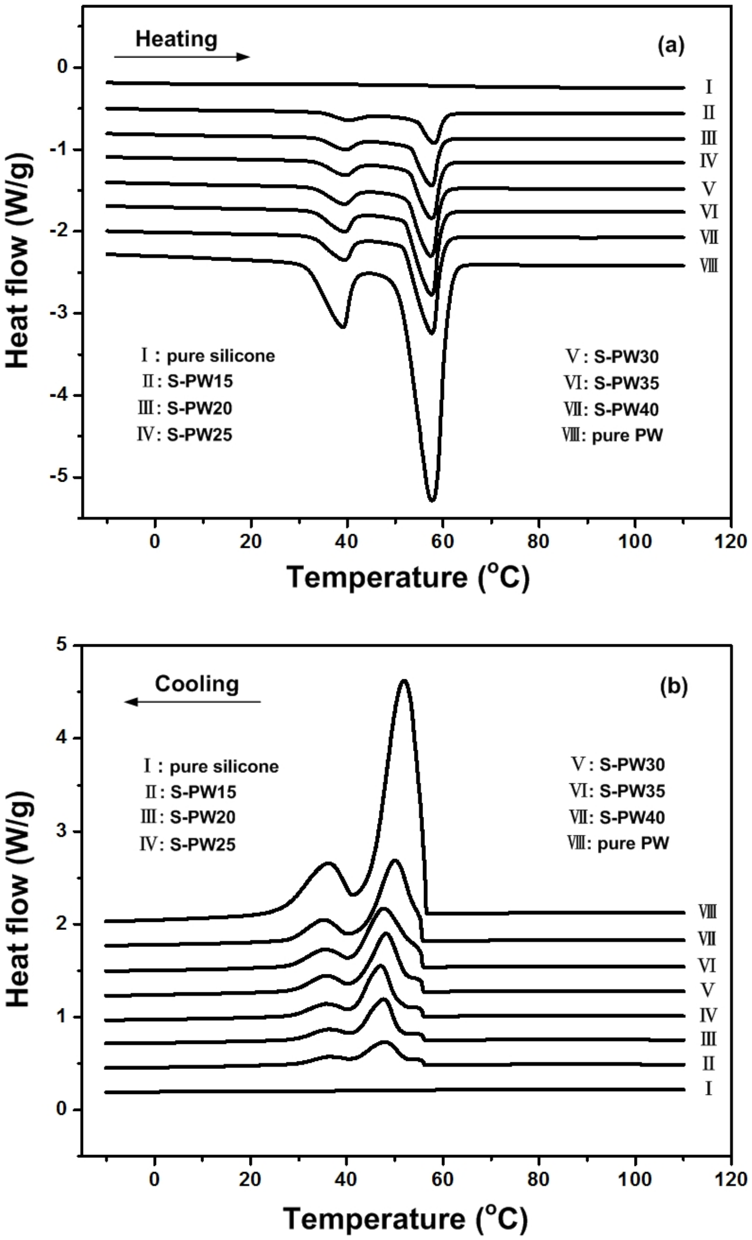

Figure 4.2 DSC results of hybrids (together with silicone and PW) upon heating (a) and cooling (b).

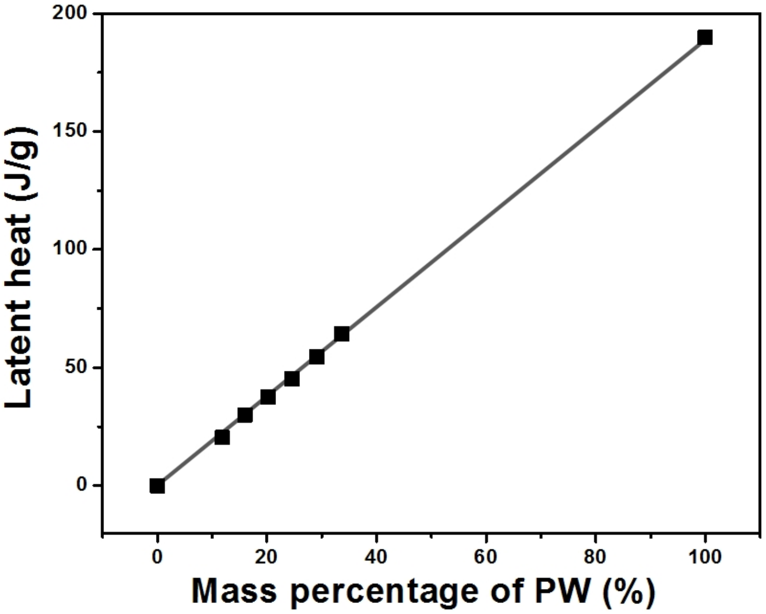

Figure 4.3 Latent heat vs. mass percentage of PW relationship.

It is also noticed that the transition (in both melting and consolidation) does not appear as one single peak/trough, but two, in which one is bigger and the other is much smaller. Two different wax crystalline phases and/or melting/crystallizing of different wax phases may be the reasons behind this (Krupa *et al.* 2007; Luyt and Krupa 2008).

The DSC results of S-PW15-LMPW15 and S-PW29-GF1 are presented in Fig. 4.4 together with PW and LMPW for reference. Two temperature peaks in S-PW15-LMPW15 locate at totally different positions as compared with those in LMPW and PW. This convoluted DSC patterns may be from some factors, such as phase mixing and imperfect crystals, in mixture of similar materials (in this case wax). On the other hand, the peak/trough temperatures of S-PW29-GF1 are very close to that of PW, which indicates that glass fiber has limited effect on the transition temperatures, if not none.

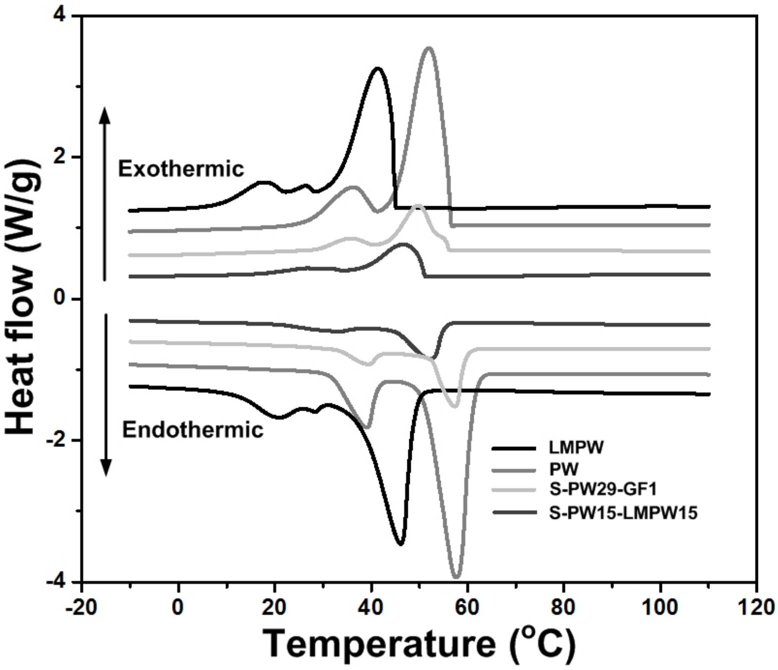

Figure 4.4 DSC results of S-PW15-LMPW15, S-PW29-GF1, PW and LMPW.

4.2.2 Dynamic mechanical analysis

Dynamic mechanical analysis (DMA) is a commonly used technique for characterization of materials by studying their modulus, damping and damping factor (tan δ) during, in most occasions, gradually heating (Sepe 1998; Wunderlich 2000). All DMA experiments reported in this dissertation were carried out on a DMA Q800 (TA) in single cantilever mode. Thicker samples are necessary when evaluating lower modulus materials, and vice versa. Hence, a standard sample size is 30×12×4 mm in current study. The applied heating ramp was 2°C/min and vibration frequency was 1 Hz.

It is revealed in Fig 4.5 that, as expected, the storage modulus of pure silicone does not change at all within the whole testing temperature range (from room temperature to

125°C). Furthermore, with the increase of PW content in S-PW, the storage modulus (a measure more or less equivalent to stiffness in current study) of a hybrid increases at room temperature since PW is harder than silicone. Upon heating, the storage modulus of all S-PW hybrids decreases in a two-step fashion (i.e., a big drop followed by a small one). Melting, and thus softening, of PW is the reason behind. Apparently, this two-stage phenomenon matches well with the dual-trough feature observed in DSC tests (Fig. 4.2a).

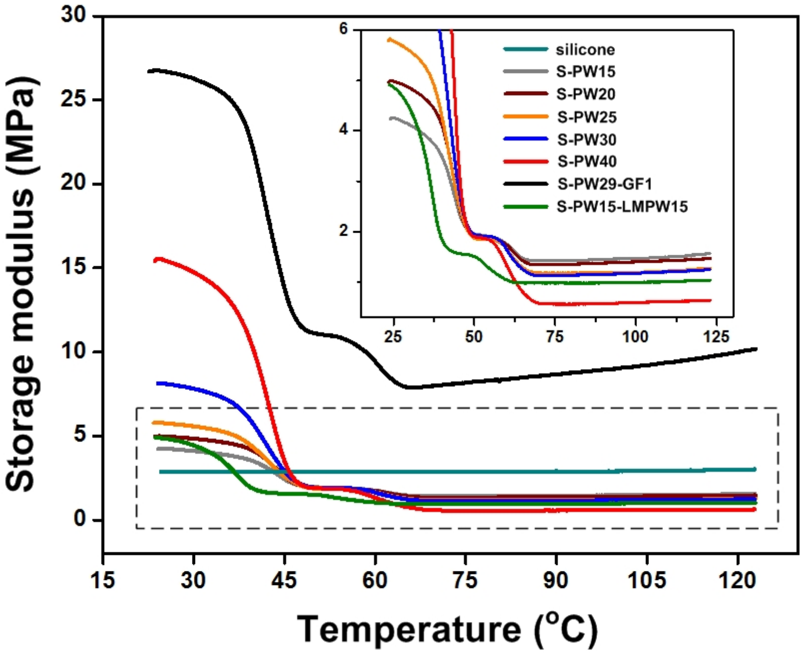

Figure 4.5 Storage modulus vs. temperature curves of S-PW hybrids together with pure silicone as reference. Inset: zoom-in view of the dashed-line area (without silicone).

On the other hand, with more PW content, the storage modulus decreases more, so that the lowest storage modulus is observed in S-PW40 which has the highest PW content. Upon further heating, the storage modulus starts to increase, but only slightly, due to continuous thermal expansion of PW. By adding in only 1% volume fraction of glass fiber, not only the overall storage modulus increases a lot (which is well understood), but also the increase in storage modulus upon further heating becomes remarkable. High stiffness of glass fiber effectively prevents isotropic expansion in a hybrid, so that the volume expansion of PW results in a high internal pressure instead. Consequently, more increase in storage modulus is observed.

S-PW-LMPW shares similar trend as in S-PWs, despite of the interaction between PW and LMPW, which affects the exact transition progress.

4.3 Morphology

Scanning electron microscope (SEM) (JEOL JSM-5600LV), which is one of the most versatile instruments to examine morphology and chemical composition of materials (Zhou and Wang 2007), was employed to study the morphology of hybrids. Second electron imaging (SEI) is commonly applied to provide excellent topographical images with fine details of a sample. Another useful mode is back-scattered electron (BSE) reflection. Since an element with higher atomic number provides stronger BSE signal, the area occupied by such an element turns to be brighter. Different chemical compositions can be detected from the contrast between different areas. Hence, back-scattered electron imaging (BSEI) is another useful technique (Klimek and Pietrzyk 2004). Characteristic x-rays (energy-dispersive spectrometry or EDS) are techniques to identify the composition and to measure the abundance of elements in a sample. BSEI is often used together with EDS in SEM.

Cryo-fractured silicone surface was revealed by means of SEI and BSEI (Fig. 4.6). Figure 4.6(a) reveals that the surface is relatively flat, continuous and compact. Figure 4.6(b) confirms that it is homogenous since there is no apparent contrast in the whole detecting area.

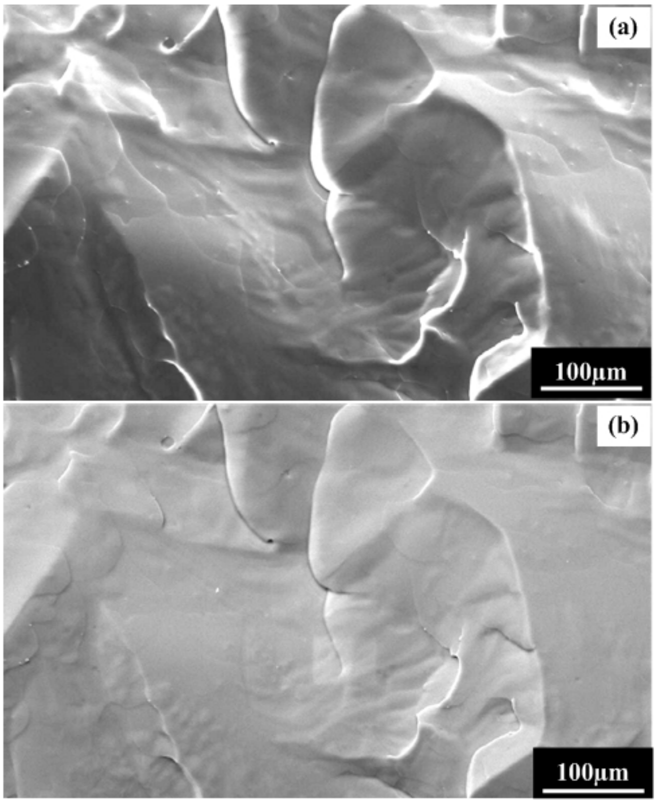

Figure 4.6 SEM images of pure silicone. (a) SEI; (b) BSEI.

As we know, the silicone used in current study is composed by elements of silicon, oxygen, carbon and hydrogen, while the compositions of wax have elements of hydrogen and carbon. The mean atomic number of silicone should be higher than that of wax, i.e., wax should be darker than silicone in a BSEI image. This is verified in Fig. 4.7. Note that the detected Au element in EDS result is the result of gold coating. Combining the BSEI and EDS results, we may safely conclude that the white base is silicone, while the dark areas are PW inclusions. As we can see, PW inclusions with a size of about 10 μm or less are well distributed within silicone. Some little holes are observed in Fig. 4.7(a). Most likely, they are formed upon removal of PW inclusions during sample preparation (cryo-fracture).

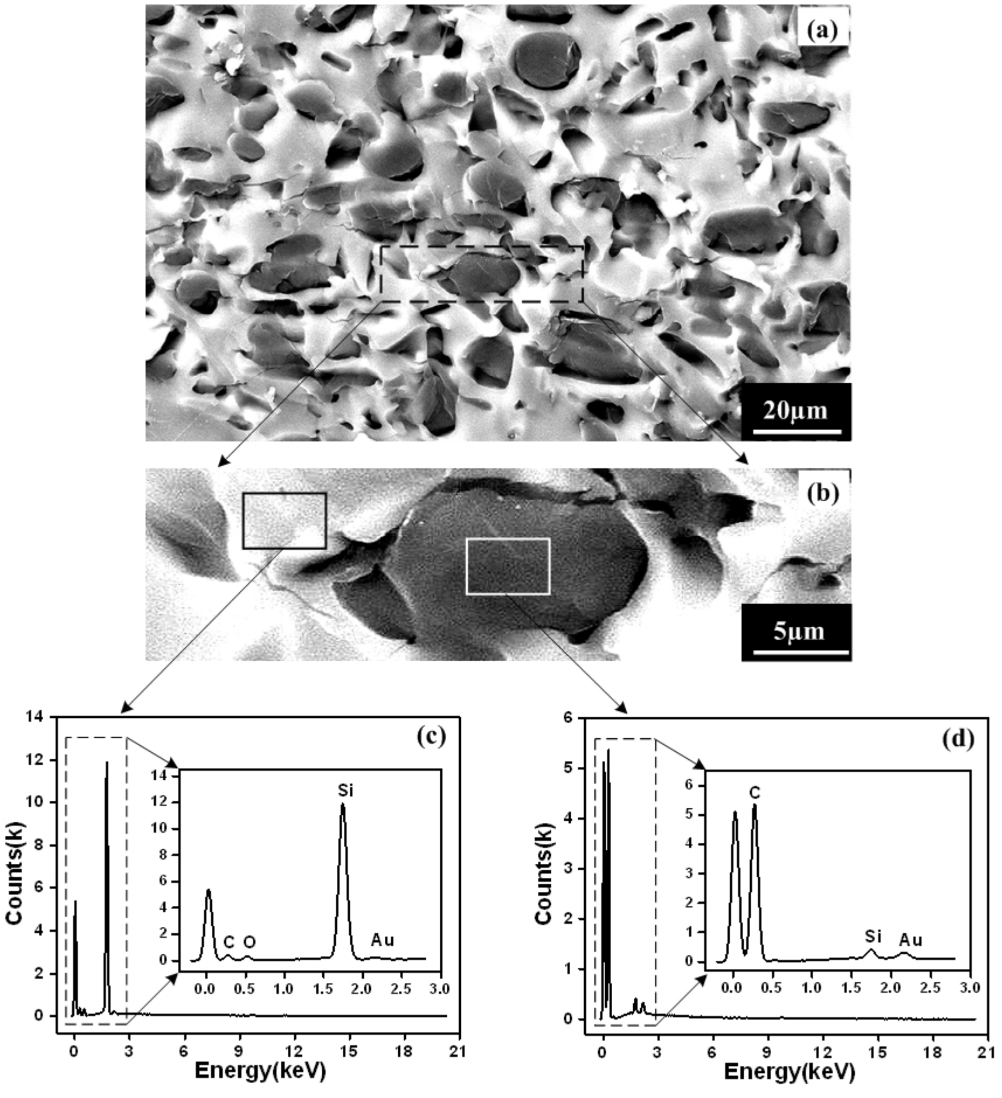

Figure 4.7 SEM images of S-PW30. (a) BSEI; (b) zoom-in view of the marked rectangular area in (a); (c) and (d) EDS results of two patches marked in (b).

4.4 Mechanical behavior

Mechanical behavior of hybrids was characterized by an Instron 5569 Universal Testing Machine in compression mode at a strain rate of 0.1%/s. The size of as-fabricated cylindrical shaped samples was 19 mm long and 20 mm in diameter. The experimental results of three S-PWs, namely S-PW20, S-PW30 and S-PW40, in cyclic uniaxial compression (to 5%, 10%, 15%, 20%, 25%, 30%, and 35% strains in an increasing order) at three different temperatures (namely, 22^{o}C, 60^{o}C and 100^{o}C) are presented in Figs. 4.8-4.10. Unless otherwise stated, hereinafter, the stress/strain is engineering stress/strain.

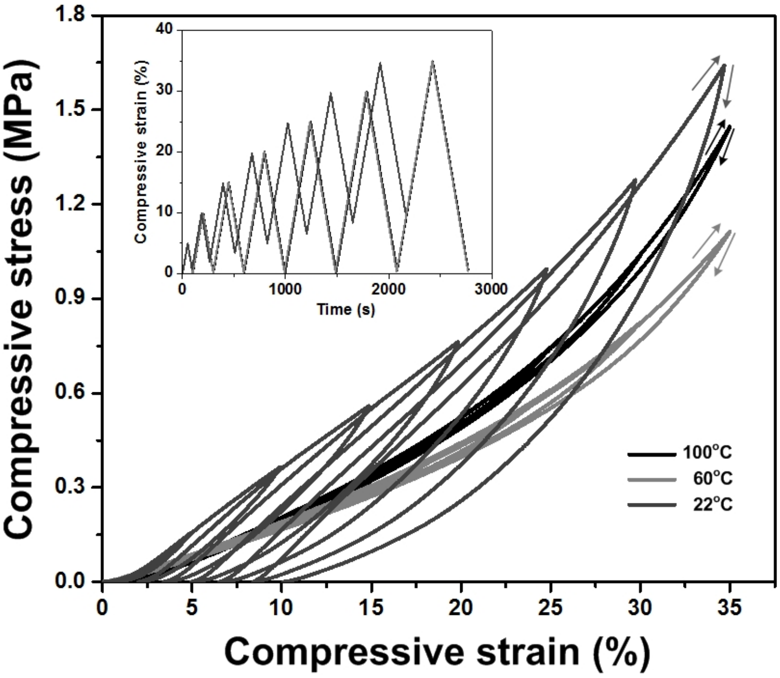

Figure 4.8 Compressive stress vs. compressive strain curves of S-PW20. Inset: recorded strain vs. time relationships.

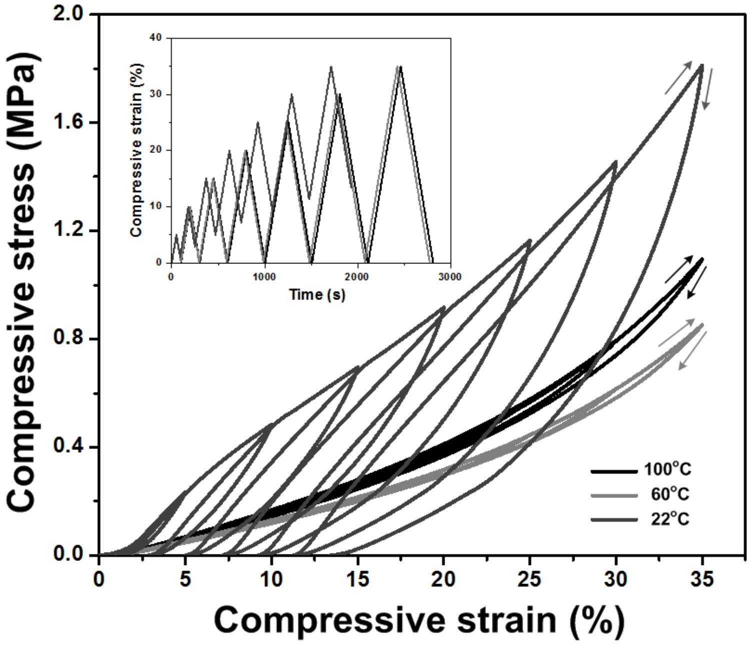

Figure 4.9 Compressive stress vs. compressive strain curves of S-PW30. Inset: recorded strain vs. time relationships.

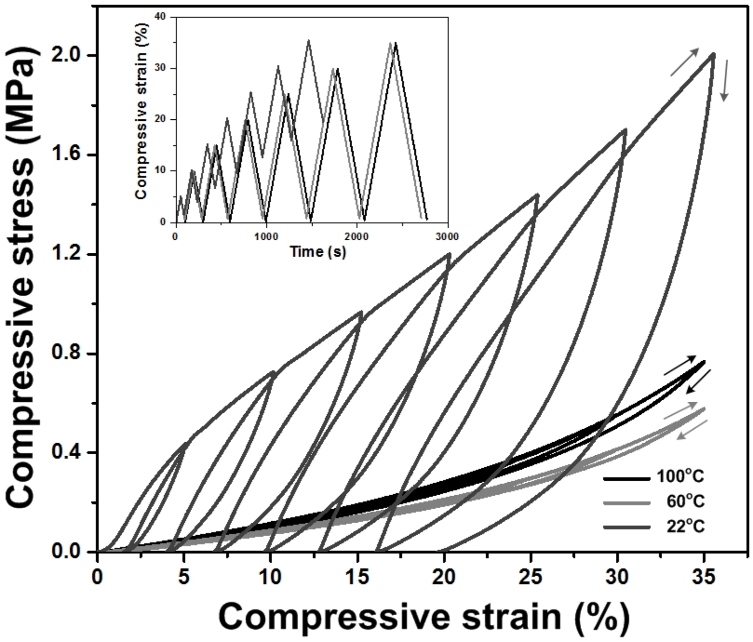

Figure 4.10 Compressive stress vs. compressive strain curves of S-PW40. Inset: recorded strain vs. time relationships.

As expected, all S-PW hybrids become softer with the increase of testing temperature. Furthermore, with more PW content, a piece of S-PW hybrid is harder at 22^{o}C (because at this temperature, PW is solid and hard), but softer at higher temperatures (as PW melts). At both 60^{o}C and 100^{o}C, S-PWs are actually rubber-like in response to compression. Even being compressed to 35% strain, there is not any apparent residual strain after unloading (to closely examine residue strain, refer to the inset). The hysteresis is also small (arrows indicate loading and unloading paths). This is due to that at 60^{o}C and above, PW is liquid so that the resistance is largely from silicone, which is essentially elastic foam (with pores filled with liquid PW).

However, at 22^{o}C, remarkable residual strain is observed in all three S-PWs, since solid PW inclusions are plastically deformed upon compression, and thus deformed hard inclusions function as constraint to prevent shape recovery of silicone foam. It is apparent that the more is PW content in an S-PW, the higher is the residual strain when compressed to the same maximum strain. To better reveal this point, the relationship between the maximum compression strain vs. the residual strain after subsequent unloading is plotted in Fig. 4.11.

A close-look reveals that at 100^{o}C, S-PWs are actually slightly harder than that at 60^{o}C. Again thermal expansion of PW induced hardening effect should be the reason behind this seemingly surprising finding. This finding is actually consistent with the DMA results reported in Fig. 4.5.

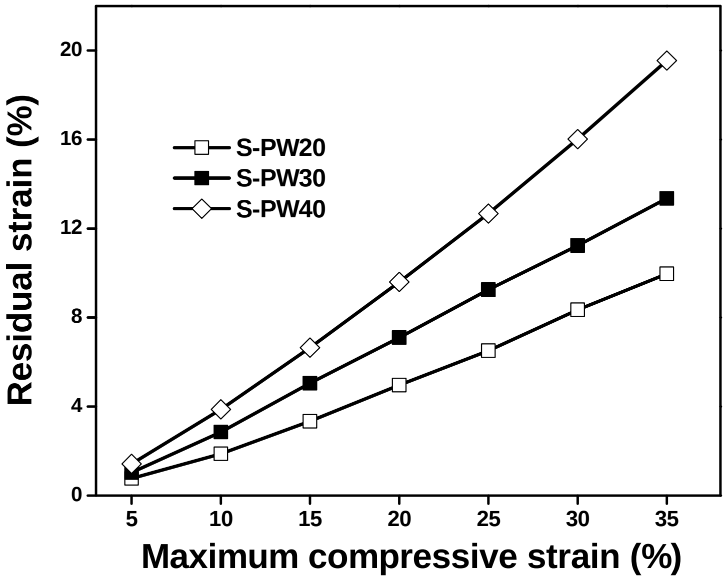

Figure 4.11 Maximum compression strain vs. residual strain after subsequent unloading.

4.5 Shape memory effect

As in SMPs, the SME may appear in the forms of dual-SME, triple-SME and mechanical two-way SME. In this section, we examine them one by one in our hybrids.

4.5.1 Dual-shape memory effect

- ***Demonstration***

Figure 4.12 shows the shape recovery sequence in a piece of S-PW30 hybrid upon immersing into 65^{o}C water. The as-fabricated hybrid was a straight piece. It was folded by 180^o in 65^{o}C water and then cooled back to room temperature with the bent shape maintained. The sample slightly recovered after the constraint was removed (Fig. 4.12a). Full shape recovery was observed after immersing it for 16 seconds in 65^{o}C water, as shown in Fig. 4.12 (b) to (f).

Although pre-distortion (i.e., programming) can be carried out at low temperatures (e.g., room temperature as revealed in Fig. 4.8 to 4.9), the shape fixity ratio is low (refer to Fig. 4.11). Programming at high temperatures (above the transition temperature) for the dual-SME is preferred if high shape recovery strain is required.

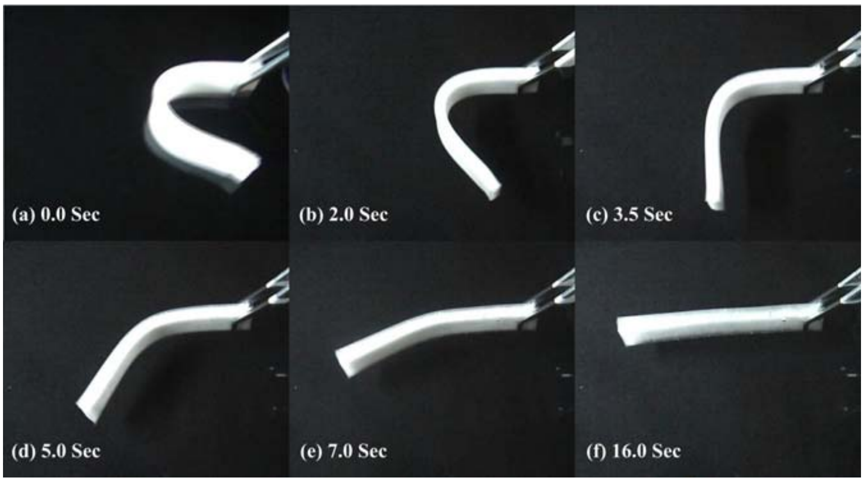

Figure 4.12 Snapshots of shape recovery sequence in a piece of S-PW30 hybrid upon immersing into 65°C water.

- ***Morphology***

As revealed in Fig. 4.7(a), in as-fabricated S-PW30, spherical shaped PW inclusions are more or less evenly distributed within silicone matrix. However, after being programmed into a curved shape by means of bending at high temperatures and then cooling, PW inclusions appear more in elliptical shape and virtually form circulars surrounding a center (Fig. 4.13a). It is these stiffer elliptical PW inclusions and their special orientation that provide resistance to shape recovery at room temperature. At above melting temperatures, liquid PW can hardly resist the elastic recovery of silicone, and thus, as revealed in Fig. 4.13 (b), after shape recovery, PW inclusions return spherical shape without any particular trend in terms of orientation.

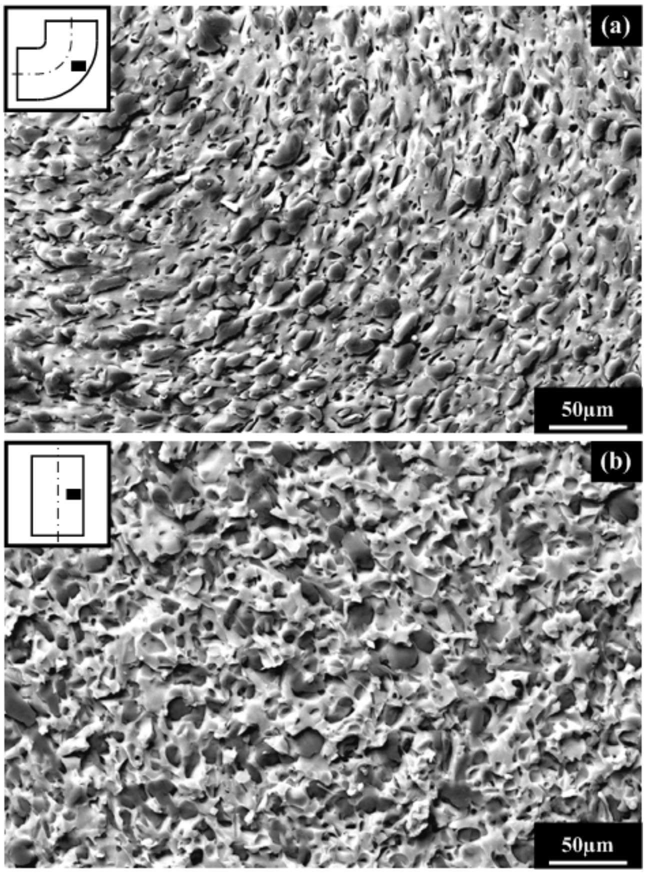

Figure 4.13 SEM images (BSEI) of S-PW30. (a) after programming by bending; (b) after heating for shape recovery. Inset illustrates the relative location of the examined area within the tested sample.

Instead of bending in programming, Fig. 4.14 reveals morphology difference in PW inclusions after programming by means of uniaxial tension (in the vertical direction) and after heating for shape recovery. It is apparent that after programming, all PW inclusions are in elliptic shape with the long axis along the tension (vertical) direction. After shape recovery, all PW inclusions turn back to circular shape. These two experiments confirm the mechanism behind the SME in hybrids from the morphology aspect.

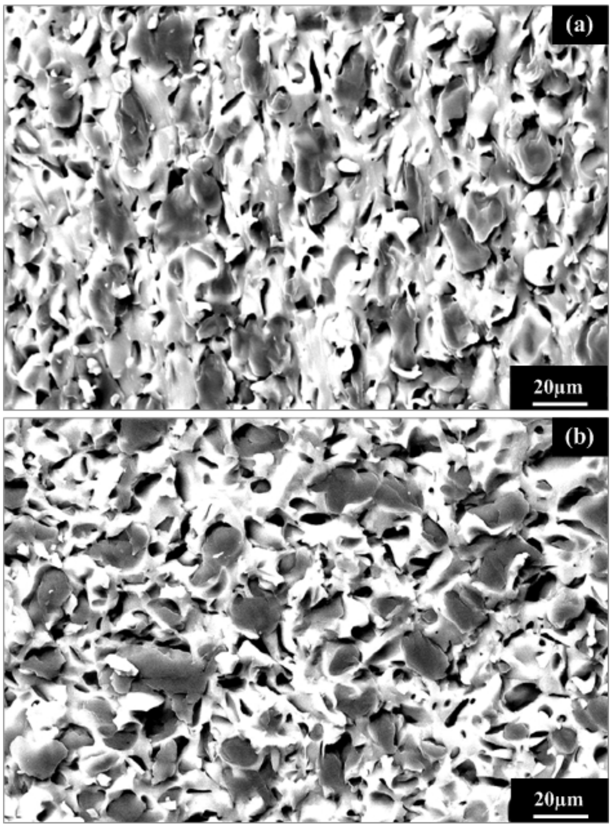

Figure 4.14 SEM images of S-PW30 after programming (stretching in the vertical direction) (a) and shape recovery (b).

- ***Characterization***

Following the typical thermo-mechanical procedure for characterizing the SME illustrated in Fig. 2.5, the shape fixity ratio and shape recovery ratio of S-PW hybrids under different maximum pre-strains (in compression) were determined. In order to obtain reliable and repeatable results, heating/cooling speed needs to be well controlled to ensure good temperature uniformity in these hybrids. The Instron 5565 Universal Testing

Machine was modified with a heating/cooling water bath for this purpose. Figure 4.15 illustrates the modified setup. A hard thermal insulation layer was applied to reduce the speed of heat transfer between the bottom clamp and water bath.

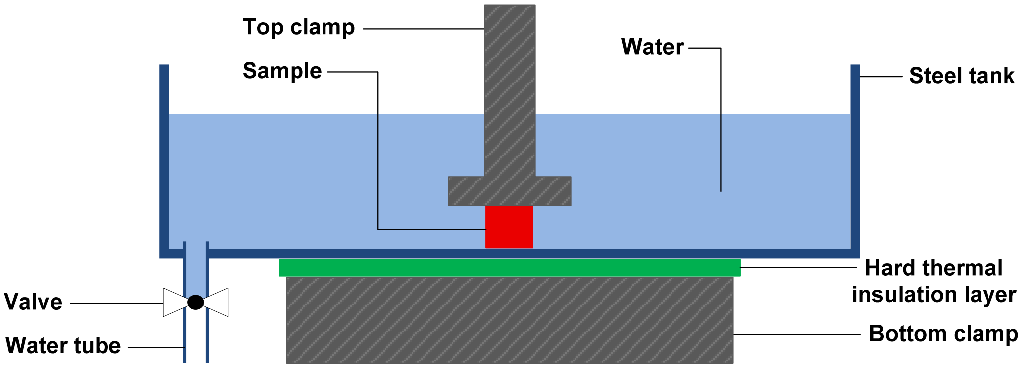

Figure 4.15 Schematic illustration of the modified setup.

Taking the experiment of 50% maximum pre-strain on S-PW30 (refer to Fig. 4.16a1 and b1 for dimensions of the sample) as an example, the experimental procedure is as following.

- 70°C hot water is poured into the tank to heat up the sample. A temperature controllable heating device is used to keep the temperature of water at around 70°C.
- After 10 minutes for temperature stabilization in the sample and top clamp, a compression strain of 50% is applied at a strain rate of 0.1%/s. Refer to Fig. 4.17 curve AB for the recorded stress vs. strain relationship in this step.
- The maximum compression strain is held for 30 minutes. In the mean time, the hot water is drained out and the heating device is moved away. Subsequently,

room temperature water is poured into the tank. Temperatures at three locations within the sample, namely bottom, middle and top, are monitored using three thermocouples. After the water in the tank is drained out, new room temperature water is poured in. This pouring-draining cycle is repeated several times until the whole sample reaches 22°C (room temperature). Straight line BC in Fig. 4.17 corresponds to the strain vs. stress relationship in this step.

- Subsequently, the sample is fully unloaded at a strain rate of 0.05%/s, which is much slower as compared with that in compression (refer to curve CD in Fig. 4.17). This much lower strain rate is applied to ensure full stress relaxation/redistribution. Figure 4.16(a_2) and (b_2) present top-view and side-view pictures of the programmed sample.
- In the shape recovery step, the programmed sample is heated to 70°C again in hot water (indicated by curve DA in Fig. 4.17). The pictures of real recovered sample are presented in Fig. 4.16(a_3) and (b_3).

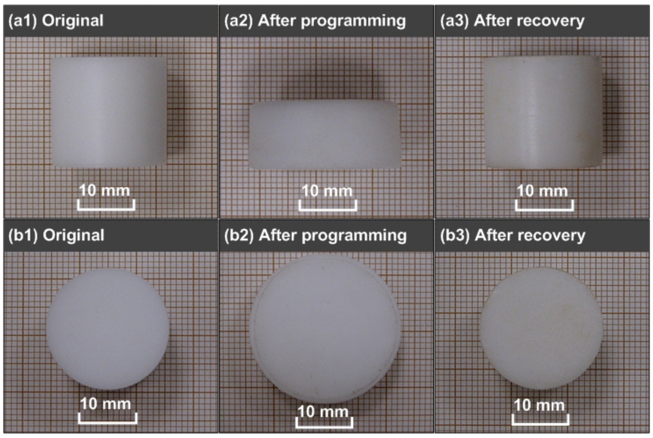

Figure 4.16 Shape change in S-PW30 during testing with a maximum compressive strain of 50%. (a) side-view, and (b) top-view.

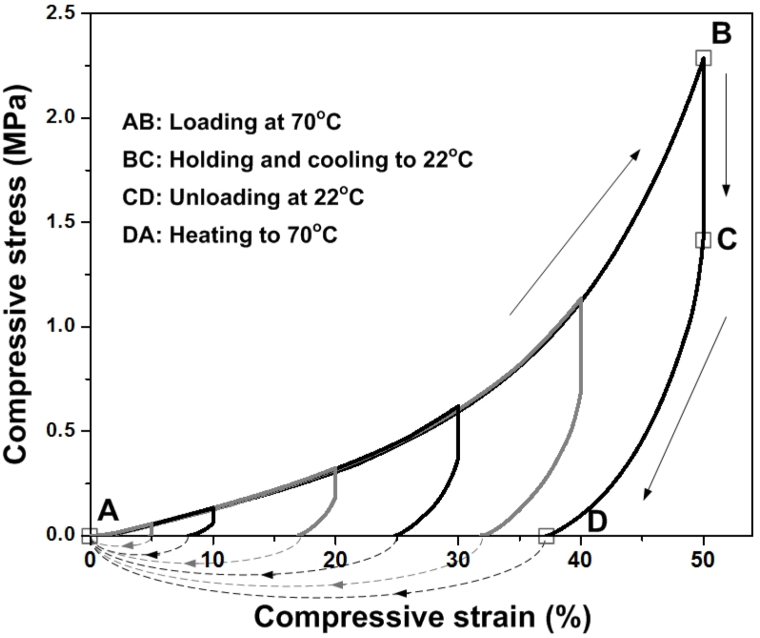

Figure 4.17 Typical stress vs. strain results of S-PW30 hybrid with different maximum compression strains.

Following this procedure, S-PW30 was programmed by compression into five other maximum strains, namely 5%, 10%, 20%, 30%, and 40% (as shown in Fig. 4.17). Other S-PWs were also tested in this way. All experimental results are summarized in Fig. 4.18. It can be seen in Fig.4.18 that all S-PWs (up to with 40% PW) are able to fully recover their original shape even being programmed by applying a maximum compression strain of 50%. Based on Fig. 4.18, the shape fixation ratio vs. volume fraction of PW relationships at different maximum compression strains are obtained and plotted in Fig. 4.19. For a clear view from a different aspect, in Fig. 4.20, the results are re-presented in terms of the shape fixation ratio vs. maximum compression strain at different PW contents (in terms of volume fraction).

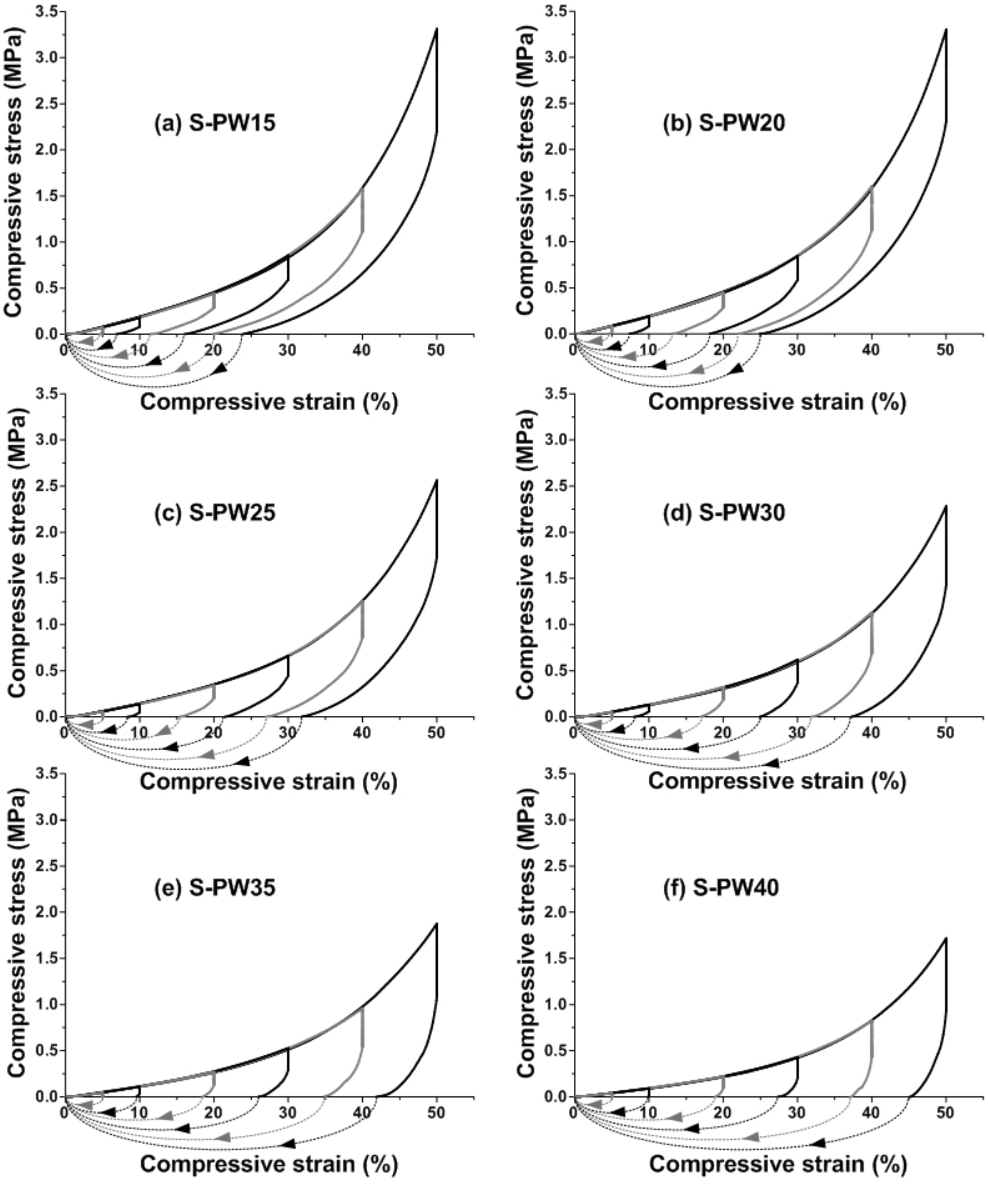

Figure 4.18 Summary of experimental results of S-PW hybrids.

It is clear that at a given maximum compression strain, the shape fixity ratio increases with the increase of PW content. On the other hand, for a give S-PW, with the increase in the maximum compression strain, the shape fixity ratio decreases. As such, the requirement on the maximum strain in programming for high shape fixity ratio and high recoverable strain are opposite.

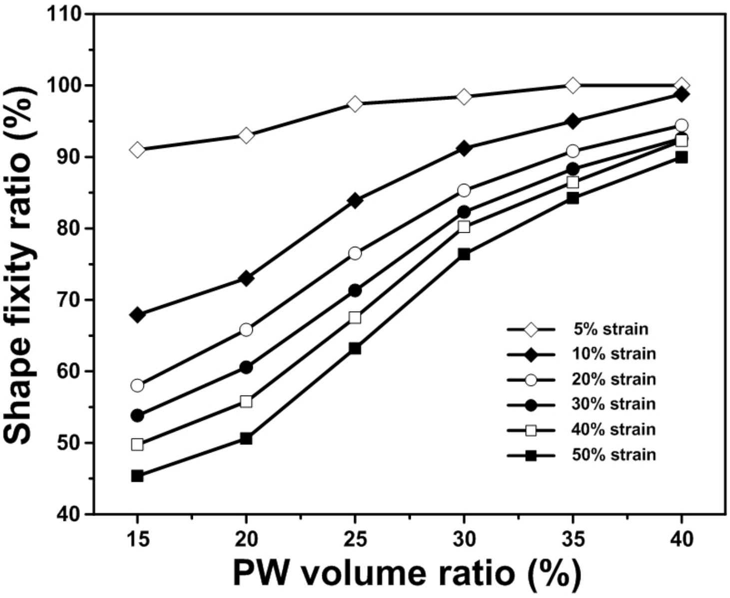

Figure 4.19 Shape fixation ratio vs. volume fraction of PW relationships at different maximum compressive strains.

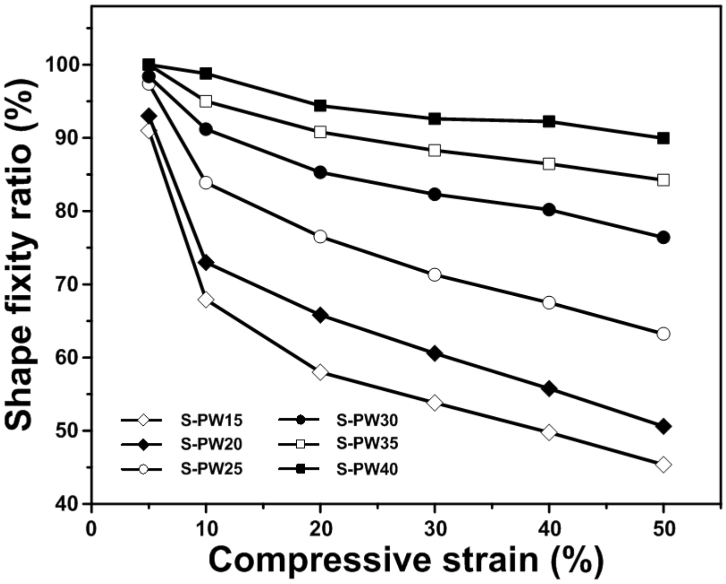

Figure 4.20 Shape fixation ratio vs. maximum compression strain relationships.

The shape recovery progress upon heating in programmed S-PWs was studied. Figure 4.21 presents a typical result of S-PW30, which was programmed by means of compressing to 40% strain at 60°C (which is about above the melting finish temperature of PW as revealed in Fig. 4.2a), in terms of the shape recovery ratio against heating temperature. The shape recovery ratio was obtained by DMA (DMA Q800, TA) in force-control mode at a heating ramp of 0.5°C/min. Since a tiny constant force is applied, the recovery is about equivalent to free-recovery.

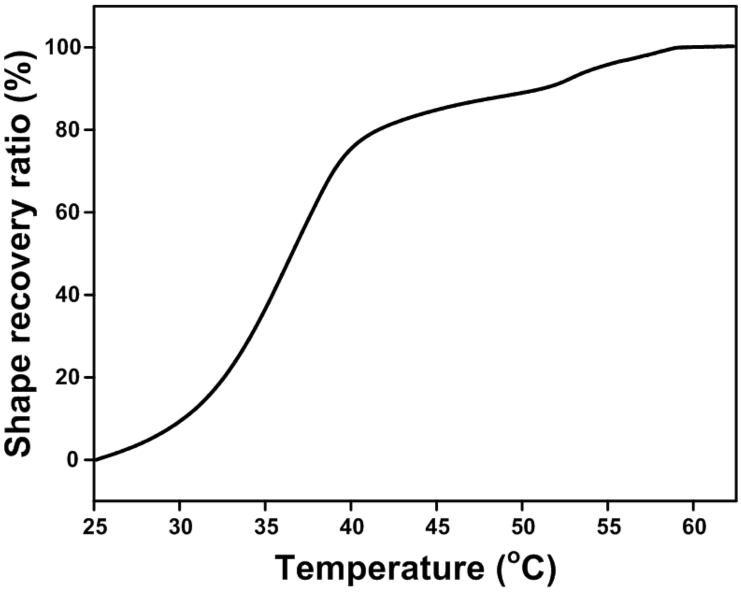

Figure 4.21 Typical shape recovery ratio vs. heating temperature relationship in S-PW30.

As we can see, shape recovery starts instantly when heating starts. This should be the result of thermal expansion, and gradually softening of PW upon heating which is consistent with the DMA result (refer to Fig. 4.5). Upon further heating, recovery becomes dramatic till temperature reaches around 40°C. This should correspond to the trough in the DSC result of PW (refer to Fig. 4.2a). After a seeming plateau, there is another big recovery event, but much less significant in terms of magnitude as compared with the first one, which should correspond to the second trough in DSC result. Full recovery achieves at around 60°C, which is the programming temperature.

4.5.2 Triple-shape memory effect

The triple-SME in SMPs normally requires two different switching/transition domains, which can be triggered for softening at different temperatures, or by different stimuli, such as heat or light. S-PW15-LMPW15 has two transition domains associated with two transitions at two different temperature ranges (refer to Fig. 4.4 for DSC result). After carefully selecting the programming procedure, the triple-SME can be realized in this hybrid.

Figure 4.22 reveals one typical experiment to demonstrate the triple-SME in S-PW15-LMPW15. The sample was programmed according to the following procedure (refer to the cooling curve of S-PW15-LMPW15 in Fig. 4.4).

1) A piece of straight sample (Shape A) is heated to 70°C and bent.
2) The curved shape (Shape B) is held while the temperature is reduced to 40°C.
3) The sample is straightened (Shape A’) at 40°C.
4) Cooling to 15°C, while holding Shape A’.

After programming, the sample was about straight as the original shape. Upon immersing into 65°C water, the sample bent downward (for the first 4.5 second in water) and then upward, and fully recovered its original shape after 18 seconds in water (Fig. 4.22).

Interestingly, between 4.5 second and 6 second, there is not any much shape change in the sample. This is due to that upon heating there is a big temperature gap (about 8^{o}C) between two troughs (refer to the heating curve of S-PW15-LMPW15 in Fig. 4.4). The first downward motion corresponds to the first trough, which ends at around 42^{o}C, while the subsequent upward motion is the result of the second trough, which finishes at about 65^{o}C.

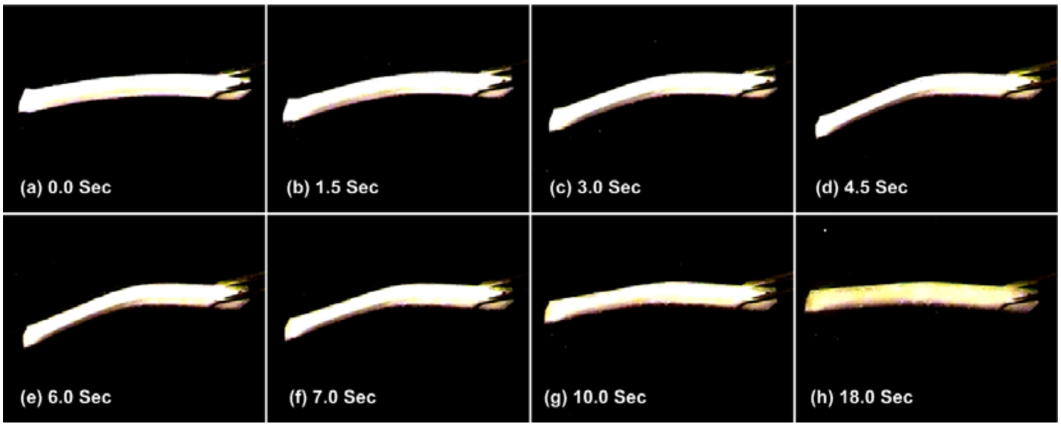

Figure 4.22 Triple-SME in S-PW15-LMPW15 upon immersing into 65^{o}C water.

Figure 4.23 presents another example demonstrating the triple-SME but by another means of motion during shape recovery. Again, we started with the same piece of straight sample (Shape A) (as used in Fig. 4.22). The programming procedure is as following.

- The sample is heated to 70^{o}C and then twisted.
- The twisted shape (Shape B) is maintained upon cooling to 40^{o}C.
- The sample is bent at 40^{o}C.
- After cooling to 15^{o}C and removing constraints, the new shape (Shape C) is a combination of twisting and bending as shown in Fig. 4.23(a_1).

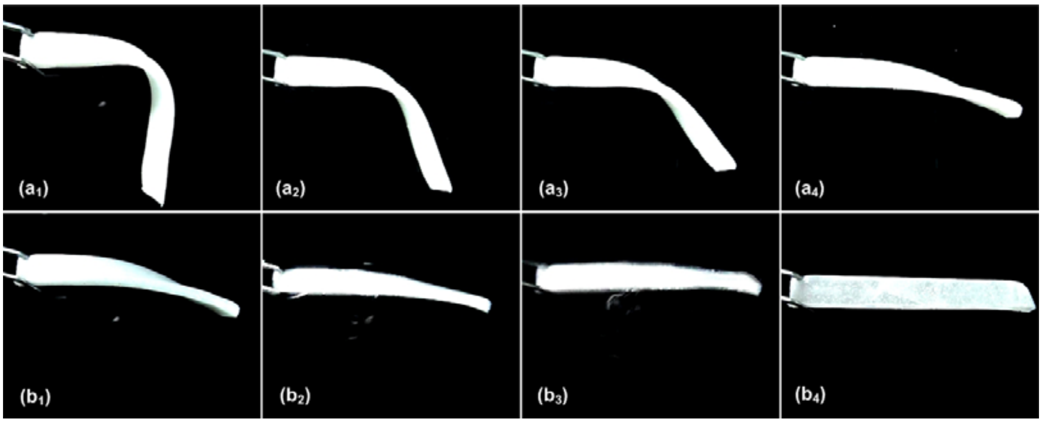

Figure 4.23 Triple-SME in S-PW15-LMPW15 upon heating. (a) from twisted-bent shape to twisted shape in 40°C water; (b) from twisted shape to original straight shape in 65°C water.

Different from the previous experiment, this time, shape recovery was carried out in two steps. In the first, the sample (Shape C) was placed into 40°C water. As revealed in Fig. 4.23(a_1) to (a_4), the sample became straight but was still twisted (which is Shape B). Subsequently, the sample was immersed into 65°C water. As we can see, the sample became straight (as Shape A, the original shape) (Fig. 4.23b_1 to b_4).

Similar to S-PW15-LMPW15, in which there are two troughs upon heating, S-PW has two troughs (refer to the DSC result of S-PW in Fig. 4.2a), although there is only one switching domain instead of two as in S-PW15-LMPW15. Following a similar programming procedure as for S-PW15-LMPW15 in Fig. 4.22, S-PW30 shows similar triple-SME (as presented in Fig.4.24) upon heating at two different temperatures, namely 45°C and 65°C.

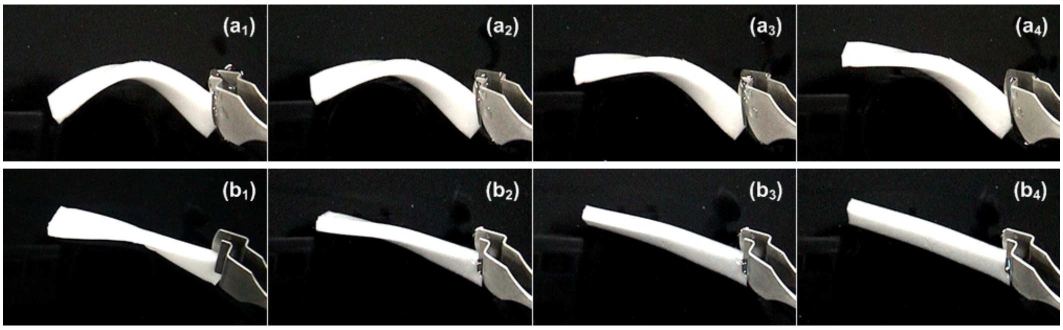

Figure 4.24 Triple-SME in S-PW30. (a) from twisted-bent shape to twisted shape in 45^{o}C water; (b) from twisted shape to original straight shape in 65^{o}C water.

It should be pointed out that silicone (PDMS) shows a glass transition at -127^{o}C and a melting of crystalline at -54^{o}C (the exact fraction of crystalline is highly dependant on the cooling rate applied on silicone), according to (Varma-Nair *et al.* 1989). As such, silicone can obtain a temporary shape if cooled to very low temperatures, e.g., -196^{o}C in liquid nitrogen, and the original shape can be recovered upon heating to room temperature. In other words, silicone itself, as an elastomer, is naturally a SMP despite that its transition temperature is so low that beyond the working temperature range of most engineering applications. However, theoretically speaking, we can use the SME in silicones to have at least one more intermediate shape in silicone based SMHs.

According to (Xie 2010) and (Sun and Huang 2010), in theory a number of intermediate shapes (i.e., multiple-SME) are possible even with only one switching/transition domain. We should bear in mind that the stability of these individual intermediate shapes, if there are too many, is a problem, in particular if the transition temperature range is narrow.

4.5.3 Mechanical two-way SME

Shape memory alloys (SMAs) are stiff at high temperatures and soft at low temperatures, so that SMAs with one-way SME are ideal for thermally induced cyclic actuation, biased against either an elastic element or another piece of SMA (Huang 2002). Such cyclic actuation is termed as mechanical two-way SME. In addition, after training, SMAs are able to switch between two shapes, one corresponding to high temperatures and the other to low temperatures (Huang and Toh 2000). Correspondingly, this is called material two-way SME.

On the contrary, normally SMPs are hard and tough at low temperatures but soft and flexible at high temperatures. Hence, generally speaking, SMPs are more suitable for one-time actuation only. From engineering application point of view, cyclic actuation is highly in demand. Thus, it is necessary to develop a systematic approach to realize two-way reversible actuation (i.e., mechanical two-way SME) in SMMs, other than SMAs.

In this section, we demonstrate how to achieve two-way reversible actuation (mechanical two-way SME) in silicone based SMHs.

- **Working mechanism**

Significant volume change is produced if a transition is between a loose amorphous phase and a closely packed/highly aligned phase in a material. As such, if a polymer has a higher degree of crystallinity, significant shrinkage/expansion can be observed during solidification/melting. Both PW and LMPW can expand over 10% upon heating from 20°C to 100°C due to a high fraction of crystalline in them, especially in PW (with a thermal volume expansion coefficient up to 16%) as shown in Fig. 4.25. This phenomenon can be utilized to achieve two-way reversible actuation in silicone based thermo-responsive SMHs.

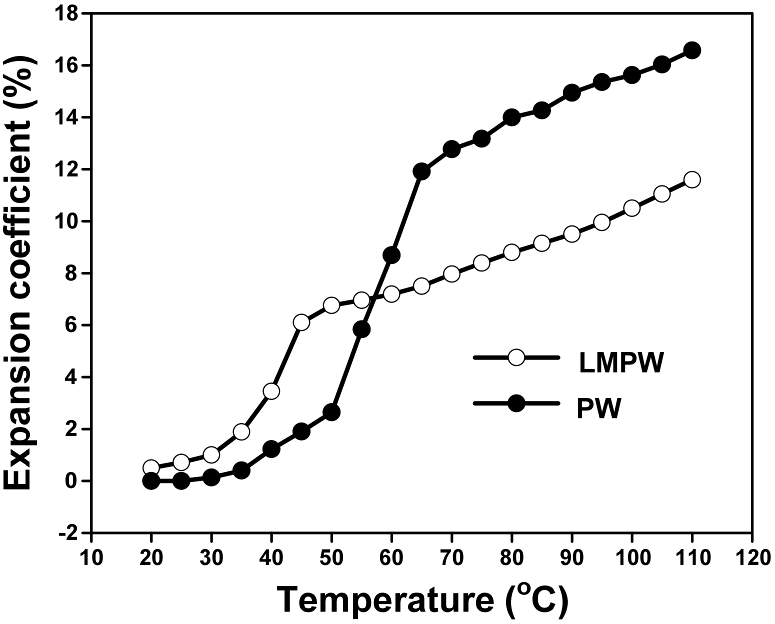

Figure 4.25 Thermal volume expansion coefficients of PW and LMPW upon heating.

The working mechanism of two-way reversible actuation in a silicone based SMH (filled with wax and glass fiber) is illustrated in Fig. 4.26. Glass fiber is added in to enhance the stiffness of silicone, but more importantly to limit the expansion of silicone during heating. The presence of stiff glass fiber in silicone limits the expansion of silicone, so that upon melting of wax a higher internal stress is produced to enhance the stiffness of hybrid (like blowing air into a plastic bag), instead of free expansion as a balloon made of rubber.

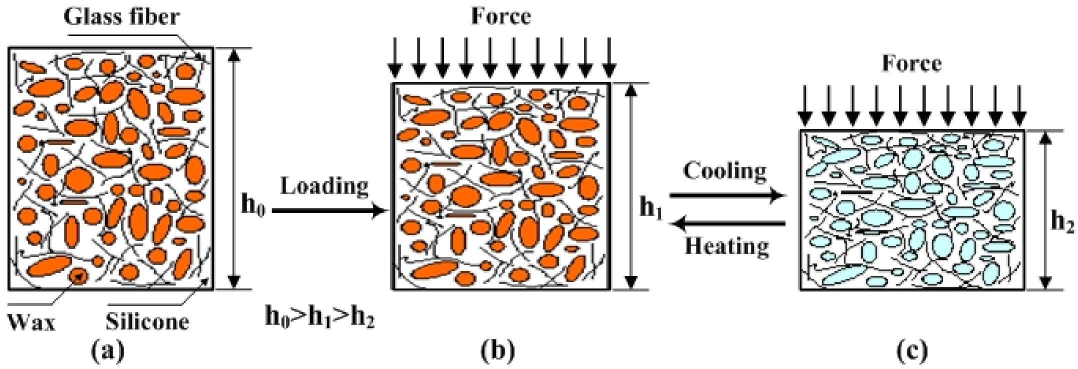

Figure 4.26 Working mechanism of two-way reversible actuation. (a) original shape at high temperatures; (b) after loading; (c) after cooling.

As illustrated in Fig. 4.26(a), after heating to above the melting temperature of wax, the sample has a height h_0. Subsequently, a compression force is applied so that the sample is shortened to h_1 (Fig. 4.26b). h_1 is further reduced to h_2 after cooling to below the consolidation temperature of wax (Fig. 4.26c). In the subsequent thermal cycling, the height of sample alters between h_1 (at high temperatures) and h_2 (at low temperatures). Two-way reversible actuation is obtained.

- **Demonstration**

Two-way reversible actuation is demonstrated in a piece of S-PW29-GF1 beam with a dimension of 40×10×2 mm. The experimental setup is presented in Fig. 4.27. PW was selected as the transition component due to its higher thermal expansion. A piece of elastic aluminum alloy beam was used to provide a bias force. Both the elastic beam and hybrid beam were fixed at one end and then pushed against each other at room temperature to generate significant bending in both of them. A metallic ruler was used as a reference to monitor the deflection at the tip of the free-end of the hybrid beam. Finally, the whole setup was placed inside a temperature controllable oven for thermal cycling.

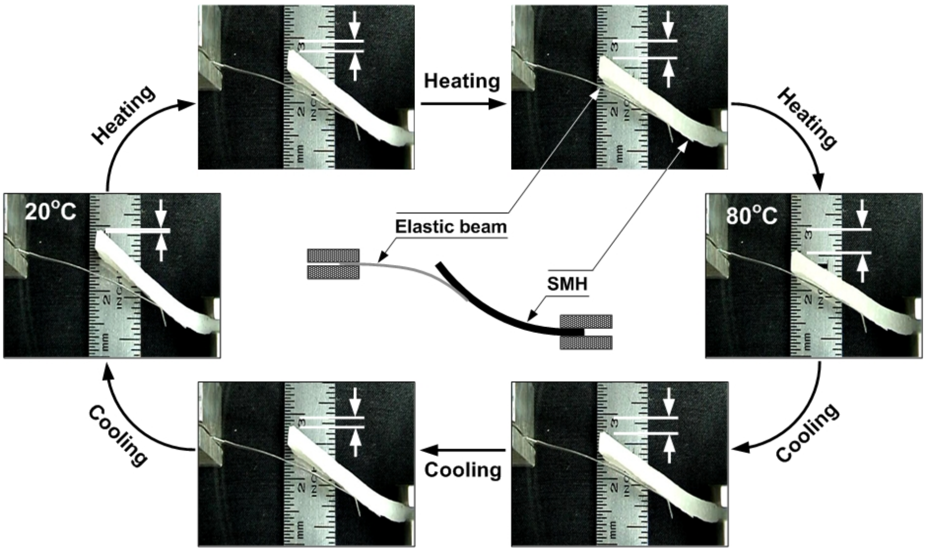

Figure 4.27 Two-way reversible actuation in S-PW29-GF1 upon thermal cycling.

As we can see in Fig. 4.27, upon heating to 80°C, the hybrid beam pushed the elastic beam down, which means that the hybrid beam became stiffer despite of melting of PW. On the other hand, upon cooling the hybrid beam moved upward. It suggests that the hybrid beam became soft and was pushed back by the elastic beam. The whole process is fully repeatable. Apparently, the observed up-down motion in the hybrid beam is not due to other reasons, but the volume expansion of PW.

As shown in Fig. 4.5, upon heating the storage modulus of S-PW29-GF1 decreases first due to melting of PW and then starts to increase gradually at above 65°C (due to thermal expansion of PW). A V-shape in the storage modulus vs. temperature curve is observed.

Unlike that in SMAs, the observed increase in storage modulus upon heating is not the sufficient condition to warrant the fitness of a SMP/SMH for two-way reversible actuation. This is because the storage modulus measured by DMA is derived from applying a tiny cyclic force (to ensure elastic deformation is fully in control), which is not equivalent to the real situation in two-way reversible actuation, in which the deformation is beyond the elastic range. In addition, DMA test is sensitive to many issues. For instance, different sample size and different clamp are able to slightly alter the result, which may not be serious for convention purposes, such as to determine the transition temperature, but is critical in study the two-way reversible actuation in a SMP/SMH. This is confirmed by the experimental results reported in the literature (Mather *et al.* 2008; Mather and Qin 2009; Zhang and Du 2010). Even the DMA result appears with a V-shape, there is no guaranty for two-way reversible actuation.

The change of stiffness in a S-PW hybrid upon thermal cycling can also be observed from the stress vs. strain relationships at different temperatures (refer to Figs. 4.8-4.10). Apparently, a higher stress at the same strain means a higher resistance to deformation, i.e., higher stiffness in the material. As we can see in Figs. 4.8-4.10, at 22^{o}C the stress value at a strain of 35% is the highest. It is the lowest at 60^{o}C, and turns to be higher at 100^{o}C. This trend is applicable to other strains in all three S-PW hybrid samples. Hence, the stiffness of S-PW hybrid follows a V-shape against heating temperature. This trend obtained from the stress vs. strain relationships at different temperatures is more relevant to the actual situation.

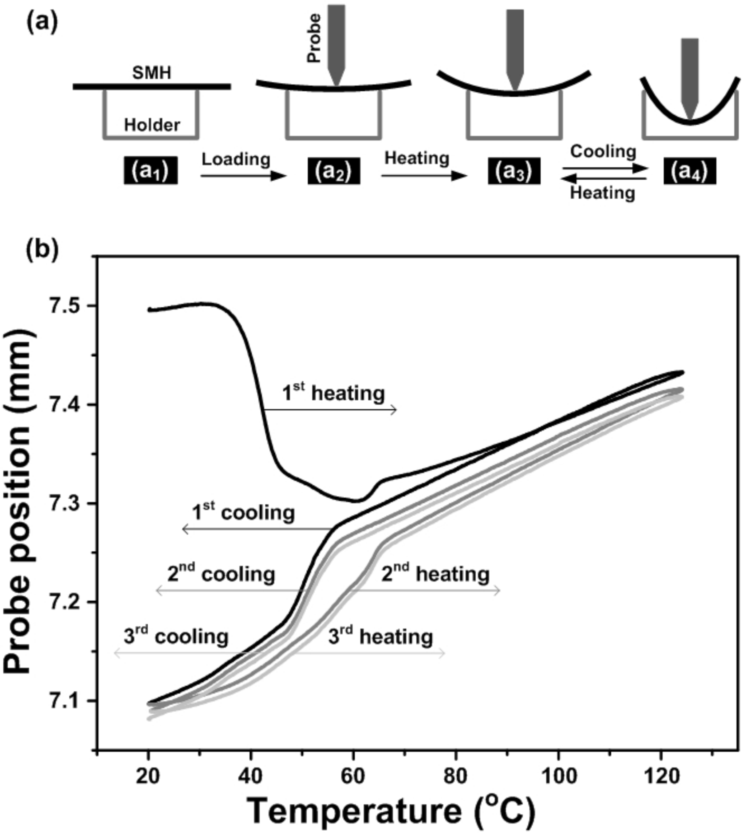

Figure 4.28 Two-way reversible actuation in S-PW29-CF1 in DMA test. (a) Illustration of experimental setup and procedure; (b) probe position vs. temperature relationship during thermal cycling.

A more straightforward investigation for the two-way reversible actuation was carried out on a PERKIN ELMER DMA 7e in three-point bending mode with a heating/cooling ramp of 2°C /min. The dynamic force function was turned off and replaced by applying a constant force of 200 mN. Refer to Fig. 4.28 (a) for the experimental setup and procedure. A piece of flat beam (S-PW29-CF1, 20×4×2 mm) was tested between 20°C and 120°C for a few thermal cycles. In the 1st heating process, we can see an apparent V-shape in the probe position vs. temperature curve (Fig. 4.28 b). In the subsequent thermal cycles, the curves change the pattern, so that upon heating the probe is at a high position (which indicates that the beam actually pushed the probe up), while upon cooling the probe is at a low position (i.e., the probe pushed the beam downward). Since a constant force was applied in the probe, we can conclude that the beam becomes stiffer upon heating and softer upon cooling. As compared with the thermal expansion vs. temperature curve of PW in Fig.4.25, the heating curves in the 2nd and 3rd heating processes in Fig. 4.28 (b) follow the same trend, which proves that thermal expansion of PW is the driving force behind the two-way reversible actuation.

We may further conclude that DMA can be used to examine the mechanical two-way SME in a SMP/SMH, when a non-conventional testing mode and procedure are applied.

4.6 Summary

A silicone based SMH system is developed, in which wax is used as the transition component. All types of shape memory phenomena, namely dual-SME, triple-SME, and mechanical two-way SME, are reproduced. The mechanisms behind these phenomena are investigated in details and verified by various experiments (including DSC, DMA and SEM etc). The dual-SME in S-PWs is systematically characterized, which is helpful to have a better understanding of the SME in SMHs and can serve as a generic guide in design and development of other types of SMHs.

Chapter 5 Multiple-responsive Silicone-Sodium Acetate Trihydrate Shape Memory Hybrids

Unlike that in shape memory polymers (SMPs), the components of shape memory hybrids (SMHs) are not limited to polymers. A wide range of materials can be utilized as components of a SMH, as long as certain conditions are satisfied, so that one can design a SMH to meet the requirements of a particular application. More importantly, multiple-stimuli-responsive SME may be easily achieved in SMHs. In this chapter, we investigate silicone-sodium acetate trihydrate hybrids. Sodium acetate trihydrate is a kind of salt with a number of interesting features, such as, super-cooling in the phase transition and exothermic during re-crystallization.

5.1 Materials and sample preparation

Same as in Chapter 4, silicone (SYLGARD® 184 Silicone Elastomer) was used as the elastic component (matrix) in this chapter. Sodium acetate trihydrate (Sodium Acetate, Trihydrate, Crystal 3462-01, Mallinchrodt Baker, Inc.), which is originally in a colorless crystal form, was used as the transition component (inclusion). At room temperature and within an ordinary environment, sodium acetate may be in two forms, namely, anhydrous or trihydrate. Sodium acetate trihydrate (SAT) has a molecular formula of $C_2H_3NaO_2 \cdot 3H_2O$, while sodium acetate anhydrous (SAA) has a molecular formula of

$C_2H_3NaO_2$. These two forms of sodium acetate may coexist. The main difference between SAT and SAA is that SAT has the super-cooling feature, i.e., upon cooling liquid (melting) SAT does not transform into solid at its melting temperature, but at a much lower temperature in order to have enough driving force to trigger homogeneous nucleation for re-crystallization. Wei and Ohsasa (2010) reported that the observed maximum degree of super-cooling in a SAT is 89°C. On the other hand, the nucleation and thus the solidification of super-cooled melting SAT can be triggered by some heterogeneous nucleation inducement methods, such as adding in nucleation catalysts (Guion and Teisseire 1991; Naumann and Emons 1989), applying a mechanical impact (Wei and Ohsasa 2010) or electrical voltage (Yoshii *et al.* 2002). A high thermal energy is released during solidification/re-crystallization of SAT. As such, SAT is often utilized in a latent heat energy storage system, in which a large amount of energy is saved in the form of transformation latent heat at ambient temperature for extended periods of time, which can be released later on (Agyenim *et al.* 2010; Zalba *et al.* 2003).

It should be pointed out that SAT and SAA have different melting temperatures, one is 58^oC (SAT) and the other is 324^oC (SAA). SAT is prone to lose its crystallization water and transforms into fine powder (SAA) upon exposure to air, a process known as efflorescence. As such, special attention is required during storage and fabrication. Furthermore, both SAT and SAA are water-soluble.

Figure 5.1 reveals typical differential scanning calorimeter (TA DSC Q200) results of SAT in three continuous thermal cycles at a heating/cooling rate of 5^oC/min. It can be seen that a high peak (heat absorption) occurs at approximately 62°C upon heating from room temperature (about 22°C) in the first thermal cycle. This high heat absorption is due to melting of SAT. After that, an aqueous solution (saturated) is formed. However, upon cooling, there is not any trough at all within the testing temperature range, which indicates that no re-crystallization occurs and SAT is still liquid. In the subsequently two more thermal cycles (2nd and 3rd cycles), virtually there is not any peak/trough at all within the testing temperature range. The measured latent heat of SAT upon melting (by integrating the area of melting peak in Fig. 5.1) is 270 J/g (very close to 264 J/g reported in Zalba et al. (2003)).

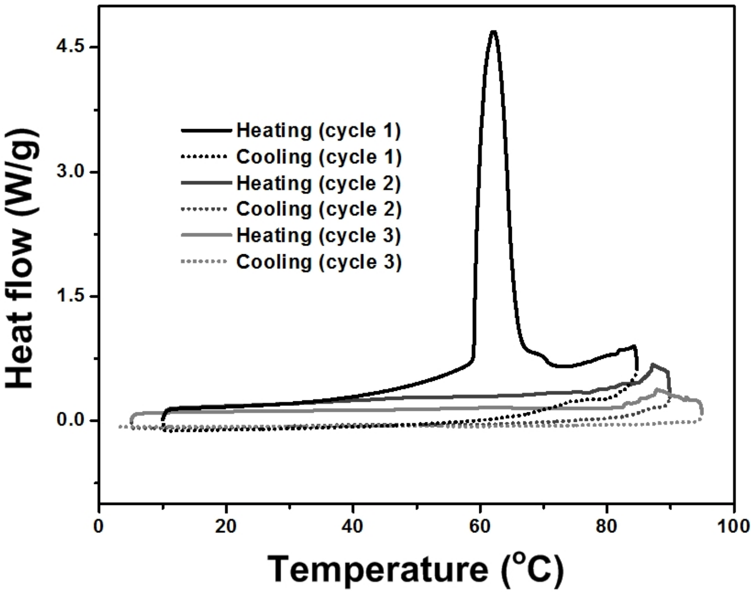

Figure 5.1 DSC result of SAT in three continuous thermal cycles.

According to the experimental result of thermogravimetric analysis (TGA) (AutoTGA 2950HR V6.0E, at heating rate of 10°C/min) shown in Fig. 5.2, the rate of weight loss in SAT upon heating to 200°C has two peaks at temperatures of 68°C and 121°C, respectively. At above around 140°C, all of crystallization water is lost by means of evaporation.

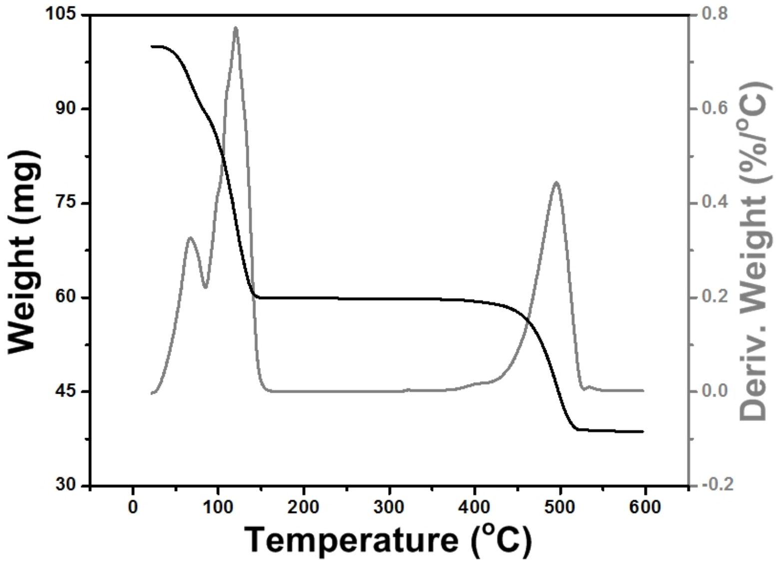

Figure 5.2 Typical TGA result of SAT upon heating at a heating rate of 10°C/min.

The major fabrication procedure of silicone (S)-SAT hybrids is essentially similar to that of silicone-wax hybrids discussed in Chapter 4. Firstly, fine SAT power (density: 1.45 g/cm^3), silicone base (density of cured silicone: 1.05 g/cm^3), silicone curing agent are weighted according to the required volume fraction. A high volume fraction of SAT (namely 50%, 60%, and 70%) in S-SAT samples is applied to ensure good connection among SAT aggregates within silicone matrix so that re-crystallization and/or dissolving of SAT (if applicable) can propagate throughout the whole sample. To prevent/minimize high density SAT powder from sinking to the bottom of S-SAT mixture during sample preparation (in particular before curing starts), silicone should be slightly pre-cured to increase its viscosity before mixing with SAT powder. In the next step, the mixture of silicone and SAT is poured into a mold and then transferred into a vacuum chamber to remove bubbles that are trapped within the mixture during stirring. A piece of sample is obtained for further testing after curing at room temperature for more than 24 hours (about 22°C).

Typical dispersion of SAT within silicone matrix is shown in Fig. 5.3. The particular sample is S-SAT50. Note that S-SAT*x* indicates the volume fraction of SAT in this S-SAT hybrid is *x*. As we can see, SAT inclines to form aggregates, which are not fully isolated from each other but connected by some tiny SAT powders.

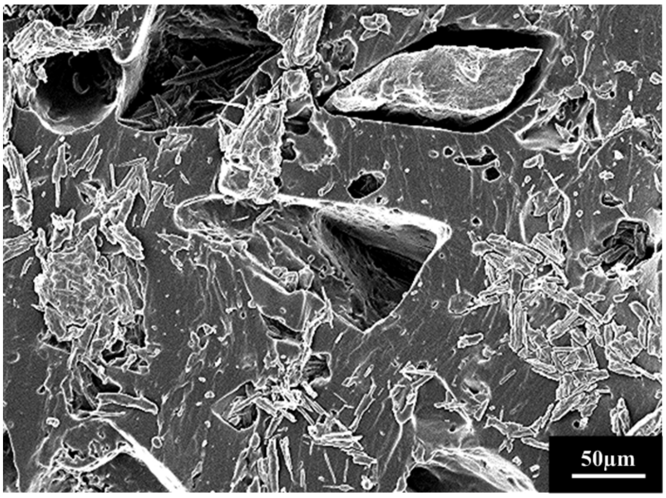

Figure 5.3 Typical scanning electron microscope (SEM) image of S-SAT50 hybrid.

It should be pointed that in order to avoid efflorescence in SAT during fabrication, humidity of environment during fabrication should be controlled. Furthermore, depending on the exact application, additional coating of a thin layer of, for instance, silicone may be applied to prevent efflorescence of SAT in S-SAT hybrids in long term application and/or cyclic actuation.

5.2 Mechanically induced shape fixation in S-SAT hybrids

As discussed in Section 5.1, super-cooling is required for re-crystallization of SAT. However, as shown in Fig. 5.4, a piece of pre-heated S-SAT70 turned to be white everywhere after being tapped once at a single point. The hybrid was pre-heated to 80°C to ensure fully melting of SAT, so that the as-fabricated white sample became translucent and softer. Even after being cooled back to room temperature, due to the requirement of super-cooling, the embedded SAT was still in liquid form. Crystallization of SAT was triggered by tapping once within a small area of the sample. Within 12 seconds, the whole sample became white and harder. Apparently, tapping a piece of super-cooled S-SAT hybrid triggers the nucleation of embedded SAT within the compressed area, and thus re-crystallization starts from there locally and subsequently propagates quickly throughout the whole sample as the SAT aggregates are connected by tiny SAT channels. Obviously, high volume fraction of SAT is the condition for such mechanically induced hardening of S-SAT hybrids.

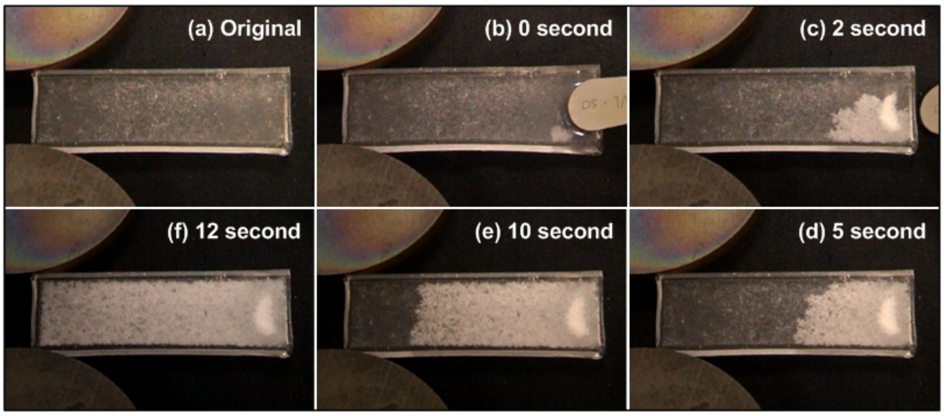

Figure 5.4 Snapshots of re-crystallization and propagation sequence in a piece of S-SAT70 (40×12×2 mm in dimensions) by tapping once.

This hardening feature can be utilized for programming, instead of following the traditional programming approaches in conventional thermo-responsive SMHs/SMPs, as demonstrated in Fig. 5.5. Similar to that in Fig. 5.4, the same sample (S-SAT70) was pre-heated to 80^{o}C to ensure fully melting of SAT and then cooled in air to room temperature. The sample was soft and bent gently (to prevent mechanically induced hardening). Two pieces of metal blocks were used to maintain the sample in bending shape. To trigger mechanically induced shape fixation, one metal block was quickly pushed a little bit to further bend the sample. Figure 5.5 (b_1) to (b_4) shows the re-crystallization of SAT and propagation throughout the whole piece of sample. After that, two metal blocks were removed. Apart from a little bit of elastic recovery, the bent shape is largely maintained (refer to Fig. 5.5c).

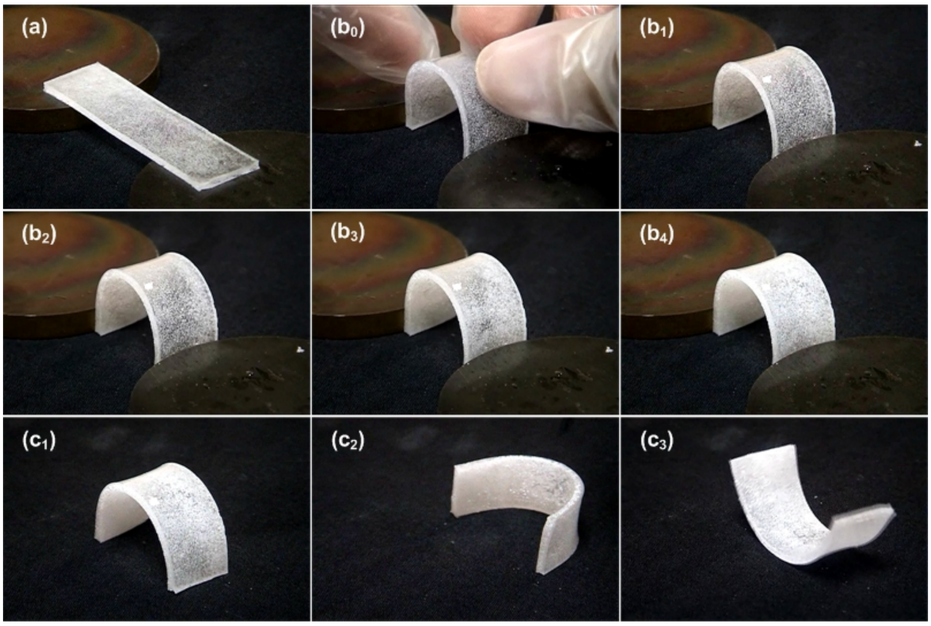

Figure 5.5 Snapshots of programming S-SAT70 by bending at room temperature.

5.3 Multiple-stimuli-responsive shape memory effect

5.3.1 Thermo-responsive shape memory effect

A piece of original flat S-SAT60 sample (45×7×2 mm in dimensions) was programmed into bent shape following the mechanical programming procedure discussed in Section 5.2. Subsequently, the bent sample was immersed into 75^{o}C water for thermally induced shape recovery (i.e., thermo-responsive shape memory effect, SME). As shown in Fig. 5.6, the S-SAT60 sample fully recovered its original shape in 15 seconds. Melting of SAT crystalline upon heating effectively releases its constraint on the pre-deformed elastic silicone matrix, so that the elastic silicone returns its original shape to fully release the stored elastic energy. Consequently, S-SAT60 recovers its original straight shape.

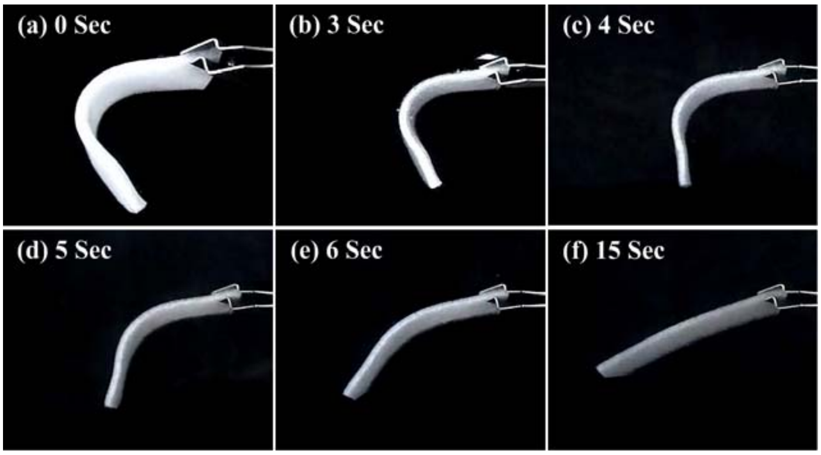

Figure 5.6 Snapshots of shape recovery sequence in a S-SAT60 upon immersing into 75^{o}C water.

It should be pointed out that the temporary shape of S-SAT can also be programmed by cooling to just right below the melting temperature of SAT (as in conventional thermo-responsive SMHs/SMPs) if a small amount of SAA is included in SAT. This part of SAA can effectively initiate the nucleation of SAT to prevent super-cooling.

5.3.2 Water-responsive shape memory effect

Water soluble is another intrinsic feature of SAT, which can be utilized to achieve the water-responsive SME atop the thermo-responsive SME discussed in Section 5.3.1. The fundamental mechanism behind the water-responsive SME is similar to that of thermo-responsive SME in dual-component SMHs/SMPs. After programming, re-crystallized SAT (transition inclusions), which is hard, effectively prevents the elastic recovery of silicone (elastic matrix). As such, the temporary shape is largely maintained. However, instead of heating to melt SAT, dissolving SAT in water is an alternative approach to remove the constraint of SAT on the deformed silicone to induce the so called water-responsive SME.

Two pieces of S-SAT50 (40×8×2 mm in dimensions) were prepared following the same fabrication procedure as discussed in Section 5.1. However, in both pieces, silicone was not pre-cured, so that high density SAT was allowed to settle down at the bottom of sample. After being programmed into the same bent-shape (the left side surface of both samples was with high percentage of SAT), one piece of S-SAT was vertically immersed into room temperature water (Fig. 5.7a_0), while the other was vertically hung in air (Fig. 5.7b_0) (humidity: 54%). There was not much shape change in the sample hung in air even after 23 hours (Fig. 5.7b), while we can see full shape recovery in the sample after being immersed in water for 12 hours (Fig. 5.7a).

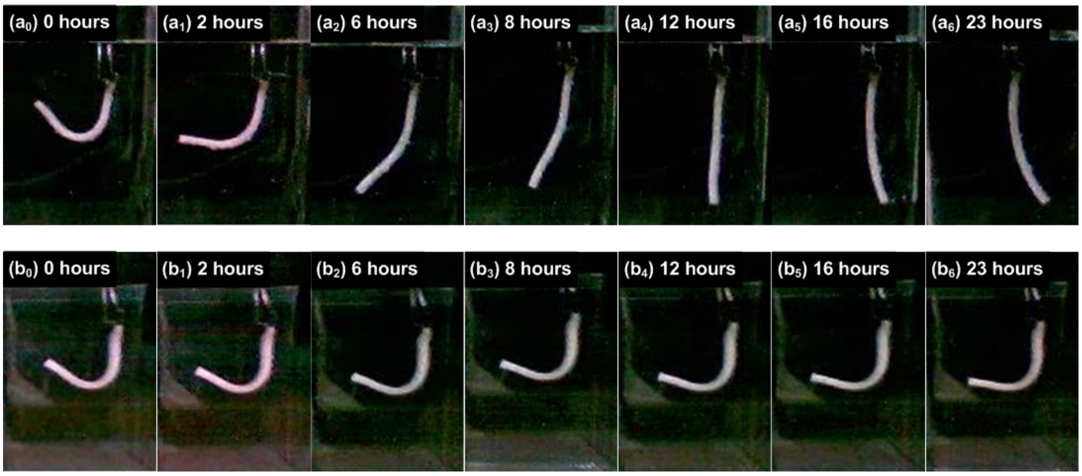

Figure 5.7 Snapshots of shape change sequence in pre-bent S-SAT50 upon (a) immersing into room temperature water and (b) in air.

There are three major possible reasons behind small shape change in Fig. 5.7 (b). One is creeping due to gravity, and the second is the moisture effect from high humidity air, which softens SAT slightly, in particular inside the layer with high SAT concentration. Volume expansion of SAT after absorption of moisture from surround air might be an additional reason atop the above mentioned two.

We also observed further bending into the opposite direction after 12 hours of immersion in room temperature water. Water mainly penetrates into the left side of sample, where a high concentration of SAT is located. Dissolving starts from this side of the sample, while the right side is about fully occupied by silicone so that the right side serves more likely as an elastic spring. It is easy for SAT within the sample surface to be fully dissolved and washed away almost instantly. However, after penetrating into deep inside of the material, high concentration SAT solution is formed but cannot be easily *washed* away. As such, the transition from SAT crystal into high concentration SAT solution can naturally cause slight volume expansion, which induces local expansion at the water penetration line and consequently opposite bending as we have observed after 12 hours of immersion in water.

Water-responsive feature of S-SAT hybrids can be applied for water-responsive actuation in SMH devices. A ring-shaped S-SAT50 sample was prepared (Fig 5.8 a_0) and then programmed into a Y-shape (Fig 5.8 a_1). The original ring shape was fully recovered after 50 hours of immersion in room temperature water (Fig 5.8a_2 to a_9).

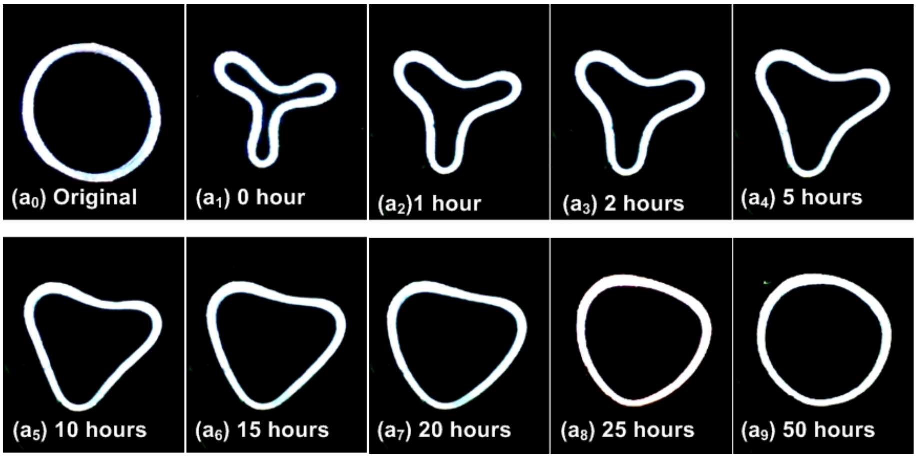

Figure 5.8 Snapshots of shape recovery sequence in a piece of S-SAT50 ring (2 mm in thickness and 40 mm in diameter) upon immersion into 22°C water.

Figure 5.9 demonstrates the feasibility of retractable ring like S-SAT stent based on the water-responsive SME. The stent (ring) was fabricated into an original star-shape (Fig.

5.9a_0, refer to Figs A1 to A2 in Appendix for the dimensions of mold), and then programmed into a flower shape with a larger size (Fig. 5.9a_1). After programming, the ring was still highly elastic and could be elastically deformed to fit into, for example a catheter, for elastic deployment inside blood vessel. Full shape recovery occurred after 300-minute immersion in 22^{o}C water (Fig. 5.9a_2 to a_5). The exact time required for shape recovery can be controlled by the exact dimension of stent, volume fraction and dispersion of SAT, and water temperature etc.

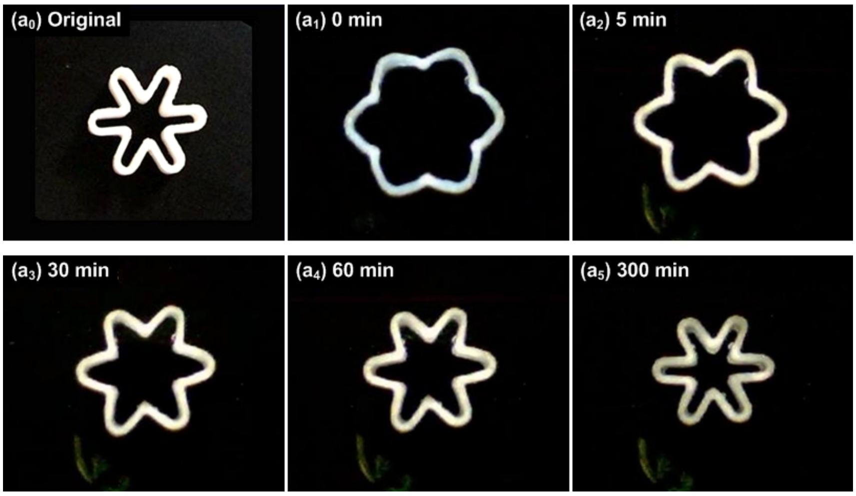

Figure 5.9 Snapshots of shape recovery sequence in a stent/ring made of S-SAT70 upon immersing into 22^{o}C water.

In real retractable stents, SAT may be replaced by drugs in crystal form, so that the stents become a drug elute stent, i.e., able to gradually release drug to prevent infection and/or in-growth of tissues. Such retractable stents might be useful in urethral cancer or prostate cancer treatment, in which a removable stent, instead of a permanent one, is often preferred.

5.3.3 Pressure-responsive shape memory effect

As discussed above, super-cooled SAT is able to maintain its liquid state at below its melting temperature unless an external stimulus, e.g., pressure, is applied to trigger re-crystallization, which can self-propagate throughout the material quickly accompanied by releasing a great amount of heat (latent heat of SAT is 270 J/g, Fig. 5.1).

We may utilize these features (namely pressure-responsive, heat generation and self-propagation) to trigger thermally induced shape recovery in a thermo-responsive SMH/SMP in which enough amount of SAT is embedded inside. Fundamentally, this is still a heating process, similar to that in traditional electro-responsive and magneto-responsive SMPs (Buckley *et al.* 2006; Leng *et al.* 2008b; Mohr *et al.* 2006). However, from the triggering mechanism point of view, this material is able to be activated by compression, i.e. the directly applied stimulus is in the form of pressure, which indicates that this is a new type of shape memory material (SMM), i.e., pressure-responsive SMM.

To experimentally verify the pressure-responsive mechanism, which has never been reported in the literature, a piece of S-PW SMH loaded with SAT was prepared. The volume ratio of silicone: PW: SAT is 55:30:15. Fabrication of S-PW-SAT follows standard procedure as discussed above.

A piece of straight S-PW-SAT strip (55×10×2.5 mm in dimensions) was pre-heated to 80^{o}C and then bent by about 90^{o} before cooling back to room temperature. The bent shape was largely maintained after constraint was removed (Fig. 5.10a_0). Here, room temperature PW, which is hard, functions to keep the deformed shape, while SAT is still able to maintain in liquid state. A piece of metal block was gently placed atop one end of the sample to hold the deformed sample in position. After pressing quickly at a point close to its fixed end using a metal stick (Fig. 5.10a$_1$), pressure induced re-crystallization of SAT was triggered and heat was released (refer to infrared images in Fig. 5.10b). Consequently, shape recovery was activated due to thermally induced softening of PW. Fig. 5.10(a$_2$) to (a$_5$) reveals the shape recovery sequence, while Fig. 10 (b) presents the corresponding temperature distribution within the sample.

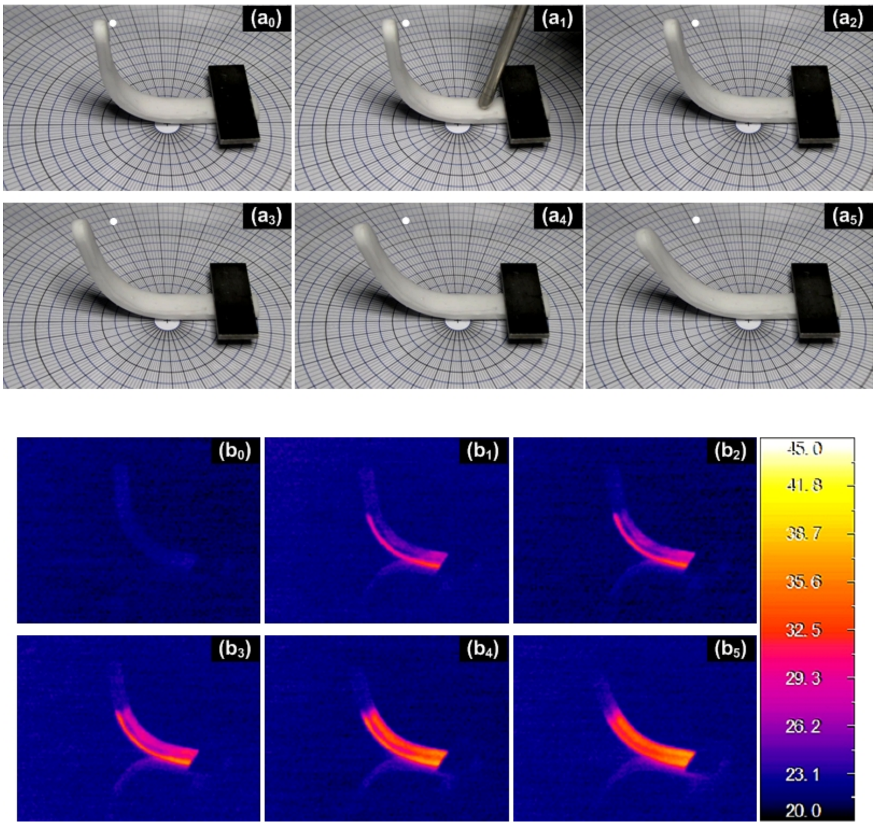

Figure 5.10 Optical (a) and infrared (b) snapshots of shape recovery sequence in a piece of S-PW-SAT triggered by pressuring once at a local position of the sample (a$_1$).

We can clearly see the propagation of high temperature zone within the sample, which indicates the crystallization front and matches well with the sequence of shape recovery recorded by the optical camera.

Here, silicone serves as the elastic component, PW is the transition component, and SAT functions as heating source. As such, the shape fixity ratio of this material depends mainly on silicone and PW, while the shape recovery ratio also depends on SAT. The total amount of latent heat and heat capacity of SAT, PW and silicone largely determine the highest heating temperature in the material that can be possibly reached, while the surrounding environment (i.e., heat convention, conduction and radiation, and environmental temperature, etc) determines heat transfer in the heating process. From design point of view, we need to ensure the amount of SAT in the material is able to generate enough heat to melt PW.

As such, the transition temperature and transition temperature range are factors to be considered in SMH design. A first order estimation of the required amount of SAT can be worked out as following.

The total thermal energy (Q_0) used for heating is from the latent heat of re-crystallization of SAT, i.e.

$$Q_0 = M_{SAT} \cdot H_L^{SAT} \tag{5.1}$$

where, H_L^{SAT} is latent heat in re-crystallization of SAT, and M_{SAT} is the mass of SAT.

The total absorbed thermal energy includes three parts, namely Q_1, Q_2 and Q_3 ,

$$Q_1 = C_{SAT} \cdot M_{SAT} \cdot (T_2 - T_0) \tag{5.2}$$

$$Q_2 = C_{silicone} \cdot M_{silicone} \cdot (T_2 - T_0) \tag{5.3}$$

$$Q_3 = H_L^{PW} \cdot M_{PW} + C_{PW} \cdot M_{PW} \cdot (T_1 - T_0) \tag{5.4}$$

where, Q_1 is the thermal energy for heating re-crystallized SAT, Q_2 and Q_3 are the thermal energy absorbed by silicone and PW, respectively, T_0 is the surrounding/room temperature, T_1 and T_2 are the start and finish melting temperatures of PW, respectively, H_L^{PW} is the latent heat to melt PW, $C_{silicone}$, C_{PW} and C_{SAT}, are the heat capacities of silicone, PW and SAT, respectively, $M_{silicone}$ and M_{PW} are the mass of silicone and PW, respectively.

If heat transfer between the sample and its surrounding is omitted, we have,

$$Q_0 = Q_1 + Q_2 + Q_3 \tag{5.5}$$

Let us assume that,

$$M_{silicone} = a \cdot M_{PW} \tag{5.6}$$

Combining Eqns. 5.1 to 5.6 together, we can get that,

$$\frac{M_{SAT}}{M_{PW}} = \frac{a \cdot C_{silicone} \cdot (T_2 - T_0) + H_L^{PW} + C_{PW} \cdot (T_1 - T_0)}{H_L^{SAT} - C_{SAT} \cdot (T_2 - T_0)} \tag{5.7}$$

If we consider one unit of sample, the volume fraction of silicone ($V_{silicone}$), PW (V_{PW}) and SAT (V_{SAT}) can be expressed as,

$$V_{silicone} = 1 - V_{pw} - V_{SAT} \tag{5.8}$$

$$V_{PW} = \frac{1}{\frac{a \cdot C_{silicone} \cdot (T_2 - T_0) + \Delta_L H_{PW} + C_{PW} \cdot (T_1 - T_0)}{\Delta_L H_{SAT} - C_{SAT} \cdot (T_2 - T_0)} \cdot \frac{\rho_{PW}}{\rho_{SAT}} + \frac{a \cdot \rho_{PW}}{\rho_{silicone}} + 1} \tag{5.9}$$

$$V_{SAT} = \frac{1}{\rho_{SAT} \cdot (\frac{a}{\rho_{silicone}} + \frac{1}{\rho_{PW}}) \cdot \frac{H_L^{SAT} - C_{SAT} \cdot (T_2 - T_0)}{a \cdot C_{silicone} \cdot (T_2 - T_0) + H_L^{PW} + C_{PW} \cdot (T_1 - T_0)} + 1} \tag{5.10}$$

where $\rho_{silicone}$, ρ_{PW} and ρ_{SAT} are the density of silicone, PW and SAT, respectively.

To obtain a high shape fixity ratio in S-PW-SAT hybrid, a is set to be 2.17 (i.e., the volume ratio of PW and silicone is 35/65, which is selected according to the study in Section 4.5.1). We assume that latent heat in solidification of SAT is the same as that of melting, i.e., H_L^{SAT} is 270 J/g (refer to Section 5.1). Similarly, we have obtained H_L^{PW} as 185 J/g (which is very close to the reported value of 189 J/g in (Abhat 1983)). The calculation is based on the experimental result reported in Fig. 4.2. $\rho_{silicone}$, ρ_{PW} and ρ_{SAT} are 1.05 g/cm^3, 0.9 g/cm^3, and 1.45 g/cm^3, respectively. $C_{silicone}$, C_{PW} and C_{SAT} are 1.4 J/(g·K), 2.5 J/(g·K) and 1.7 J/(g·K), respectively. T_0, T_1, and T_2 are 24^{o}C, 30^{o}C and 58^{o}C, respectively.

Substituting above values into Eqns. 5.8-5.10, we obtain the volume ratio of silicone:PW:SAT as 49%:27%:24%, i.e. at least 24% is required.

The detailed underlying mechanism behind this pressure-responsive feature is actually far more complicate. Figure 5.5 reveals that re-crystallization of SAT involves two simultaneous phenomena, one is releasing of latent heat, and the other is solidification of SAT. The former softens PW so that plays a positive role for shape recovery, while the latter actually prevents shape recovery. At the early stage of re-crystallization, SAT is still relatively soft (since the resulted SAT crystals are still small and largely separated from each other without forming a strong network), and thus shape recovery is still relatively easy to progress forward. Only after a strong network of SAT crystals is formed, which is able to fully support the elastic force from the elastic silicone matrix, further recovery of S-PW-SAT is stopped.

In addition to pressure, re-crystallization of SAT can be triggered by some other ways. Electrical voltage and ultrasonic irradiation are two among others (Wei and Ohsasa 2010; Yoshii *et al.* 2002). Consequently, electro-responsive and ultrasonic-responsive SMHs can be developed based on these actuation methods.

5.4 Mechanical two-way shape memory effect

Similar to S-PW-GF discussed in Section 4.5.3, mechanical two-way SME can be achieved in S-SAT, but based on a different type of transition. Refer to Fig. 5.2. Upon heating to around 100^{o}C, crystalline water derived from SAT starts to turn into gas, which naturally induces significant volume expansion. This phenomenon can be utilized for two-way reversible actuation (i.e., mechanical two-way SME) in S-SAT hybrids.

As shown in Fig. 5.11, a piece of S-SAT70 (40×10×3 mm in dimensions) moved up against a piece of elastic beam upon heating from 24^{o}C to 140^{o}C. Apparently, the pre-bent S-SAT beam becomes stiffness, which is largely due to the internal pressure generated during water to gas transition upon heating. It should be pointed out that in order to avoid leakage of gas (developed from water upon heating) the S-SAT beam was coated with a thin layer of silicone. We also limited the maximum heating temperature to 140°C to prevent overpressure. In the subsequent cooling process, gas condensed back to water and thus, the internal pressure was reduced, so was the stiffness of the S-SAT beam. Consequently, the S-SAT beam moved downwards. This whole process is fully repeatable upon thermal cycling.

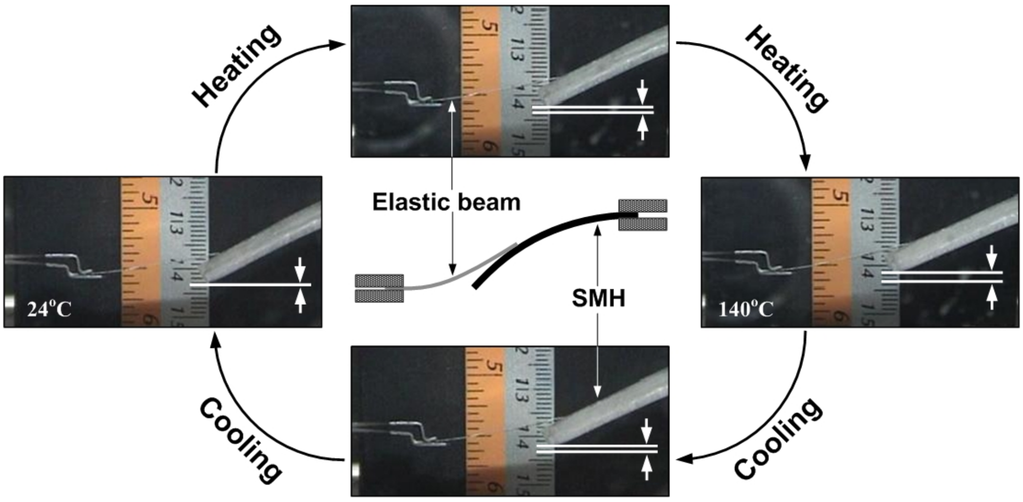

Figure 5.11 Two-way reversible actuation in a piece of S-SAT hybrid against an elastic beam upon thermal cycling.

As mentioned in Section 4.5.3, the two-way reversible actuation reported here can be further enhanced by filling micro fibers, such as glass fiber or carbon fiber, into the silicone matrix to prevent isotropic elastic expansion.

5.5 Summary

Multiple-stimuli-responsive SME is demonstrated in this S-SAT hybrid system. As revealed, shape recovery can be triggered by not only heat (thermo-responsive) and water (water-responsive), but also pressure (pressure-responsive). In addition, we show that shape fixation of S-SAT hybrids can also be achieved by means of tapping instead of following conventional thermo-mechanical programming approaches for traditional thermo-responsive SMPs/SMHs. Two-way reversible actuation is also realized in this hybrid system.

Chapter 6 Silicone-Melting Glue Shape Memory Hybrids with Rubber-like and Self-healing Features

To my best knowledge, at least till now, shape memory polymers (SMPs) are rubber-like only at high temperatures (above their transition temperature), while at low temperatures they are either brittle or ductile (i.e., easily to break or to be quasi-plastically deformed) (Dietsch and Tong 2007; Huang *et al.* 2011). On the other hand, we have seen significant efforts towards achieving self-healing in materials (Wool 2008; Yuan *et al.* 2008). As shown in the movie series, Terminator, future robotic solders require not only repeated and instant self-healing function, but also shape and strength recovery. Till today, such requirements have yet been simultaneously achieved in any material. By careful selection of components of a hybrid, we may achieve some novel features besides the shape memory effect. In this chapter, we present a SMH, namely silicone-melting glue (S-MG) hybrid, which not only has the shape memory effect (SME), but also is able to achieve self-healing, not only shape recovery, but also strength recovery in an instant and repeated manner. In addition, it is rubber-like from above to below its transition temperature.

6.1 Materials and sample preparation

Same as in the silicone-wax hybrid system and silicone-sodium acetate trihydrate hybrid system discussed in Chapters 4 and 5, SYLGARD® 184 silicone (S) was used as the elastic component. Melting glue (MG) was Sellery glue stick (5/16"×4" 96-802) from Centenary Materials Co., Ltd., Taiwan (under authorization of Sellery Inc. California U.S.A.). The average density of MG over ten measurements is 1.004 g/cm^{-3}. Ethylene vinyl acetate (EVA) is the main component of this MG.

The general fabrication procedure of S-MG hybrids is similar to that of silicone-wax/silicone-SAT shape memory hybrids (SMHs). A brief summary of the main fabrication procedure is presented as follows.

- As received MG sticks are cut into small pieces.
- Mix a certain amount of MG with liquid silicone base component according to the required fraction of a particular S-MG sample.
- Heat the mixture to 100°C in an oven (which is well above the melting finish temperature of this MG).
- Stir the mixture quickly and continuously at above 83°C (which is the melting finish temperature of this MG) until the mixture becomes fully transparent without any visible small particles at all.
- Keep stirring during the mixture is cooled down to room temperature (about 22°C).
- Add in the required amount of curing agent and stir again for a uniform dispersion.
- Well mixed mixture is poured into a mould with the required shape and dimensions.
- Place the mould in a vacuum chamber to remove all trapped air bubbles in the mixture.

- After being left in air at room temperature for 24 hours, a fully cured solid sample is obtained.

Following this procedure, S-MG samples in different shapes and with different MG volume fractions were fabricated. Figure 6.1 shows typical S-MG dog-bone shaped samples with different MG contents. Refer to Figs. A3 and A4 in Appendix for the dimensions of moulds to fabricate dog-bone shaped samples. Note that same as the definition in previous chapters, here S-MGx means that the volume fraction of MG in a S-MG hybrid is x.

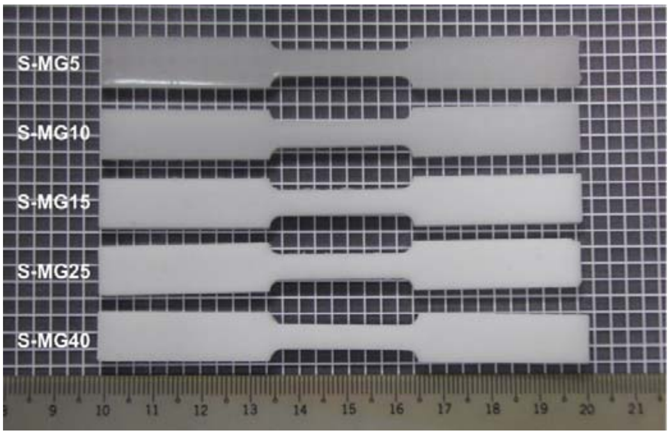

Figure 6.1 Typical dog-bone shaped S-MG samples with different volume fractions of MG.

A differential scanning calorimeter (DSC, TA DSC Q200) was used to characterize the thermal properties of S-MG samples. Samples with an approximate weight of 10 mg were tested at a heating/cooling ramp of 8^{o}C min^{-1} within a temperature range of 20^{o}C to 120^{o}C. The observed trough and peak in heating process and cooling process in Fig. 6.2 correspond to the melting and solidification transition, respectively. In all samples with

MG (including pure MG), melting/solidification start/finish temperatures are about the same, and there is not any new peak/trough at all. The melting start and finish temperatures of all S-MG samples are about the same as that of MG, i.e., about 58°C and 83°C, respectively.

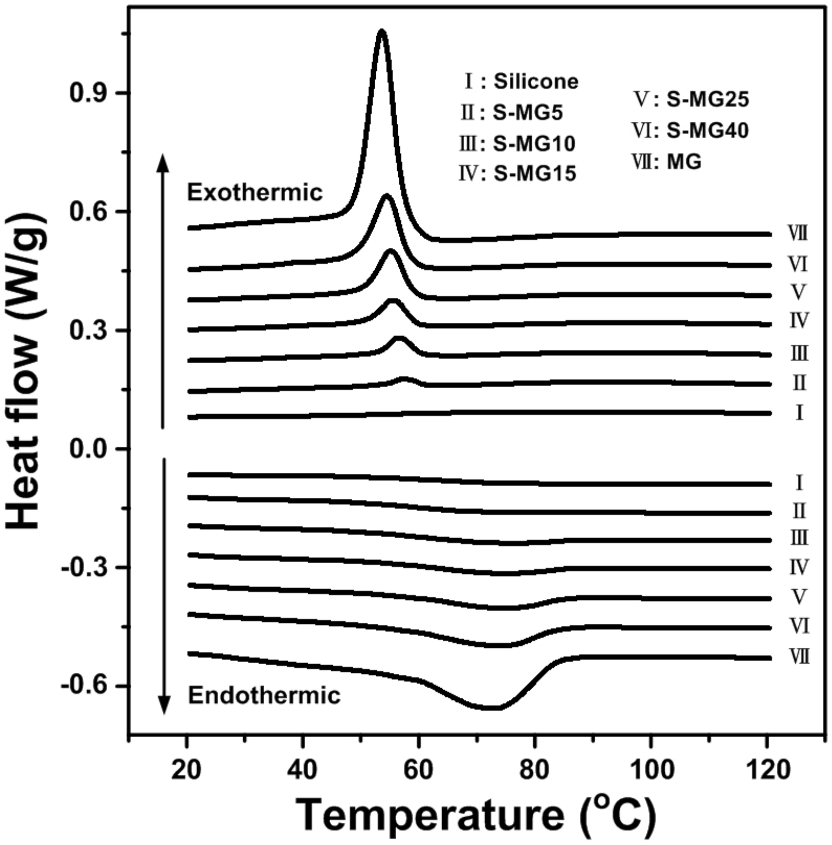

Figure 6.2 DSC results of S-MG upon heating (endothermic) and cooling (exothermic).

Based on the DSC results in a thermal cycle, latent heat of all samples was calculated and plotted against the MG content in Fig. 6.3. An approximate linear relationship between the latent heat and MG content is observed. According to Fig. 6.2 and Fig. 6.3, it seems that the chemical reaction between silicone and MG, if any, is very much limited.

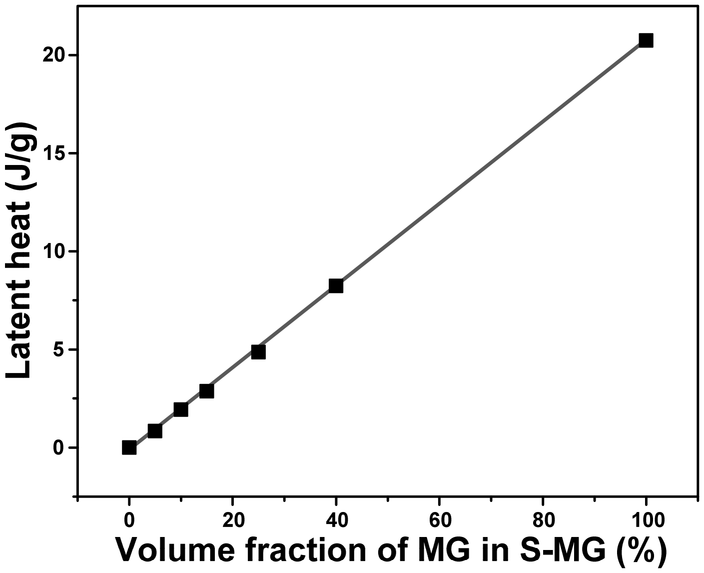

Figure 6.3 Latent heat against MG content in S-MG samples.

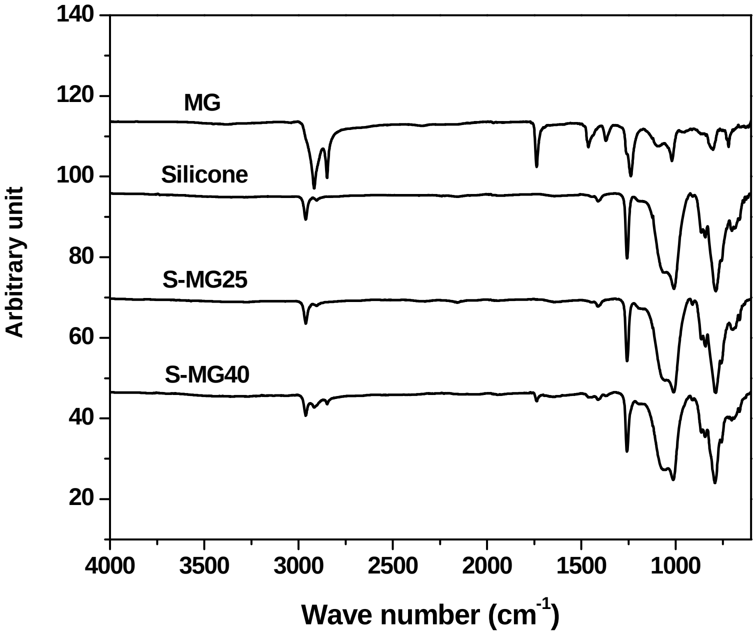

Figure 6.4 FTIR spectra of MG, silicone, S-MG25 and S-MG40 at room temperature.

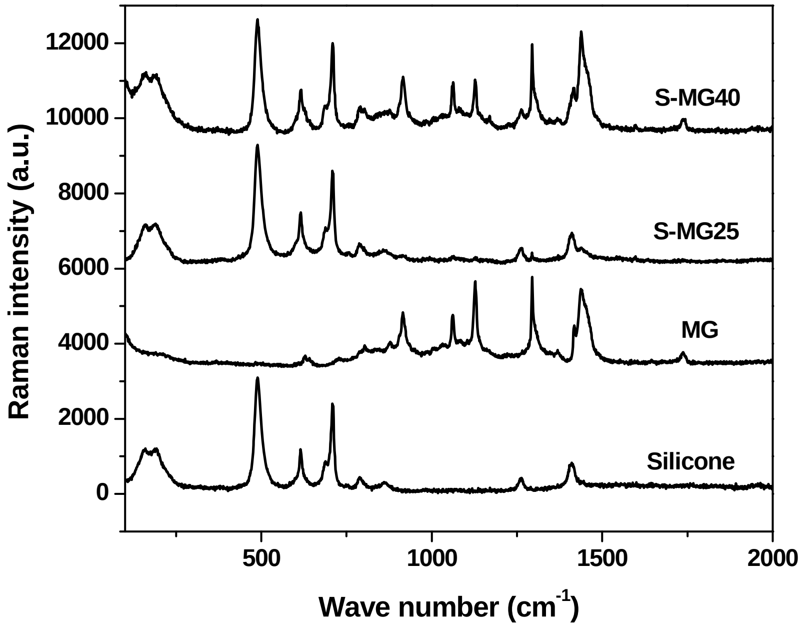

Figure 6.5 Raman spectroscopy spectra of MG, silicone, S-MG25 and S-MG40 at room temperature.

Fourier transform infrared spectroscopy (FTIR) test (spectrum GX FT with a resolution of 0.1 cm^{-1}) and Raman spectroscopy test [RENISHAW inVia (He:Ne laser, 1.96 eV) confocal Raman system with a beam size of less than 1 μm] were conducted at room temperature on a couple of selected samples. Results are presented in Fig. 6.4 and Fig. 6.5, respectively. As compared with the results of silicone and MG, failure to spot any apparent new peaks and to observe any significant shifts in both S-MG25 and S-MG40 at both millimeter (FTIR) and micron scales (Raman) excludes the possibility of forming any significant new chemical bonding between MG and silicone.

6.2 Shape memory effect

Similar to other hybrid systems investigated in previous chapters, S-MG hybrids, in which silicone works elastic component and MG functions as transition component, are expected to have the SME as well. According to Fig. 6.2, all S-MG hybrids should have a shape recovery temperature same as the melting temperature of MG.

To demonstrate the SME, a round disk shaped piece of S-MG40 was bent by 180^o at room temperature, and then placed inside an oven which was set to 90^{o}C (above the melting finish temperature of MG) with the constraint being maintained till the S-MG40 was fully heated. Subsequently, the 180^o-bent sample was cooled down to room temperature before the constraint was removed. The residual bending of the sample was about 90^o, as shown in Fig. 6.6 (a). Upon immersing into 90^{o}C water, it fully recovered its original flat disk shape [Figs. 6.6 (b) to (f)].

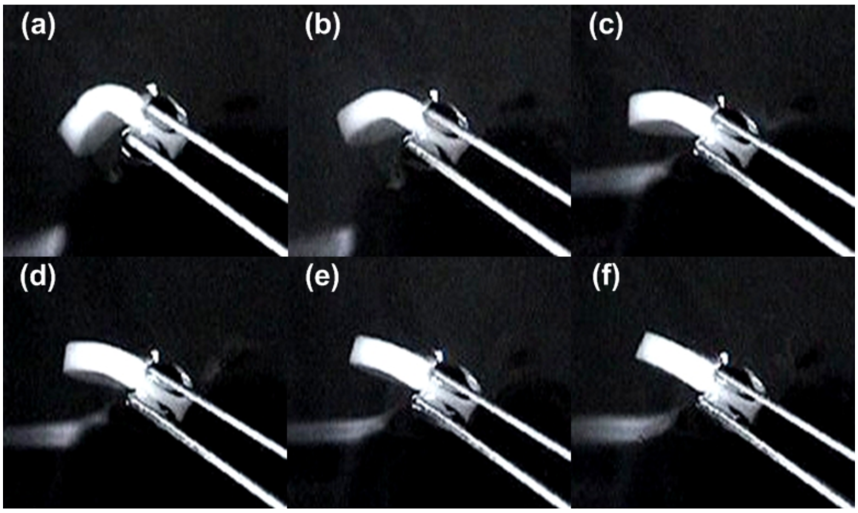

Figure 6.6 Snapshots of shape recovery sequence in a piece of round disk shaped S-MG40 upon immersing into 90^{o}C water.

Note that different from conventional programming procedure for thermo-responsive SMPs (as illustrated in Fig. 2.5), in the above experiment, we actually bent the S-MG40 at room temperature before heating it to soften the transition component. We are able to do so in programming, because the material is highly elastic at room temperature. This issue, i.e., rubber-like feature at low temperatures, will be further investigated in Section 6.3. Of course, we are still able to follow conventional approaches, such as that in Fig. 2.5, to program this S-MG hybrid.

The micro-structures of S-MG40 at different stages are presented in Fig. 6.7. These images were taken by a scanning electron microscope (SEM) (JEOL JSM-5600LV) under the second electron imaging mode. As we can see in Fig. 6.7(a), many circular shaped micrometer-sized balls are distributed (and well separated) in the prepared sample. When stretched to 100% at room temperature (with 100% strain remained during SEM test), many elliptical shaped holes with one small ball in each hole appear in Fig. 6.7 (b_1). Fig. 6.7 (b_2) is the typical image after 100% stretching at 100^{o}C, cooling back to room temperature and then removing the constraint. Instead of elliptical holes, many elliptical shaped particles are observed. After heating to 100^{o}C for shape recovery, inclusions in all freestanding samples are in circular shape again as revealed in Fig. 6.7(c). Since the volume fraction of MG is 40% in this S-MG hybrid, the observed inclusions should be MG balls. They are in circular shape in the as-fabricated sample due to the influence of surface tension during fabrication (mixing at above the melting temperature of MG) in order to minimize the free energy.

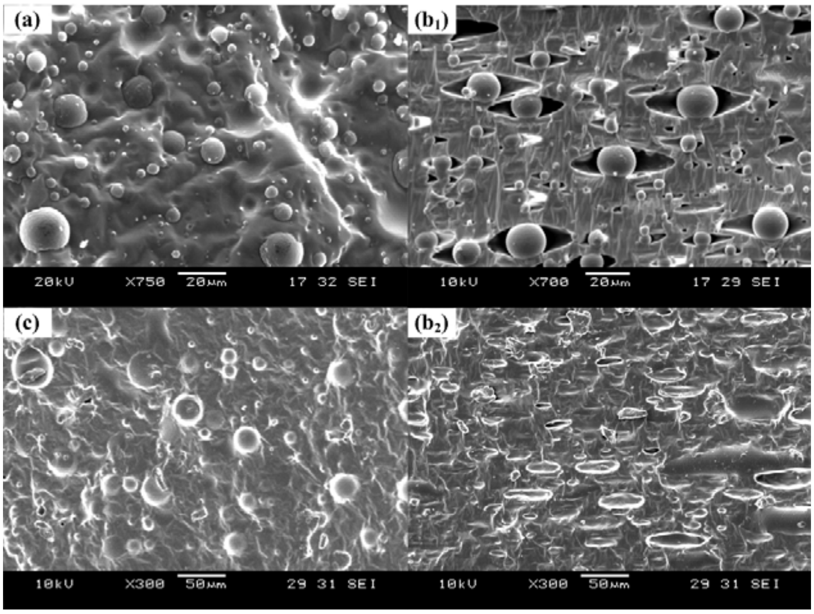

Figure 6.7 SEM images of cryofracture surface of S-MG40. (a) Original sample; (b$_1$) 100% stretched at room temperature; (b$_2$) after 100% stretching at 100^{o}C; (c) after heating to 100^{o}C for shape recovery.

According to Fig. 6.7(b$_1$), it seems that the bonding between silicone and MG ball is not strong, so that we see many eye-shaped features when the sample is stretched to 100% at room temperature. Bear in mind that at room temperature, MG is much harder than silicone, so that MG balls are difficult to deform. It is the elastic deformation of silicone matrix which accommodates the 100% stretching. Further study on the bonding issue will be presented in Section 6.4.

However, at 100^{o}C, which is well above the melting temperature of MG, MG can easily flow and deform to match the deformation of the silicone matrix. Consequently, after programming, we see elliptical shaped MG inclusions with their long axis being parallel to the stretching direction in Fig. 6.7 (b_2). It is obvious that these elliptical shaped MG inclusions also prevent the elastic recovery of the silicone matrix, i.e., MG inclusions help to fix the temporary shape of the S-MG40 sample. After heating to 100°C again, MG melts and thus freestanding S-MG hybrids are able to fully return their original shape. As such, MG inclusions are in circular shape again in Fig. 6.7 (C).

To systematically investigate the influence of MG content on the shape memory properties of S-MG hybrids, a series of experiments (in bending deformation mode as revealed in Fig. 2.6) were carried out to study the shape fixity ratio (R_f) and shape recovery ratio (R_r) of S-MG hybrids with different volume fractions of MG.

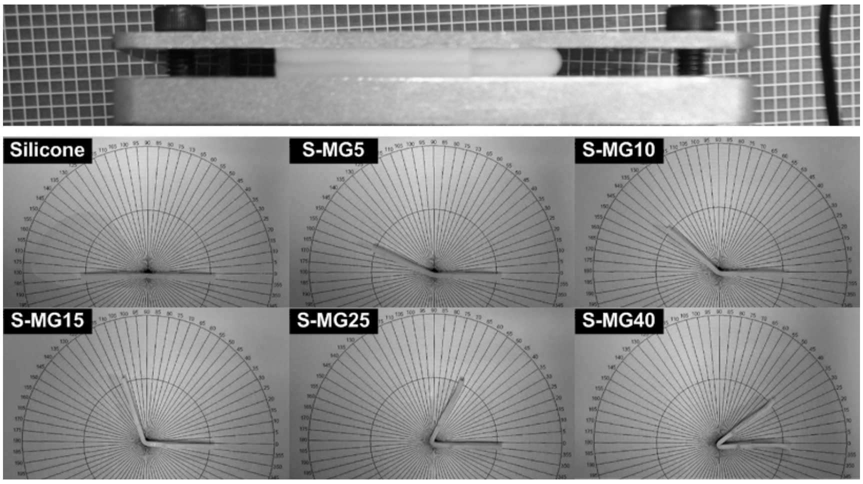

Figure 6.8 Experimental setup for shape fixation test (top) and typical results of freestanding samples after cooling and removal of constraint (bottom).

All tested samples are in dog-bone shape with a thickness of 3 mm. The programming and shape recovery procedure is similar to that described in the early part of this section. All samples were bent to 180^o at room temperature so that there was no gap between the top and bottom parts (refer to top of Fig. 6.8). Hence, radius R marked in Fig. 2.6 is about zero, and therefore the maximum surface strain in both tension and compression is 100% according to Eqn. 2.4.

The samples were heated inside a 100^{o}C oven with the deformed shape maintained. After programming, samples were placed atop a piece of scale paper to measure the residual angle θ_i (refer to Fig. 2.6). Figure 6.8 (bottom) presents the images of the tested samples after programming. After being immersed into 90^{o}C water for shape recovery, all samples were placed atop the scale paper again to measure the remaining angle θ_f (refer to Fig. 2.6). Subsequently, the shape fixity ratio R_f and shape recovery ratio R_r were calculated according to Eqns. 2.5 and 2.6. Table 6.1 lists all measured angles and calculated results. For easy visualization, Fig. 6.9 plots R_f and R_r vs. MG content relationships.

Table 6.1 Shape fixity/recovery ratios of S-MG hybrids.

Sample	θ_i (^{o})	θ_f (^{o})	R_f (%)	R_r (%)
Pure silicone	0	0	0	100
S-MG5	25	0	14	100
S-MG10	43	0	28	100
S-MG15	72	0	42	100
S-MG25	119	0	66	100
S-MG40	145	0	83	100

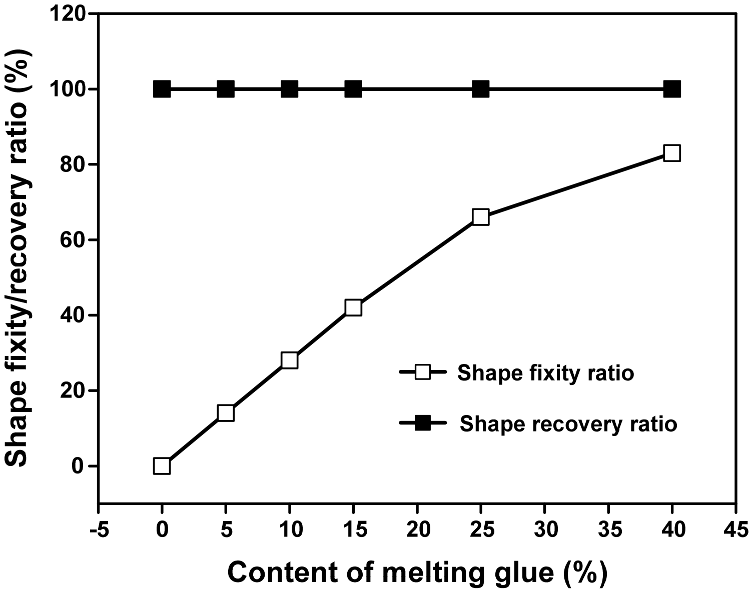

Figure 6.9 Shape fixity/recovery ratios against MG content in S-MG hybrids.

According to Fig. 6.9, the shape fixity ratio of S-MG hybrids increases with the increase of MG content. As expected, the shape fixity ratio of pure silicone is zero since pure silicone is highly elastic within the whole temperature range during programming. A ratio of more than 80% is observed in S-MG40. Bear in mind that the maximum surface strain in both tension and compression during programming is 100% according to the current experimental setup. Obviously, higher MG content means higher resistance against the elastic recovery of silicone, so that a higher shape fixity ratio is resulted.

On the other hand, all S-MG hybrids are able to fully recover their original straight shape, i.e., the shape recovery ratios of all tested samples are 100%. This is due to two reasons, one is high elasticity of silicone, and the other is that the maximum MG content is only

40% so that silicone is able to form a continuous network (evidenced by Fig. 6.7) to ensure full shape recovery.

6.3 Rubber-like behavior

A commonly understanding of conventional SMPs is that at high temperatures (above the transition temperature), these polymers have good elasticity, while at low temperatures (below the transition temperature), they are either brittle (easy to break upon slight distortion) or ductile (able to quasi-plastically deform). For examples, at room temperature, the polystyrene SMP from Cornerstone Research Group, USA is brittle (Dietsch and Tong 2007), while the polyurethane SMP from SMP Technologies Inc., Japan is ductile (Huang *et al.* 2011). The SMP developed by (Luo and Mather 2009) shows good elasticity at room temperature (which is below its transition temperature), but with strong hysteresis and large residual strain. After aging, some shape memory alloys (SMAs) do have certain level of elasticity at below their transition temperature, but their recoverable strain is limited and strong hysteresis is observed (Ren and Otsuka 1997). It should be reasonable to claim that so far, there is not any shape memory material (SMM) which is exactly rubber-like below its transition temperature.

To investigate the elasticity of S-MG hybrids below its transition temperature, uniaxial tensile tests were carried out on dog-bone shape S-MG samples via Instron 5565 Universal Testing Machine. The applied strain rate was 0.1%/s. A 100 N load cell was used. Typical stress vs. strain curves of samples (up to 50% strain) at room temperature are plotted in Fig. 6.10. As compared with the result of MG, the stress vs. strain curves of silicone and S-MG hybrids are more or less in a linear fashion. MG has the highest strength, while with the increase of MG content, the hybrid softens gradually.

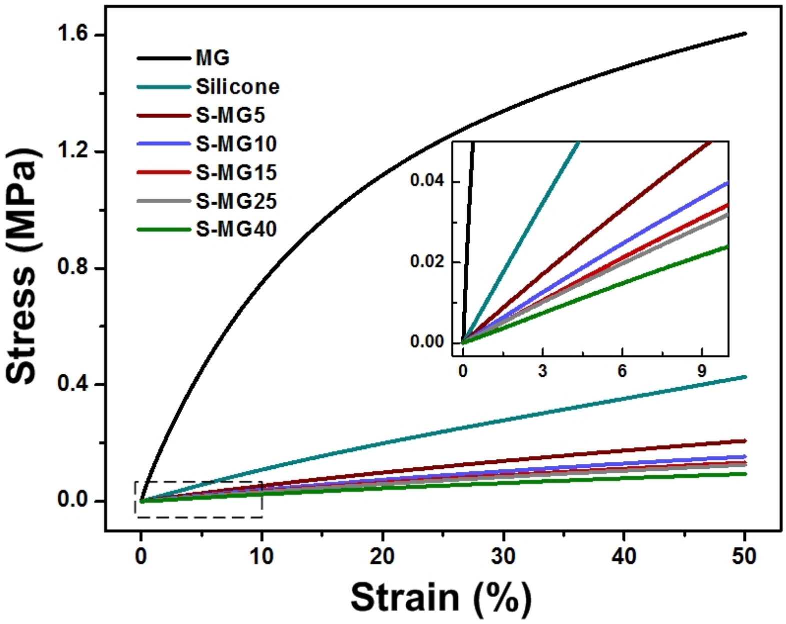

Figure 6.10 Typical stress vs. strain curves of dog-bone shaped S-MG samples together with silicone and MG samples. Inset: zoom-in view of the dashed-line area.

Subsequently, cyclic uniaxial tensile tests at room temperature were conducted on these samples. Typical results are presented in Fig. 6.11. The maximum strains were 30%, 50%, and 100% in three continuous cycles, respectively, at a strain rate of 0.1%/s. For comparison, a pre-tensile strain of 20% was applied on S-MG25 and S-MG40 to examine the influence of pre-strain on their elastic response.

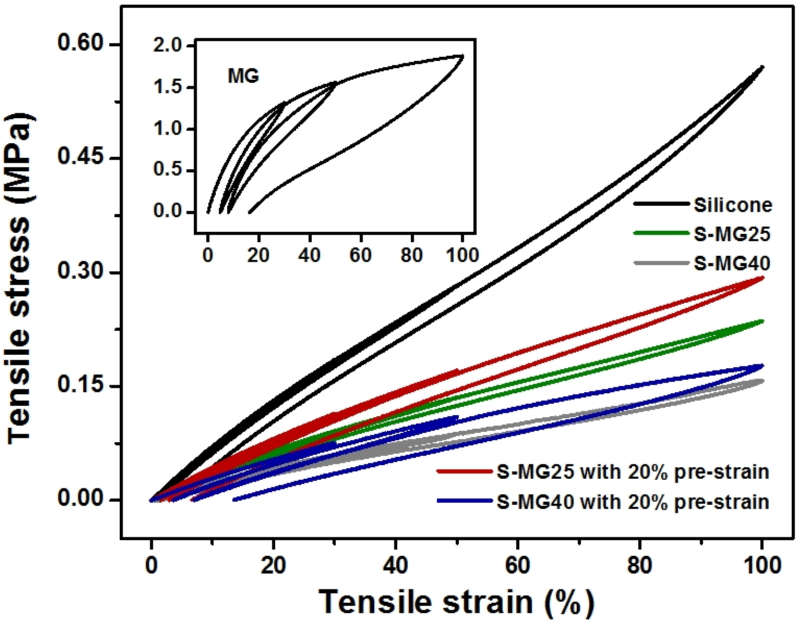

Figure 6.11 Cyclic uniaxial tensile results (to 30, 50 and 100% strains) of silicone, S-MG25 and S-MG40. Inset is the result of MG for comparison.

As we can see, MG is essentially a ductile material, while S-MG25 and S-MG40 are actually more elastic than silicone. Even with 20% pre-strain, they become a bit stiffer but still highly elastic. As such, we may claim that S-MG hybrids are rubber-like at low temperature, in particular within the tensile strain range of 0-50%.

It appears that while pure MG is the stiffest among the tested samples, MG actuallyweakens S-MG hybrids, i.e., the more is the MG content in a S-MG hybrid, the weaker is the S-MG hybrid. In order to have a quantitative comparison, the Young's moduli of silicone, MG and S-MG hybrids are determined from the slope of their respective stress vs. strain curve at the early linear stage (refer to Fig. 6.10 for the experimental results used in calculation). The obtained results are summarized and plotted in Fig. 6.12.

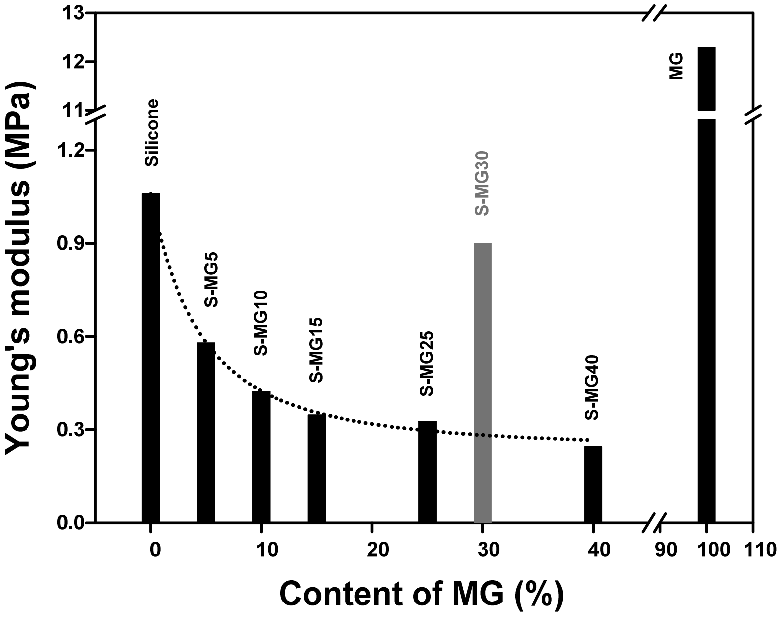

Figure 6.12 Comparison of Young's moduli of silicone, MG and S-MG hybrids. S-MG30 is essentially a mixture of silicone and millimeter sized MG fillers.

It is clear that although pure MG has the highest Young's modulus, 10 times higher than silicone, even with only 5% of MG, the Young's modulus of S-MG5 drops dramatically, only about half of pure silicone. With further increase of MG content, the Young's modulus of S-MG hybrids continuously decreases, but in a more gradual manner, in particular in samples with 15% of MG or more. It suggests a kind of percolation phenomenon. For comparison, S-MG30, which is actually a mixture of silicone and millimeter sized MG fillers (i.e., in the form of MG inclusions embedded inside silicone matrix), was fabricated and tested. As we can see, the Young's modulus of S-MG30 mixture does not fit the trend of S-MG hybrids, but is more comparable to that of silicone.

At this point, we may conclude that unlike that in S-MG30 mixture, silicone and MG are not completely separated in their S-MG hybrids in the form of MG inclusions embedded within silicone matrix. Apart from MG inclusions that we have observed in Fig. 6.7, some MG exists in a miscible form within silicone at submicron scale (hence *invisible* in Fig. 6.7). In other words, in addition to observed micro sized MG inclusions, it is very likely that MG molecular chains and silicone molecular chains are entangled together at nanoscale as illustrated in Fig. 6.13. The miscible MG increases the distance among silicone chains, weakens the interactions among silicone chains, and consequently reduces the stiffness of hybrids, which results in a lower Young's modulus but higher elasticity in S-MG hybrids.

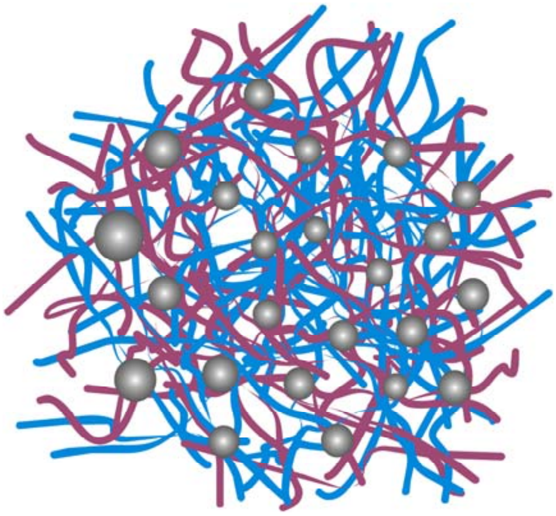

Figure 6.13 Schematic illustration of microscopic structure of S-MG hybrid. Balls are micro sized MG inclusions, while lines represent tangled chains of MG and silicone.

Although MG inclusions are relatively much stiffer, their contribution to the Young's modulus of S-MG hybrids is very much limited. This is because the silicone matrix is highly elastic (so that it is well capable to deform accordingly to accommodate the applied distortion), while the MG inclusions are in a spherical shape and well separated (even with samples with 40% of MG), i.e., lack of geometrical overlapping to effectively transfer force through themselves in particular in uniaxial tension.

The influence of MG inclusions on the SME in S-MG hybrids is apparent. However, beside the weakening effect, the possible contribution of miscible MG to the SME, just like transition segment in conventional SMPs, is yet identified. In order to investigate the influence of miscible MG, a piece of thin film S-MG40 with a thickness of around 25 μm was fabricated by spin-coating atop a piece of silicon wafer (spin speed: 7000 rpm; spin time: 120 s). The as-fabricated thin film was cooked in boiling water for two hours to remove as many MG inclusions at its top surface as possible. Subsequently, instrumented indentation test (a maximum force of 500 mN was loaded at a loading rate of 500 mN/min) with a flat indenter (conical diamond tip with a diameter of 200 μm) was conducted on a hole at 90^{o}C (refer to Fig. 6.14a for the hole, which is very likely formed due to the removal of a MG inclusion). After cooling back to room temperature and unloading, the hole became bigger (Fig. 6.14b) and with a sharper edge (Fig. 6.14d). Heating to 90^{o}C results in almost full shape recovery (Fig. 6.14c). The cross-sectional view presented in Fig. 6.14(d) confirmed that the edge becomes less shaper. Given the dimension of the sharp edge, it is very unlikely that the shape recovery at the edge is due to MG inclusions. It is more likely the result of miscible MG which held the temporary shape of the hole after programming, and became soft again to let the elastic silicone chains return the original shape, i.e., almost full shape recovery in this hole. As such, we may conclude that both MG inclusions and miscible MG contribute to the SME in S-MG hybrids.

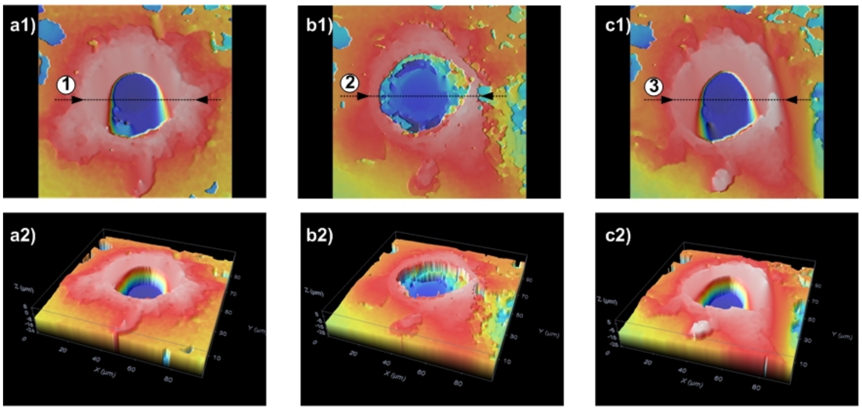

(a) Before indentation (b) After indentation (c) After recovery

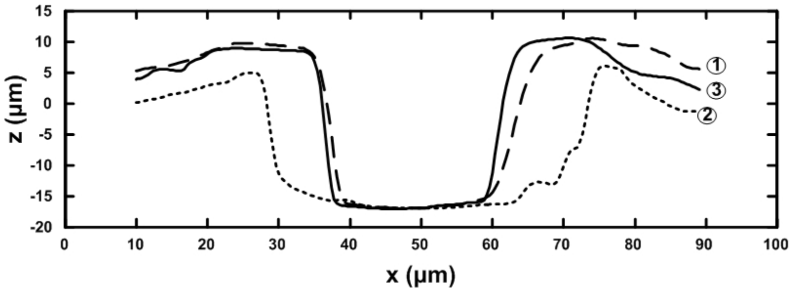

(d) Cross section of SMG thin film

Figure 6.14 The SME in a piece of thin film S-MG40 with a thickness of ~25 μm. Surface scanning (over a square area of 100×100 μm^2) was conducted using a Confocal image profiler.

Figure 6.15 presents the stress vs. strain curves of S-MG40 in cyclic uniaxial tension (to 30%, 50% and 100% strains) at 20°C (well below the transition temperature), 50°C (around the transition start temperature) and 100°C (well above the transition finish temperature), respectively. It is obvious that the response of this hybrid at 100°C shows almost identical stress vs. strain curve in loading and unloading. There is some slight difference between the loading curve and unloading curve in the experiment conducted at 20°C. Good shape recovery is still observed in the experiment carried out at 50°C, but hysteresis is seemingly more significant when the applied strain is over 30%.

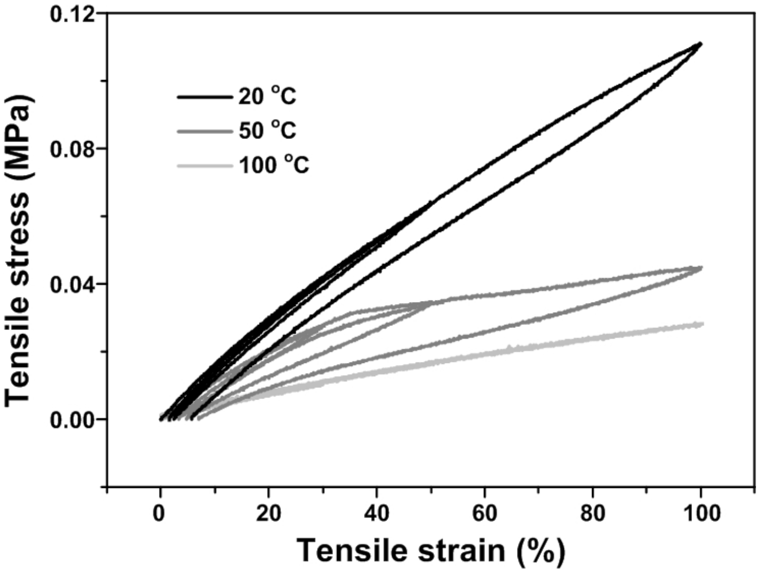

Figure 6.15 Cyclic uniaxial tensile results (to 30%, 50% and 100% strains) of SMG-40 at different temperatures.

Figure 6.16 reveals the rubber-like response (with/without programming) and SME in S-MG25. Before programming, a piece of dog-bone shaped S-MG25 can be easily stretched to over 120% and instantly bounce back at room temperature (Fig 6.16a). After being programmed into bent shape (refer to Fig. 6.8 and the context for the programming procedure), it is still as elastic as before programming (Fig 6.16b). Upon immersing into 90°C water, the programmed sample fully recover its original shape (Fig 6.16c).

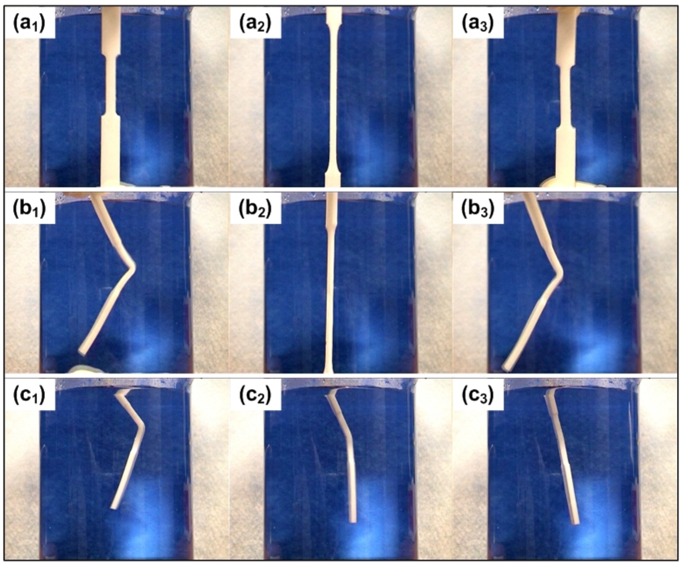

Figure 6.16 Snapshots of rubber-like behavior without (a)/with (b) programming and SME (c) in S-MG25.

Mechanical stability of materials under cyclic loading is a concern of many engineering applications. As revealed in Fig. 6.7(b_1), the bonding between the matrix and MG inclusions is weak, so that when stretched to about over 50% at room temperature, some apparent hysteresis appears in S-MG hybrids either with or without pre-strain (refer to Fig. 6.11 for the cyclic uniaxial tensile results of S-MG25 and S-MG40 with/without 20% pre-strain in tension). The residual strain also increases slightly. Furthermore, mechanical stability of pre-bent S-MG25 was investigated. As shown in Fig. 6.17, the nominal stress vs. nominal strain curves are highly repeatable upon cycling up to 50% nominal strain. Here, nominal strain is defined as the elongation vs. the initial distance between two clamps; and nominal stress is defined as the tensile force vs. the cross-sectional area of the original sample in the middle section. Further loading to 100% nominal strain, hysteresis becomes significant, but the sample is still highly elastic.

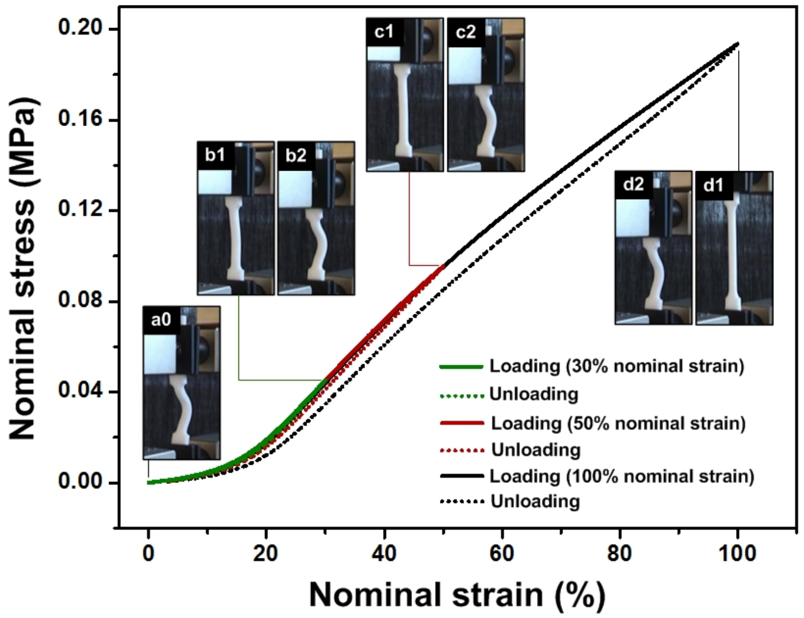

Figure 6.17 Nominal stress vs. nominal strain curve of pre-bent S-MG25 in cyclic uniaxial tension together with snapshots at different maximum stretching (b_1,b_2,b_3) and zero stress (b_2,c_2,d_2) upon subsequently unloading (a_0: original shape).

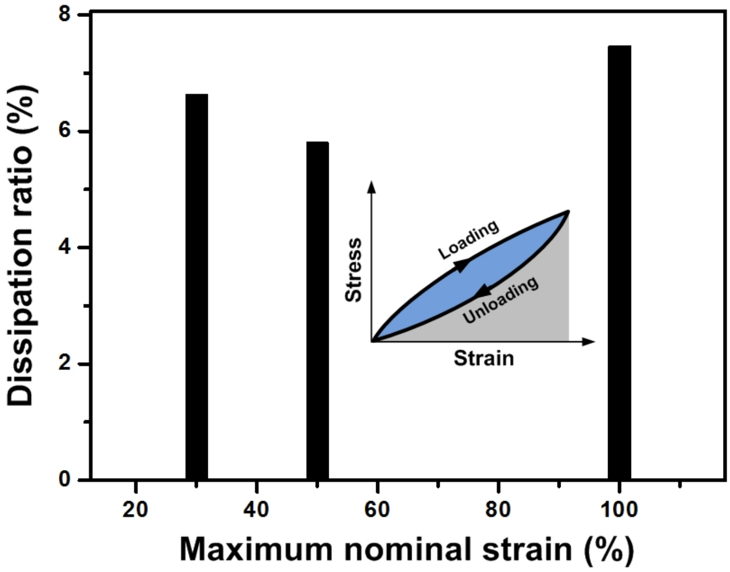

Figure 6.18 Nominal energy dissipation vs. maximum nominal strain. Inset: schematic illustration of the definitions for energies in a cycle.

The nominal energy dissipation ratio vs. nominal strain relationship calculated based on Fig. 6.17 in three cycles is presented in Fig. 6.18. Here, nominal energy dissipation ratio is defined as the ratio of the energy dissipation in one loading-unloading cycle (i.e., the enclosed area marked in the inset of Fig. 6.18) and the total energy upon loading to the required nominal strain (i.e., the grey area plus the enclosed area in the inset of Fig. 6.18). As we can see, the energy dissipation ratio is less than 8% even the maximum nominal strain is 100%.

From application point of view, SMMs with such a rubber-like feature can have a wider range of applications. As shown in Fig. 6.19(a), a star-shaped S-MG25 stent is expanded by means of mounting on a circular shaft which effectively increases the perimeter by 15%. After heating to above the transition temperature and then cooling back to room temperature, the shape of stent is close to hexagon with a larger size. The graphic drawings and images of the mold and shaft used in this experiment are included in Appendix (Figs. A1, A2, A5 and A6). After expansion, the stent can be easily deformed in a rubber-like fashion at room temperature (refer to Fig. 6.19b) to be packed into a catheter and then delivered/deployed at the required location. Shape recovery of the stent can be triggered by means of immersing into 90^{o}C hot water, as shown in Fig. 6.19(c). After the shape is fully recovered, the stent is back to its original size and behaves like a piece of rubber band again (Fig. 6.19d). Subsequently, it is ready to be easily pull back into a catheter to be removed.

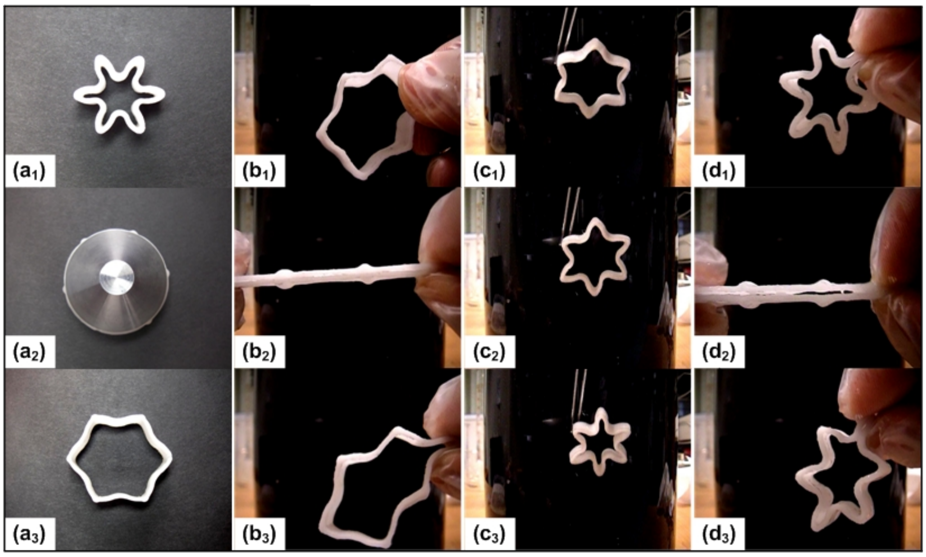

Figure 6.19 Rubber-like retractable stent (S-MG25). (a) Programming; (b) rubber-like after programming; (c) shape recovery upon heating; (d) rubber-like after recovery.

6.4 Thermally induced self-healing

As discussed above, in addition to MG balls, some MG exists in molecular chain form tangling with silicone chains, which plays a part in the SME in both shape fixation and shape recovery. As evidenced by Fig. 6.3, apparently, these MG chains do melt when heated to above the melting temperature of MG. Since MG is normally used as glue to bond materials together, it becomes interesting to check if MG chains in S-MG hybrids have the same adhesion function. It is apparent that the more MG content is in an S-MG hybrid, the stronger is the adhesion, if any, in the hybrid.

So far the S-MG hybrids that we have managed to fabricate have the highest MG content of MG 40%. S-MG hybrids with more than 40% volume fraction of MG turn out to be always sticky and essentially non-curable. As such, S-MG40 was used hereinafter in this section for thermally induced self-healing test. Since there is not any additional adhesion material/curing agent used during healing but heat only, according to the tradition in this field, we still can claim this is self-healing.

A piece of S-MG40 dog-bone shaped sample was stretched at room temperature to fracture into two pieces at a strain rate of 0.1%/s (Instron 5565 Universal Testing Machine) (Fig. 6.20). To ensure that fracture appears at the required location (i.e., in the middle part of the sample) for our convenience in the subsequent experiments, we cut the sample slightly with a sharp pen-knife in its middle part. According to Fig. 6.20, the stress vs. strain curve of the sample with cutting follows about the same trend as that of the perfect sample (without cutting), but the fracture stress is lower.

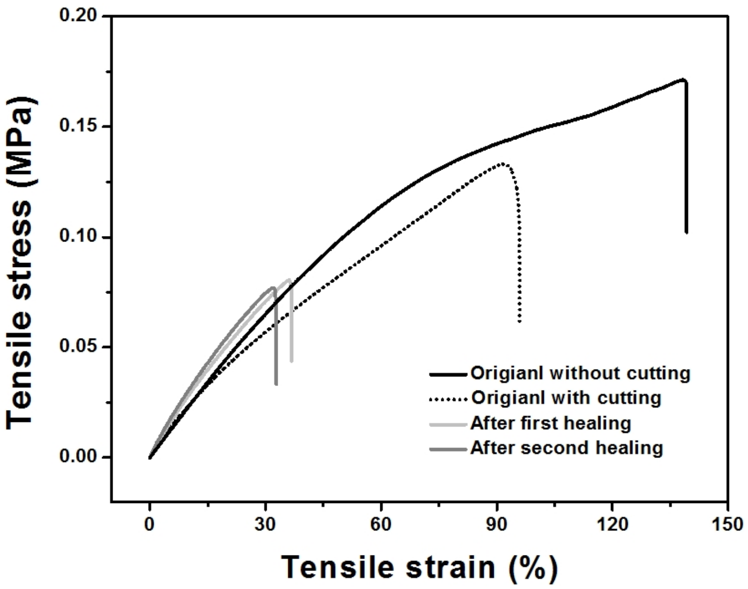

Figure 6.20 Stress vs. strain relationships of S-MG40 before and after self-healing.

In the next step, two fractured two parts were squeezed back into the dog-bone shaped mold, which was used to fabricate this sample, and then heated inside an oven at 100°C for 20 minutes. After cooling back to room temperature (about 22^{o}C), the sample became virtually one single piece again. The healed sample was stretched again under the same testing conditions to fracture again. The fractured sample was healed again following the exact same procedure and then stretched to fracture one more time. Figure 6.20 compares the stress vs. strain curves till fracture of the original samples with/without cutting and the healed samples. Around 50% of strength was recovered even after two healing cycles.

These experimental results are exciting, but more meant for demonstration only. We need a systematical investigation with a well designed testing procedure and well controlled experimental parameters.

Two pieces of cylindrical shaped S-MG40 (with a diameter of 2.5 cm) were prepared following the same fabrication procedure as described in Section 6.1. To examine the self-healing effect, they were pushed together under a pressure of 2×10^{4} Pa and then heated in an oven at 100^{o}C for half an hour. After cooling back to room temperature, the sample (now one single piece) was stretched at a strain rate of 0.1%/s till fracture (into two pieces). This procedure was repeated seven times. Typical stress vs. strain curves are plotted in Fig. 6.21. It appears that from the second healing cycle onwards the stress vs. strain curves are almost identical, which indicates high repeatability after healing. In addition, as shown in Fig. 6.21 (inset), in which we take the fracture stress in the first fracture test (self-healing cycle No. 0) as reference, over 50% strength can be recovered even after seven healing cycles.

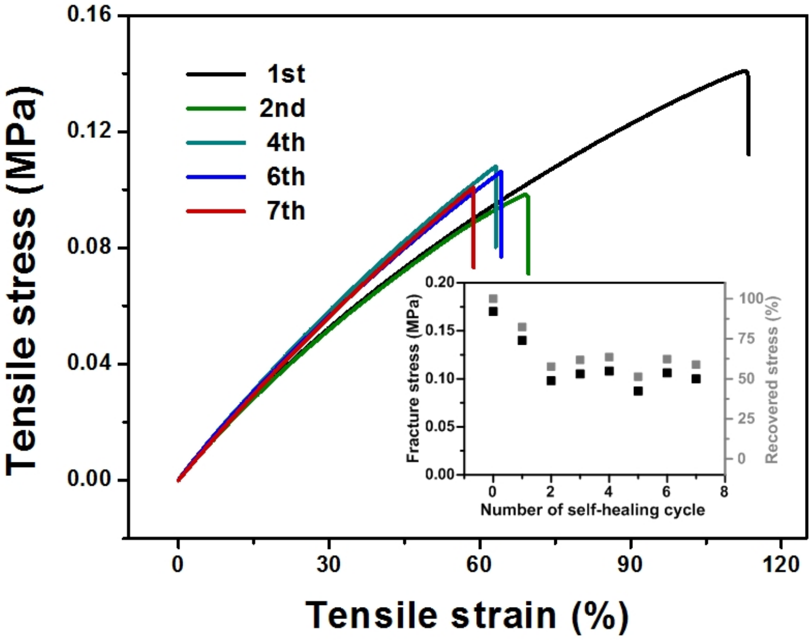

Figure 6.21 Typical stress vs. strain curves of S-MG40 at room temperature after repeated healing. Inset: evolution of actual fracture stress and recovered stress in % against healing cycle number.

As discussed before, MG in S-MG hybrids exists in two forms, micro sized inclusions and molecular chains. In order to identify the exact mechanism behind the repeated self-healing function in S-MG40, a few of additional experiments were conducted. In one experiment, a piece of flat MG was placed atop a piece of flat S-MG40 and then compressed together at 100°C. After cooling back to room temperature, these two layers were partially split. Figure 6.22(a_0) shows side-view (SEM image) of these two detached layers. The right side is MG and the left side is S-MG40. Figure 6.22(a_1) and Figure 6.22(a_2) reveal the contact surfaces of S-MG40 and MG, respectively, after being fully split apart. We can clearly see many micro balls atop MG surface, while many micro sized holes atop S-MG40. Obviously, these balls are micro MG inclusions. They were in the top surface of S-MG40, but pulled out of S-MG40. As revealed in Fig. 6.7(b_1), the bonding between MG inclusion and matrix is weak. Consequently, the contribution of these MG balls to strength recovery, if any, is limited to the first couple of healing cycles. After they are pulled out, MG molecular chains should be the major player in the subsequent healing cycles. Hence, the fracture stress should decrease in the first couple of cycles and then becomes more or less stable. This trend is exactly revealed by the inset of Fig. 6.21.

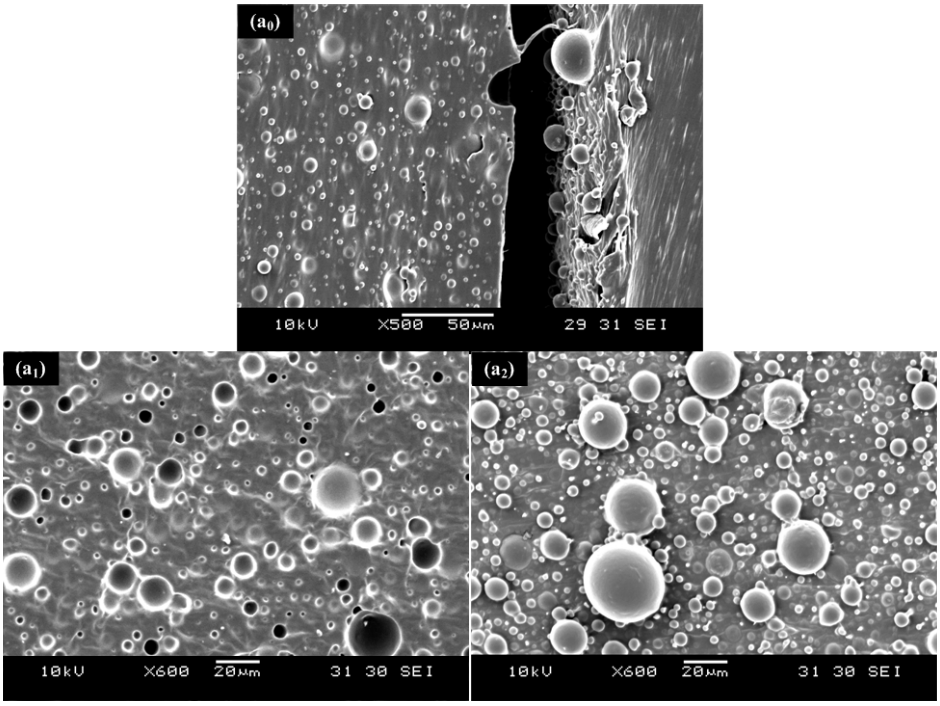

Figure 6.22 SEM images (SEI) of MG/S-MG40 sample after pulling out test.

Furthermore, bonding strength of different interfaces (MG/MG, S-MG40/S-MG40, silicone/MG, S-MG40/MG, silicone/S-MG40, and silicone/silicone) was experimentally determined. The standard testing procedure in preparing a sample (with two parts) to measure the bonding strength between them is to push two materials (all in a cylindrical shape with a diameter of 2.5 mm and a flat surface at the interface) together under a pressure of 2×10^4 Pa at $100^{o}C$ for 20 minutes and then cooling back to room temperature. Subsequently, fracture test (in uniaxial tension) is conducted at a strain rate of 0.1%/s under a 1kN load cell (Instron 5565). The fracture stresses, i.e., bonding strength, of different interfaces are summarized in Fig. 6.23. It is apparent that the bonding strength between S-MG40 and S-MG40 is about half of that between MG and MG, but much higher than the other types of interfaces.

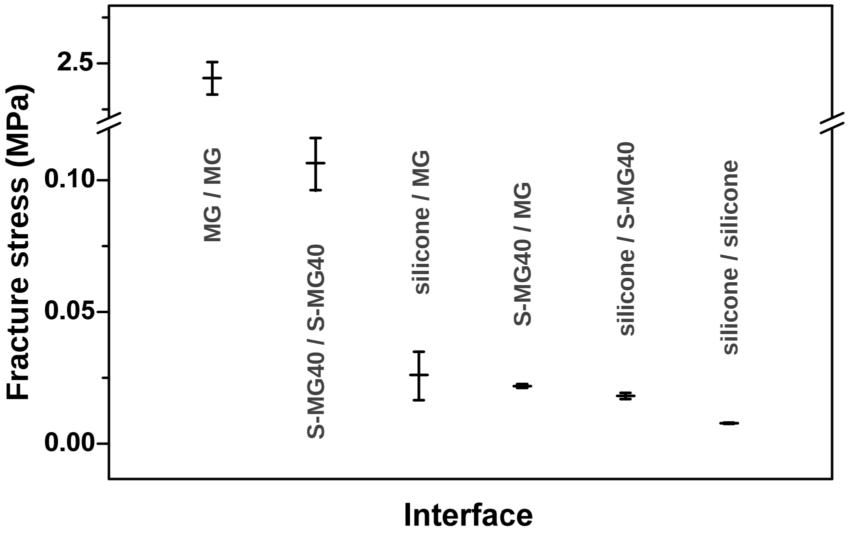

Figure 6.23 Fracture stresses of different interfaces.

From Figs. 6.22 and 6.23, it can be further confirmed that MG balls might be a bit helpful in the first one or two healing cycles, but should not be the major contributor in the subsequent cycles. This is evidenced by the drop of fracture stress in the first two healing cycles (Fig. 6.21, inset). MG molecular chains are the real player behind the repeated self-healing function. After about two healing cycles, MG molecular chains provide an almost constant bonding strength to the healed S-MG40.

The reported self-healing mechanism in S-MG40 is different from most of traditional self-healing techniques, which are intended to heal only small cracks with the help of curing agent either pre-embedded inside microcapsules or delivered to the required location through a network of micro-channels (Kirkby *et al.* 2009; White *et al.* 2001). They are more applicable to heal micro-cracks with limited size and the healing process ceases once the healing agent is used up. In addition, since it is a polymerization process, instant healing with a couple of minutes is difficult to achieve.

On the other hand, Brownian motion induced polymer chain crawling has also been applied for self-healing but with limited performance in terms of strength recovery (De Gennes 1971). In recent years, the Diels-Alder reaction (Chen *et al.* 2002; Zhang *et al.* 2009), metal-ligand coordination (Kersey *et al.* 2007), hydrogen bonding (Cordier *et al.* 2008; Sijbesma *et al.* 1997; Sivakova *et al.* 2005) have been proposed as alternatives to achieve repeated self-healing in composites but in a relatively much slow speed in healing.

The most recent and another very interesting development in the field of self-healing materials is healing of supramolecular polymers by UV light (Burnworth *et al.* 2011). Fundamentally, this is a melting for healing process in which heat is applied in an optical manner. Similar concept of melting for healing has been achieved by (Rodriguez *et al.*

2011), which also have the SME. The S-MG40 reported here has the additional advantage of rubber-like feature at low temperatures atop the excellent SME and thermally induced self-healing function.

To further demonstrate the effectiveness to achieve repeated and instant self-healing function, a piece of cylindrical S-MG40 (8 mm in diameter) with a NiTi SMA helical spring (diameter of wire: 1 mm; diameter of spring: 5 mm) embedded inside was fabricated (Fig. 6.24). This SMA spring is in martensite at room temperature and can be easily stretched in a quasi-plastic manner to very long. Upon heating (e.g., joule heating), it is able to fully recover its original length, while in the case of constrained recovery, a high actuation stress in NiTi (up to 500 MPa in uniaxial tension) can be generated (Huang 2002).

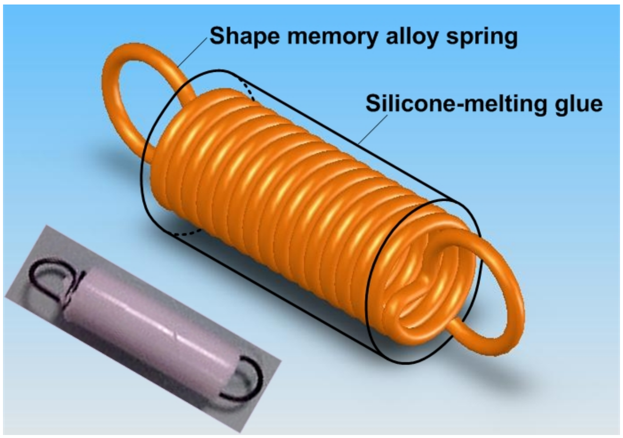

Figure 6.24 S-MG40 SMH with SMA spring embedded inside (illustration and real picture of as-prepared sample).

A full self-healing process is demonstrated in Fig. 6.25. The sample was rubber-like at room temperature. Upon bending, it was able to elastically bounce back (Fig. 6.25a). It did not break unless a high pulling force was applied (Fig. 6.25b). Even being stretched to fracture, the helical SMA spring was able to link the fractured two parts together. A 6 V rechargeable battery was connected to the two ends of the SMA spring for joule heating (Fig. 25c). Instantly, two fractured parts were pressed together when SMA spring was joule heated. Simultaneously, S-MG40 was heated under the pressure from SMA spring for self-healing. After the power supply was switched off, the sample cooled back to room temperature in air. Five minutes later, it became as elastic as before upon bending (Fig. 6.25d).

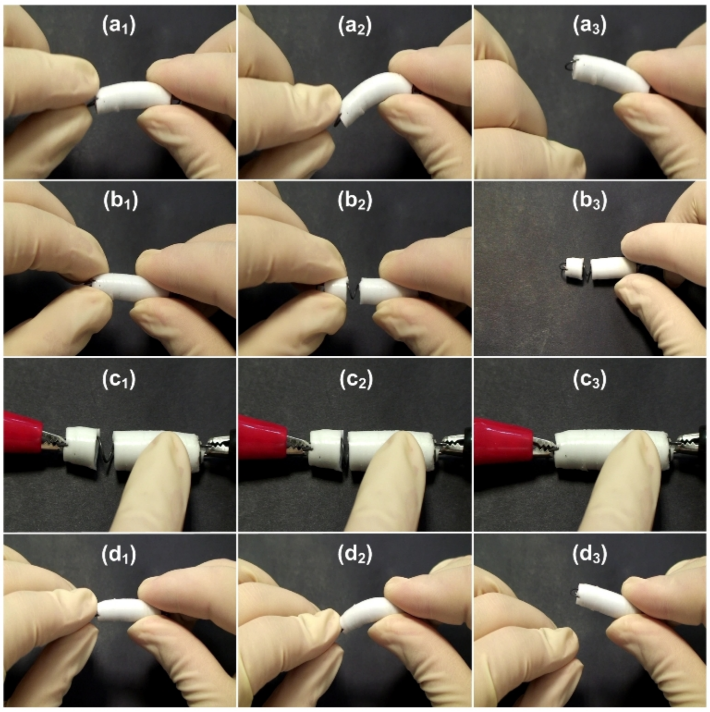

Figure 6.25 Snapshots of self-healing process of S-MG40 with a piece of SMA spring embedded inside.

We should bear in mind that the healing time can be greatly shortened if an effective cooling method (e.g., using iced-water) is applied. Furthermore, with a sensing mechanism integrated into the sample (e.g., by monitoring the change in resistance in SMA when distorted), one can eventually achieve self-sensing/self-healing.

6.5 Summary

We have developed a silicone and melting glue (S-MG) based SMH. We show that S-MG hybrids are rubber-like at both high and low temperatures, have excellent SME and repeated instant self-healing function. The mechanisms behind these features are clearly identified with hard evidence from experiments. It is proved that while micro sized MG inclusions play a part in the SME, tangled polymer chains of MG (and silicone) contribute to the rubber-like phenomenon and repeated instant self-healing function atop the SME. This tangling effect enables a seamless combination of high elasticity, shape recovery and repeated instant self-healing to be simultaneously achieved.

Chapter 7 Design of Shape Memory Hybrids with Required Features

Up to now, the basic concept and working mechanism of shape memory hybrids (SMHs) have been investigated, and further verified in a couple of silicone based systems to demonstrate the feasibility and flexibility in realizing the shape memory effect (SME) along with other novel features.

However, the actual power of SMH is far beyond what have been revealed in these examples. In this chapter, we provide a few more examples to show how to design a SMH with tailored features to meet the requirements from engineering applications.

7.1 Electrically conductive SMHs

Joule heating a thermo-responsive SMM by means of directly passing an electrical current for shape recovery is convenient in many real engineering applications. The SMHs we have presented so far are silicone based, and are electrically non-conductive, since all components are essentially electrically non-conductive in nature. From engineering application point of view, the most convenient and effective approach to enable them to have good electrical conductivity for joule heating is to load them with electrically conductive fillers.

In this section, taking silicone-paraffin wax (S-PW) hybrid as an example, we show how to achieve good electrical conductivity by means of blending with short carbon fibers (SCFs) for joule heating.

7.1.1 Preparation of electrically conductive S-PWs

As presented in Chapter 4, all types of shape memory phenomena have been reproduced in S-PW hybrids. However, they are lack of the electrical conductivity for joule heating.

As a common practice, many types of conductive fillers, such as carbon black (CB), graphite (G), carbon fiber (CF), carbon nanotube (CNT) and various kinds of micro/nano sized metallic particles, have been used, either individually or synergistically, to enhance the electrical conductivity of polymers, including shape memory polymers (SMPs) (Leng *et al.* 2008a; Leng *et al.* 2008b; Thongruang *et al.* 2002; Wang *et al.* 2002). The percolation threshold of filler content for electrical conductivity varies according to the exact type/shape of filler(s) and distribution. For instance, the percolation threshold of graphite filled high-density polyethylene is about 50wt% (Thongruang *et al.* 2002). Fillers with a high aspect ratio generally have a lower threshold of percolation. Aligned conductive fillers significantly enhance the electrical conductivity in the alignment direction (Leng *et al.* 2008a; Leng *et al.* 2008b).

The viscosity of this particular silicone used in S-PWs before curing is not low, which greatly limits our choice of conductive fillers. Carbon fiber was selected due to its normally lower threshold of percolation for electrical conductivity.

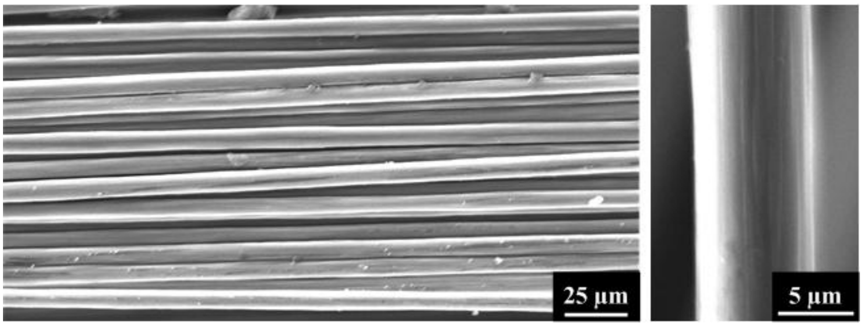

Figure 7.1 SEM images of carbon fiber bundle (left) and one single fiber (right).

Table 7.1 Technical data of carbon fiber.

Property	Unit	Value
Tensile strength	MPa	3530
Young’s modulus	GPa	230
Maximum elongation	%	1.5
Density	g/cm^3	1.76
Coefficient of thermal expansion along axial direction	10^{-6}/K	0.4 ~ 1.0

Carbon fiber (TORAY carbon fiber, T300) has a diameter about 8 µm as shown in Fig. 7.1. Its important properties relevant to current study are listed in Tab. 7.1. Long carbon fibers are more effective in lowering down electrical resistivity of a hybrid, but they may also significantly deteriorate the SME. This is because the Young’s moduli of CF and silicone are remarkably different (230 GPa and 1 MPa, respectively. Refer to Tab. 7.1 and Fig. 6.11). Thus, dislocation between silicone and long fiber is much easier to occur during distortion. Thus, short carbon fibers (SCFs), cut from long ones by a precision slider to about 1 mm long, were used. Nevertheless, the total amount of SCF should not be too high in order to prevent deterioration of the SME.

The fabrication procedure of S-PW-CF hybrids is essentially the same as that of S-PW-GF reported in Chapter 4. A few samples with different compositions were produced. Refer to Tab. 7.2 for details of these samples.

Table 7.2 Composition (in terms of volume fraction) and resistivity of fabricated conductive SMHs.

Sample name	S (%)	PW (%)	SCF (%)	Resistivity (Ω.mm)
S-PW28-SCF2	70	28	2	35.6
S-PW27-SCF3	70	27	3	30.2
S-PW25-SCF5	70	25	5	23.8
S-PW23-SCF7	70	23	7	19.1

Typical microscopic morphology of S-PW-CF (S-PW23-SCF7) is presented in Fig. 7.2, in which dark particles are PW and SCF is seemingly uniformly distributed without any preferential orientation. A SCF network is clearly observed in a little cavity near the sample edge (inset in Fig. 7.2), from which we may logically reason out that SCFs form a network with high order of overlapping even inside of the hybrid.

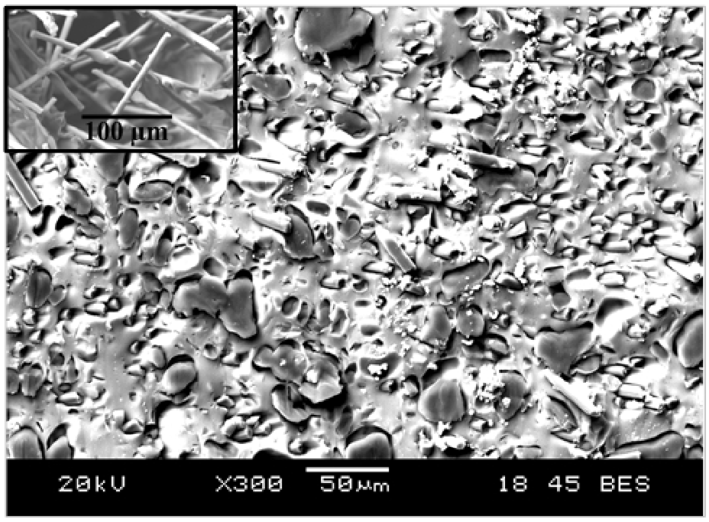

Figure 7.2 SEM images (BSEI) of S-PW23-SCF7. Inset: SCF network in a little cavity near sample edge.

7.1.2 Shape recovery by joule heating

All S-PW-SCF samples have low electrical resistance (refer to Tab. 7.2) and are suitable for joule heating. As shown in Fig. 7.3(a), a piece of straight S-PW23-SCF7 (20.0×2.0×1.5 mm) was programmed at 80°C into a curved shape. To ensure good electrical connection and high flexibility, both ends of the sample were wrapped with aluminum foil adhesive tape and then connected to 30 V DC power (provided by ISO-TECH, IPS 303DD with a voltage range from 0-30 V) through soft carbon fiber bundles. Once the electrical power was switched on, shape recovery almost finished within 2.25 seconds (Fig. 7.3a to e). The sample did not fully return its original straight shape largely due to the constraints at both ends. The experiment was repeated for ten times. No apparent deterioration was observed.

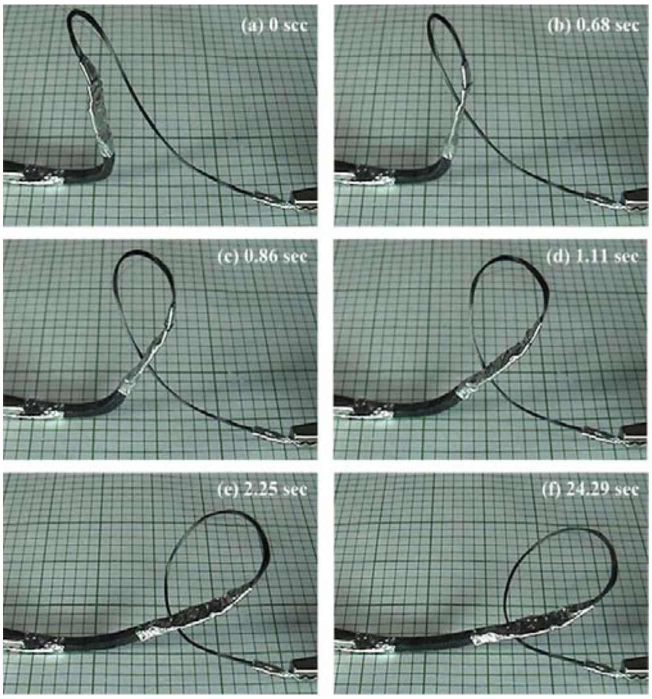

Figure 7.3 Snapshots of the shape recovery sequence in S-PW23-SCF7 upon joule heating.

To investigate the joule heating effect in details, an infrared video camera (NEC San-ei instruments, TH71-717) was used to monitor the temperature distribution within the S-PW23-SCF7 sample (same piece as tested in Fig. 7.3, but in its original flat shape, i.e., without programming). Again, 30 V DC power was applied. Typical infrared images (top surface of sample) are presented in Fig. 7.4. It can be seen that temperature distribution was actually not uniform within the sample. For most of the area, in particular within the middle part, temperature quickly reached 100°C within 4.23 seconds. However, after that, the sample started to cool although the electrical conditions were maintained the same. By tracing the temperature variation at a particular point (located at the center of sample), Fig.7.5 reveals cyclic up and down in temperature against heating time.

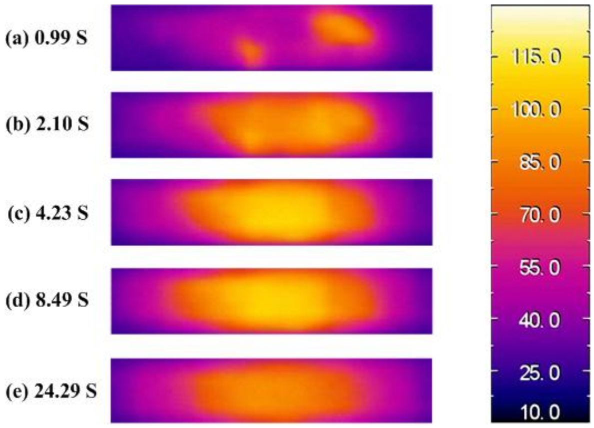

Figure 7.4 Temperature distribution within S-PW23-SCF7 SMH with 30 V DC power applied.

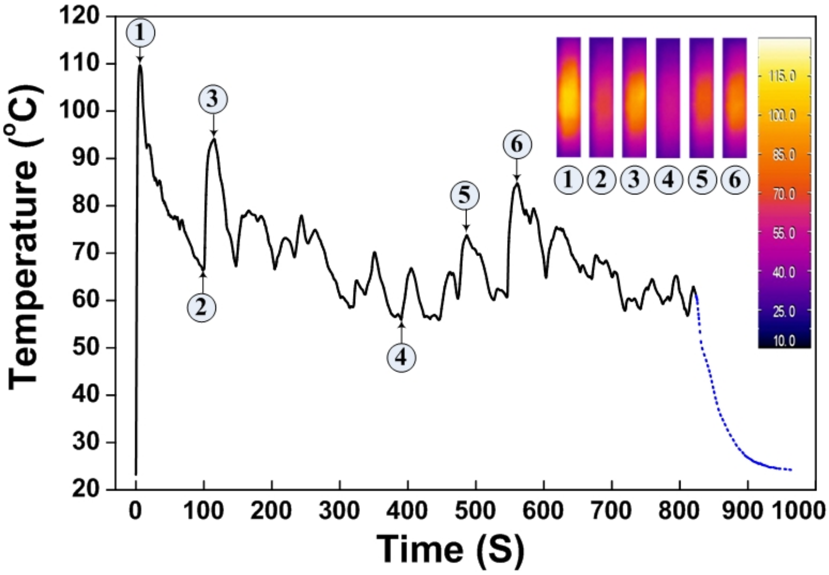

Figure 7.5 Temperature variations against heating time at the center point of S-PW23-SCF7 (insets: infrared images of sample at six occasions and temperature bar). Solid line: in joule heating (power on); dotted line: power off.

As we can see in Fig. 7.5, at point 1 (within six seconds) temperature reached the maximum, and then it started to decrease gradually till about half at point 2. From point 2 to point 3, joule heating effect strengthened again, so that temperature quickly reached another peak but at a lower level. Such a temperature up and down process repeated continuously in a more or less periodical fashion until the power was switched off.

This observed temperature up and down phenomenon, which indirectly reflects the variation of electrical resistance in a material during joule heating, is known as the positive temperature coefficient (PTC) effect in the literature (Xi *et al.* 2004; Zhang and Feng 2003), and can be explained by means of thermal expansion induced breakdown of electrically conductive network as follows.

Refer to Tabs. 4.1 and 7.1. Silicone has a much higher linear coefficient of thermal expansion than that of CF. Upon joule heating, high temperature induces significant volume expansion in silicone, which causes breakdown of the conductive SCF networks at some locations due to high Young’s modulus and low thermal expansion nature of CF. Subsequently, the resistivity of sample increases accordingly, and sample temperature starts to drop until the conductive network is partially recovered at low temperatures, so that sample temperature increases again. Only after a number of up and down temperature cycles, the sample temperature reaches static.

This phenomenon may be utilized as an additional function to provide an automatic protection mechanism to prevent these conductive SMHs in joule heating from overheating.

7.2 SMHs with narrow transition temperature range

From application point of view, a narrow transition temperature range ensures a higher responsive speed for a SMM. The overall transition temperature range of SMPs is normally around 30°C. Even for shape memory alloys (SMAs), it is normally about 20°C.

Based on the concept of SMHs, we may achieve an extremely narrow transition temperature range if water/ice is used as the transition component, so that the transition temperature is narrowed down to ±0°C.

Instead of water/ice, which limits the work temperature range to around ±0°C, it is well known that melting of some crystalline metals/alloys can also be within a very narrow temperature range, so that they can be selected according to the required recovery temperature in a particular application as the transition component in a SMH .

Previously, low melting point alloy (LMPA) has been added into polymers to increase their electrical conductivity (Michaeli and Pfefferkorn 2006). In current study, LMPA (Fluka 95430 Woods metal, Sigma-Aldrich Pte Ltd), which has a nominal melting point about 75°C provided by the producer, was selected as the transition component, while the elastic matrix was still the same silicone, i.e., SYLGARD® 184 Silicone Elastomer. The fabrication procedure of S-LMPA hybrids is essentially similar to that of other silicone based SMHs discussed above. The main steps are briefly summarized here.

- At 90°C, a specified amount of LMPA is mixed with silicone and stirred well before cooled to room temperature (about 22°C). To avoid LMPA's deposition to the bottom of a sample due to its much higher density than that of silicone, slightly pre-curing of silicone at 50°C to enhance its viscosity is a practical approach that can be applied.

- The mixture is poured into a mould with the required dimensions.
- The mould is placed inside a vacuum chamber for 10 minutes to remove entrapped air bubbles.
- The mould is placed inside an oven at 50°C for ten hours for full curing.

The distribution of LMPA within silicone matrix can be found in Fig. 7.6, in which the sample is S-LMPA25, i.e., the volume fraction of LMPA is 25%. Since the LMPA is made of bismuth (atomic number 83), tin (atomic number 50), lead (atomic number 82) and cadmium (atomic number 48), it is obvious that the mean atomic number of this LMPA is much higher than that of silicone. Hence, the bright particles in Fig. 7.6 are LMPA inclusions, which have a size around 20 μm in diameter and are distributed reasonably uniform within silicone matrix.

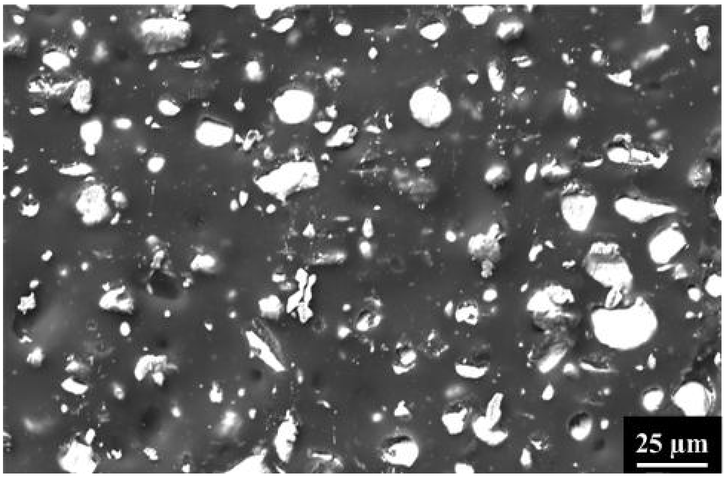

Figure 7.6 SEM image (BSEI) of S-LMPA25.

DMA (DMA Q800, TA) and DSC (DSC Q200, TA) results of S-LMPA25 are presented in Fig. 7.7. The heating ramp in both tests was 1°C/min. According to Fig. 7.7, the DSC results of S-LMPA25 and LMPA reveal that the melting temperature range and peak of S-LMPA25 are about the same as that of pure LMPA, which indicates limited chemical reaction, if none, between silicone and LMPA, so that one can precisely predict the recovery temperature and range of a S-LMPA from that of LMPA. A very narrow melting temperature of 5°C is observed in LMPA, which is further confirmed by the DMA result of S-LMPA25.

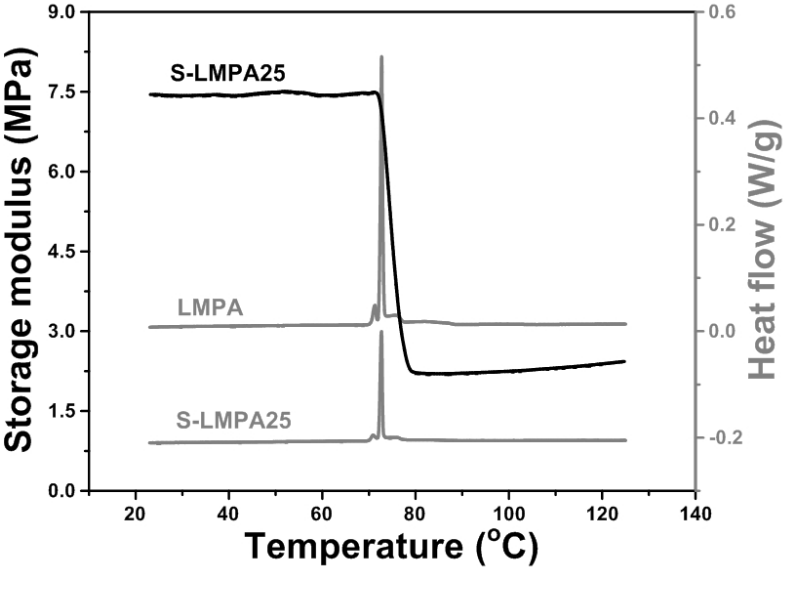

Figure 7.7 DMA and DSC results of S-LMPA25 (together with pure LMPA for reference) upon heating.

In order to investigate the SME, a piece of S-LMPA25 (50×12×2 mm) was programmed (by means of bending at 100°C and subsequently cooled to room temperature) and then gradually heated inside a water tank with temperature controlled within ±0.5°C. As revealed in Fig. 7.8 (pictures), full shape recovery was observed. Furthermore, shape recovery occurred largely within 72°C (c) to 76.5°C, i.e., with about 4.5°C. To have a clearer visualization, the corresponding shape recovery ratios were calculated according to Eqn. 2.6. As we can see, most of shape recovery (80%) was actually finished within 3°C.

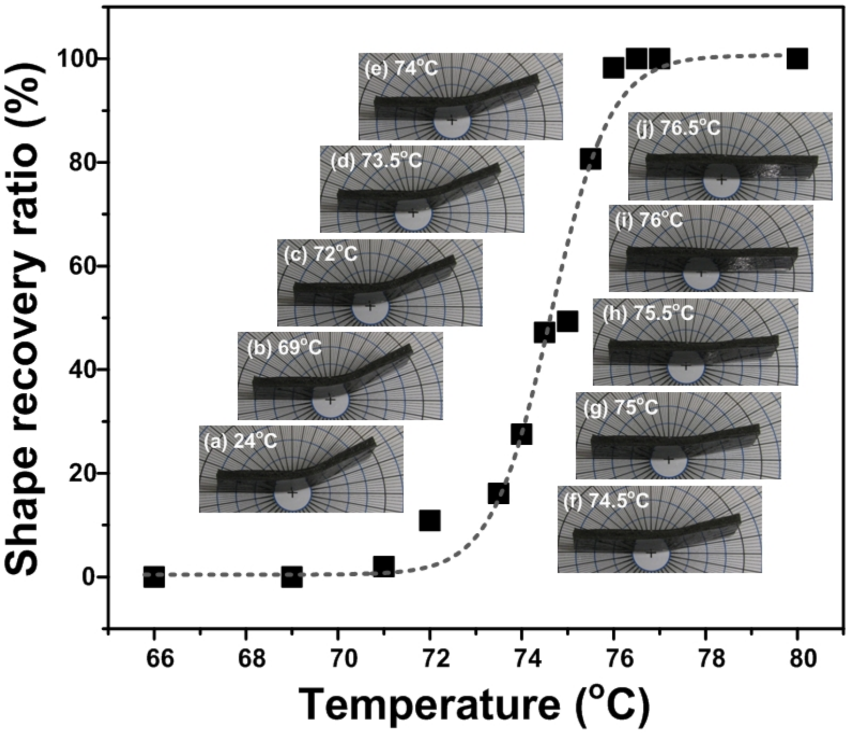

Figure 7.8 Shape recovery ratio against heating temperature in S-LMPA25 together with selected pictures taken at some particular temperatures. Black square: experimental results; dashed line: data-fitting.

It addition to a sharp melting temperature range, high thermal conductivity of LMPA is also helpful to achieve quick recovery in this S-LMPA.

7.3 Pressure-responsive SMHs

The pressure-responsive SMH presented in Section 5.3.3 is actually activated by heat, i.e., the hybrid is essentially thermo-responsive, but heat is self-generated during crystallization of an embedded component, which is triggered by pressure. In this section, we present a concept to achieve real pressure-responsive SMHs.

Refer to Fig. 7.9(a), in which solid inclusions are randomly dispersed within an elastic matrix. After being programmed (by means of vertically compressed at high temperatures), the inclusions turn to be in elliptical shape, while the hybrid is also shorter in height (Fig. 7.9b). Instead of heating to trigger shape recovery, we may compress the hybrid further at room temperature to break the inclusions. Consequently, the constraint from the inclusions to prevent elastic recovery of the matrix is reduced (or even eliminated), so that shape recovery is resulted (Fig. 7.9c). It is apparent that a critical issue here is materials selection, a right inclusion material which is able to easily and quasi-plastically deform at high temperatures and brittle at low temperature, and a right matrix material which is flexible and able to survive under high compression and even impact loading.

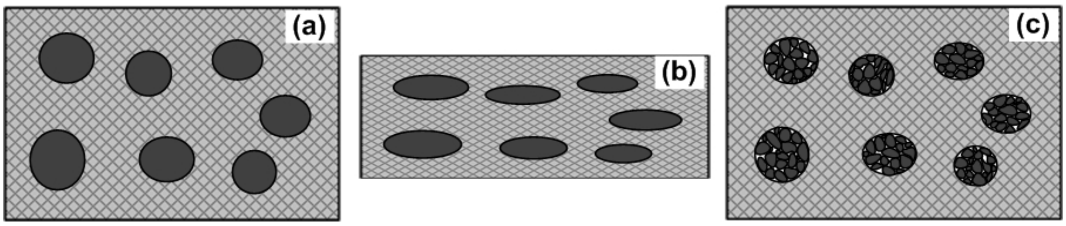

Figure 7.9 Mechanism of pressure-responsive SMH. (a) original shape; (b) programmed shape; (c) recovered shape after compression.

For the purpose of proof of concept, a sponge filled with copper sulphate pentahydrate (CSP) was prepared and tested to demonstrate the basic working principle. The sample fabrication and testing procedure is as follows.

- The sponge is compressed in the horizontal direction (refer to Fig. 7.10a for the horizontal direction) and then dipped into saturated high temperature copper sulphate aqueous solution.
- Let temperature gradually cool down and thus CSP crystals grow inside the deformed sponge till the sponge is fully filled with CSP crystals.
- After being taken out of copper sulphate aqueous solution, and constraint removed, CSP crystals are stiff and able to prevent elastic recovery of sponge. A shorter sample is obtained (Fig. 7.10a).
- Subsequently the sample is hammered in the vertical direction. The sample becomes longer in the horizontal direction (7.10 b).

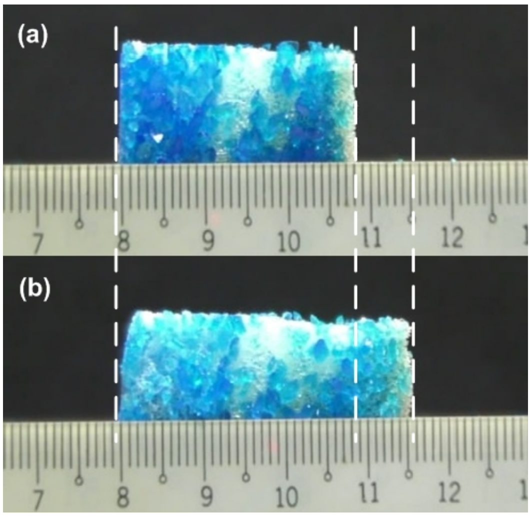

Figure 7.10 Pressure-responsive shape recovery of sponge-CSP hybrid. (a) After programming; (b) after being hammered in the vertical direction.

As we can see, above experiment successfully demonstrates the basic concept. In the next step, we examined the pressure-responsive feature in a piece of S-PW25. The original sample (Fig. 7.11a) was programmed by means of uniaxial compression in the vertical direction at 70°C and then cooled down to room temperature before constraint being removed (Fig. 7.11b). A substantial amount of compression was maintained. After being hammered in the vertical direction, the original height was largely recovered (Fig. 7.11c).

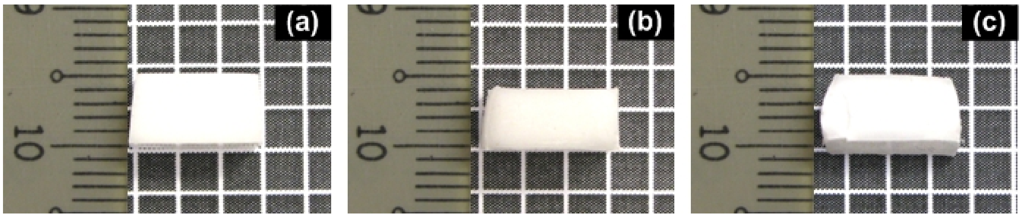

Figure 7.11 Pressure induced shape recovery in S-PW25. (a) original shape; (b) after programming; (c) after hammering.

As discussed in Section 5.2, shape fixation of a S-SAT hybrid can be induced by mechanically tapping instead of following the standard thermo-mechanical programming procedure for conventional thermo-responsive SMPs/SMHs. On the other hand, SAT is fragile due to its brittle salt crystal nature. We may utilize these features of SAT for pressure induced shape fixation and pressure induced shape recovery.

A piece of straight S-SAT50 sample (45×12×2 mm in dimension) was heated to 85°C to fully melt SAT, and then cooled to room temperature. SAT inside the sample was still in liquid form (Fig. 7.12a). Subsequently, the sample was bent and tapped once. After the bending constraint was removed, the sample was programmed into a curved shape, which was rigid due to pressure-induced re-crystallization of SAT (Fig. 7.12b). In the next step, the bent sample was hit by a hammer (Fig. 7.12c) and the original straight shape was fully recovered (Fig. 12d).

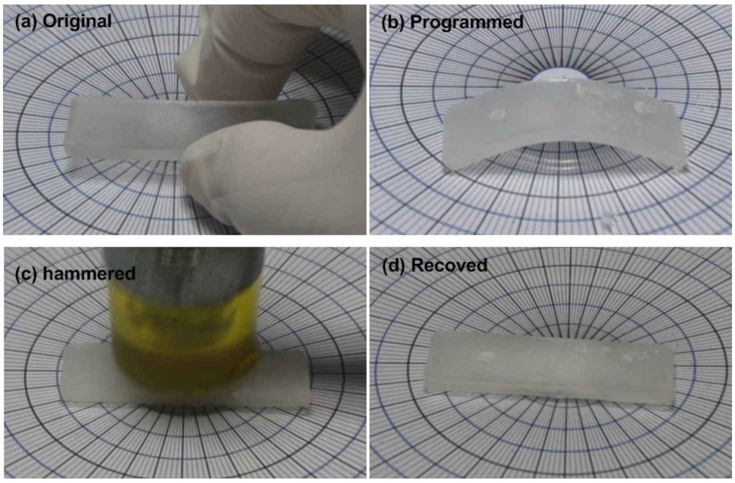

Figure 7.12 Snapshots of pressure-induced shape fixation and shape recovery in S-SAT50.

7.4 Heating/cooling-responsive SMHs

At present, so called thermo-responsive SMMs, including SMA, SMP and SMH, are actually meant for heating-responsive only, i.e., the actuation of them is by means of heating. Based on the concept of SMHs, we can design cooling-responsive SMHs, in which the transition component softens upon cooling. What is presented in this section is a SMH, which is thermo-responsive, either by means of heating or cooling for activation.

Tin is a malleable, ductile and highly crystalline silvery-white metal with a melting point about 232^{o}C, which may change according to its exact size (Lee *et al.* 2011). Tin has several stable isotopes. β-tin (or white tin) exists at about 13.2°C and above. Below 13°C, it is α-tin (or grey tin) instead. White tin has a tetragonal structure and a density of 7.31g/cm^3, while grey tin has a diamond cubic structure and a density of 5.77g/cm^3. Hence significant volume expansion is involved during the β-to-α tin allotropic transition upon cooling, which induces a high internal stress and thus tin breaks down into smaller pieces (Di Maio and Hunt 2009). This phenomenon is traditionally known as tin pest or tin disease and may be utilized to realize cooling induced softening.

Sigma-Aldrich 520373-100G tin powder with a nominal size of 10 μm was selected as the transition component. Since the melting temperature of tin is at above 230°C, instead of Sylgard 184 silicone that was previously used, Dow Corning 736 Heat Resistant Sealant (HRS), a different type of silicone, which is developed for high temperature applications (for environmental temperatures up to 216°C and able to withstand higher temperatures up to 315°C for a short period), was selected as the elastic component. In addition, a volatile silicone fluid (SHIN-ETSU silicone fluid KF-995) was introduced into tin/HRS mixture to slow down the curing speed of HRS and in the mean time to modify the viscosity of mixture to achieve good dispersion of tin powders.

The fabrication procedure of HRS-tin hybrids is similar to that of previously discussed in other silicone based SMH systems. The major steps are briefly summarized as follows.

- Specified amounts of HRS, tin power and silicone fluid are mixed together and well stirred for a uniform dispersion of tin powder.

- The mixture is poured into a mould and then put into a vacuum chamber to remove entrapped air bubbles and also to evaporate silicone fluid.
- A fully cured sample (e.g., HRS-tin30, in which the volume fraction of tin is 30) is obtained after being kept in vacuum chamber for two days.

Figure 7.13 plots the DSC (DSC Q200, TA) result of HRS-tin30 at a heating/cooling ramp of 5°C/min between -35°C and 255°C. The melting temperature range and consolidation temperature range are revealed clearly in the heating and cooling curves, respectively. However, there is no evidence of the β-to-α tin allotropic transformation at all. This is due to that this transformation is a time-consuming process (in a time scale of days or above, but not within minutes as in current DSC test). This is because that the transformation from β-tin to α-tin involves nucleation and growth with an incubation time of months or even years.

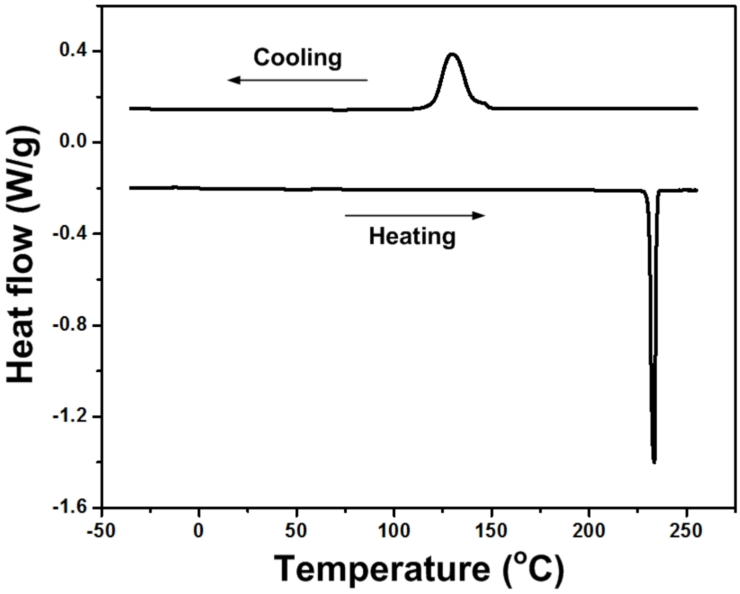

Figure 7.13 DSC result of HRS-tin30.

Figure 7.14 reveals the thermo-responsive SME in HRS-tin30 by both heating and cooling. Two pieces of straight HRS-tin30 (approximately 40×6×3 mm in dimension) were pre-bent at room temperature (we are able to do so because of high elasticity of HRS-tin30), and then heated to 240°C to fully melt tin with the constraint applied. After cooling down to room temperature and removing constraints, the samples were programmed into a curved shape as shown in Fig. 7.14(a_2) and (b_2). Upon heating (to 240°C) or cooling (by means of being kept in a freezer at -40°C for a week and then in liquid nitrogen of -196°C for 12 hours), both samples fully recovered their original straight shape (Fig. 7.14a_3 and b_2).

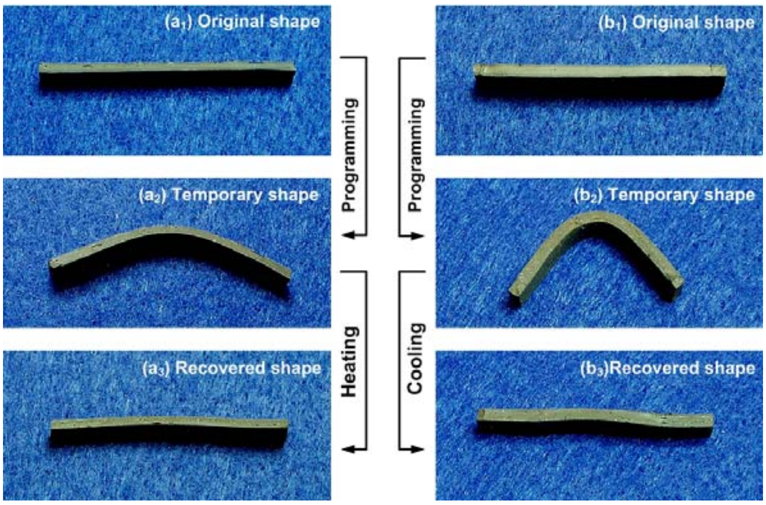

Figure 7.14 SME in HRS-tin30 SMH initiated by either heating (a) or cooling (b).

It should be pointed out that the transformation temperature from β-tin to α-tin is nominally at around 13.2°C, but it can be much lower if impurities, such as aluminum and zinc, exist. As such, in our experiment, we applied much lower cooling temperatures to speed up the transition. As reported in (Raynor and Smith 1958), the maximum growth rate is at around -40^{o}C. On the other hand, a high level of stress is induced due to a large volume change in β-tin to α-tin transition, and the growth of α-tin is also controlled by the relaxation stress in the β-α tin interface. Relaxation via dislocation motion, point defect creation, twinning or crack formation reduces this stress and thus speeds up the transition (Plumbridge 2007). Furthermore, the process of nucleation can be always expedited by seeding crystals which are similar to α-tin in structure (such as cadmium telluride, indium antimonide), or just simply by adding in α-tin (Styrkas 2003).

At present, the recovery temperature of most SMPs is less than 150^{o}C. Even for high temperature SMAs, it is less than 200^{o}C (Ma *et al.* 2010). Since the transition temperature of HRS-tin30 is as high as 230^{o}C, it has great potential for high temperature applications. We also notice very high hysteresis (about 100^{o}C) in HRS-tin30, which is far larger than the conventional high-hysteresis SMAs (He *et al.* 2004).

7.5 Summary

In this chapter, we further demonstrate the flexibility and versatile in design and fabrication of SMHs for tailored properties through a few examples. Based on the working principle of SMHs, electrically conductive SMHs which are suitable for joule heating and are with the over-heating protection function, SMHs with a narrow transition temperature range (within 4.5^{o}C), real pressure-responsive SMHs, high temperature SMHs, and heating/cooling-responsive SMHs are developed and characterized. As we can see, the performance of these SMHs can be well predicated even in the early design stage, due to the advantages in concept of SMHs.

Chapter 8 Conclusions and Future Works

8.1 Conclusions

An extensive literature review about shape memory materials (SMMs), in particular shape memory polymers (SMPs), is presented. The underline mechanisms behind different types of shape memory phenomena, particularly for thermo-responsive SMPs, and their thermo-mechanical characteristics are discussed. Some important issues of current SMPs for further development are identified.

Based on the similar working principle of dual-component SMPs, a new type of SMM, namely shape memory hybrid (SMH), is proposed and demonstrated in a few silicone based systems. The simple fabrication process and a wide selection range of component materials enable the design and fabrication of a particular SMH for a particular application turning out to be a rather conventional routine, which is accessible to ordinary engineers, even without any relevant background knowledge and experience. Since the SMH is made of conventional materials, which properties are well-known, the performance of the resulted SMH can be well-predicated in the pre-design stage.

In addition,

(1) The underlying mechanism behind the SME in SMHs was discussed schematically and then investigated by mean of numerical simulation (via finite element analysis).

The conditions to achieve good SME in SMHs were obtained. The influence of the volume fraction of transition component on shape fixity ratio, shape recovery ratio, maximum programming stress and shape recovery stress were studied.

(2) All types of shape memory phenomena, namely dual-SME, triple-SME, and mechanical two-way SME, which most likely can be found separately in some individual current SMP systems but not all in one, were reproduced in the S-PW based SMH system. The mechanisms behind these phenomena were investigated in details and verified by various experiments (including DSC, DMA and SEM etc). The dual-SME in S-PWs was systematically characterized, which helps us to have a better understanding of the SME in SMHs and can serve as a generic guide in design and development of other types of SMHs.

(3) Multiple-stimuli-responsive SME was demonstrated in the S-SAT hybrid system. As reported, shape recovery could be triggered by not only heat (thermo-responsive) and water (water-responsive), but also pressure (pressure-responsive). In addition, we showed that shape fixation of S-SAT hybrids could also be achieved by means of tapping instead of following conventional thermo-mechanical programming in conventional thermo-responsive SMPs/SMHs. Two-way reversible actuation (mechanical two-way SME) was also realized in this hybrid system.

(4) Besides the SME, rubber-like and self healing features were achieved in a S-MG hybrid system. We showed that S-MG hybrids are rubber-like at both high and low temperatures, and have excellent SME and repeated instant self-healing function. The mechanisms behind these features were clearly identified. It has been proved that while following the well-understood mechanism in SMHs, micro sized MG

inclusions play a part in the SME, tangled polymer chains of MG (and silicone) contribute to the rubber-like phenomenon and repeated instant self-healing function. The miscible MG within silicone provides a wonderful mechanism to simultaneously realize high elasticity, shape recovery and instant repeated self-healing.

(5) We further demonstrated the flexibility and versatile in design and fabrication of SMHs for tailored properties through a few examples. Based on the working principle of SMHs, electrically conductive SMHs which are suitable for joule heating and with over-heating protection function, SMHs with a narrow transition temperature range (within 4.5^{o}C), real pressure-responsive SMHs, high temperature SMHs, and heating/cooling-responsive SMHs were developed. As we can see, the performance of these SMHs can be well predicated even in the early design stage, due to the advantages in concept of SMHs.

With the achievements in SMHs reported here, we are ready to compare the characteristics of SMA, SMP and SMH. Some important properties/features of them are summarized and compared in Tab. 8.1, where texts highlighted in grey background indicate that the corresponding property is excellent. As we can see, while SMA and SMP have some their own advantages, both of them have some intrinsic deficiencies. In contrast, SMH can achieve excellence in all aspects as compared with SMA and SMP, and even have some functions/features that neither SMA nor SMP can provide.

Table 8.1 Comparison of major features of SMA, SMP and SMH.

	SMA	SMP	SMH
Recoverable strain	low	high	tunable
Recovery stress	high	low	tunable
Recovery speed	high	low	tunable
Multiple-SME	difficult	yes	easy
Two-way SME	easy	difficult	yes
Narrow transition temperature range	difficult	difficult	yes
High transition temperature	easy	difficult	yes
Multiple-stimuli-responsive	difficult	yes	easy
Color change	difficult	yes	yes
High electrical conductivity	easy	yes	yes
High electrical insulation	no	easy	easy
Fabrication/processing	difficult	easy	easy
Cost	high	low	low
Density	high	low	tunable

8.2 Future works

As mentioned in Huang et al (2011) and Toensmeier(Toensmeier 2005) (2005), SMMs are reshaping product design in many ways. Given the flexibility and versatile, SMHs, which may be regarded as a great expansion/extension of SMPs, from within polymeric materials only to far beyond virtually without any limit at all, not only emerge just in the right time, but also add in a new dimension in terms of applications of SMMs.

We have demonstrated that SMHs are able to achieve what other SMMs may have many difficulties to realize. In addition, SMHs can be designed and fabricated in a do-it-yourself (DIY) manner for tailored features and functions by even non-professionals.

However, what revealed here is merely a tiny portion, but not the full potential of SMHs. There are a lot to further explore. A few important directions for future investigation are listed as follows.

(1) Wireless/contactless remote-controllable SMH

By selecting transition components which are sensitive to some particular stimuli, such as light (either visible or invisible), magnetic/electrical field, wireless/ contactless remote-control can be achieved. Such materials are very much useful in medical operations, in particular for minimally invasive surgery. Surgical stents, sutures, staples and screws, et al with self-tightening/fixing/retraction can be developed based on such SMHs.

(2) Metal/ceramic/bioplastic based SMH

What we have presented here are mainly silicone based SMHs, in which highly elastic silicone is chosen as the elastic component. Based on the concept of SMH, we can also select other types of materials, not only other polymers, but also metal and ceramic, for either the elastic component or the transition component or both of them for a SMH. Ceramic based SMH may be used in very high temperature applications, while metal based SMHs may be applied in cases where high strength/stiffness and high actuation stress are required. Bioplastics, which are a form of plastics derived from renewable biomass sources, such as vegetable fats and oils, corn starch, pea starch, or microbiota, are future alternative to replace current petroleum based plastics. Bioplastic based SMHs are naturally biodegradable, so that they are environmental friendly.

(3) Biodegradable/recyclable SMH

Nowadays, biodegradable materials are highly in demand in order to keep our environment to be *green*. In addition to bioplastic based SMH that we have mentioned above, other types of biodegradable SMHs can be developed, particularly for biomedical applications. On the other hand, recyclable materials are widely to reduce our dependence on natural resources. Recyclable SMHs well fit this trend.

(4) SMH with additional functions

Additional function(s) is very important which adds in additional value and thus widens the range of applications. Self-healing SMH reported in Chapter 6 is a good example. High strength/stiffness and high recovery strength SMH may be developed using metals or metallic composites.

(5) Micro/nano sized SMH

Micro/nano sized SMH, in which protein and/or DNA may be used as components, can be developed for, for instance targeted drug release, and cellular surgery etc.

(6) Stability and modeling

The stability (both long term stability and stability in cyclic actuation) of SMHs is an important concern in many applications. Thermo-mechanical modeling is also required for optimization to achieve enhance performance.

Seemingly, the age of SMHs just starts. We expect to see a great expansion not only the size of SMH research community, but also the number of engineering applications of SMHs. The easy accessibility of SMHs should provide a great advantage over other SMMs, so that every interested person can design and fabricate his/her own SMH in a DIY manner, even just as a hobby.

Reference

Abhat A (1983). Low-Temperature Latent-Heat Thermal-Energy Storage - Heat-Storage Materials. Solar Energy 30(4), 313-332.

Abrahamson ER, Lake MS, Munshi NA, Gall K (2003). Shape memory mechanics of an elastic memory composite resin. Journal of Intelligent Material Systems and Structures 14(10), 623-632.

Agyenim F, Hewitt N, Eames P, Smyth M (2010). A review of materials, heat transfer and phase change problem formulation for latent heat thermal energy storage systems (LHTESS). Renewable & Sustainable Energy Reviews 14(2), 615-628.

Aschwanden M, Stemmer A (2006). Polymeric, electrically tunable diffraction grating based on artificial muscles. Optics Letters 31(17), 2610-2612.

Behl M, Bellin I, Kelch S, Wagermaier W, Lendlein A (2009). One-Step Process for Creating Triple-Shape Capability of AB Polymer Networks. Advanced Functional Materials 19(1), 102-108.

Bellin I, Kelch S, Langer R, Lendlein A (2006). Polymeric triple-shape materials. Proceedings of the National Academy of Sciences of the United States of America 103(48), 18043-18047.

Buckley PR, McKinley GH, Wilson TS, Small W, Benett WJ, Bearinger JP, McElfresh MW, Maitland DJ (2006). Inductively heated shape memory polymer for the magnetic actuation of medical devices. Ieee Transactions on Biomedical Engineering 53(10), 2075-2083.

Bueche F (1973). New Class of Switching Materials. Journal of Applied Physics 44(1), 532-533.

Burnworth M, Tang L, Kumpfer JR, Duncan AJ, Beyer FL, Fiore GL, Rowan SJ, Weder C (2011). Optically healable supramolecular polymers. Nature 472(7343), 334-337.

Chang LC, Read TA (1951). Plastic Deformation and Diffusionless Phase Changes in Metals - the Gold-Cadmium Beta-Phase. Journal of Metals 3(1), 47-52.

Chen SJ, Hu JL, Zhuo HT, Zhu Y (2008). Two-way shape memory effect in polymer laminates. Materials Letters 62(25), 4088-4090.

Chen XX, Dam MA, Ono K, Mal A, Shen HB, Nutt SR, Sheran K, Wudl F (2002). A thermally re-mendable cross-linked polymeric material. Science 295(5560), 1698-1702.

Chiodo JD, Billett EH, Harrison DJ Active disassembly using shape memory polymers for the mobile phone industry. In 'Proceedings of the 1999 IEEE International Symposium on Electronics and the Environment. ISEE-1999, 11-13 May 1999', 1999, Danvers, MA, USA, pp. 151-156

Cho JW, Kim JW, Jung YC, Goo NS (2005). Electroactive shape-memory polyurethane composites incorporating carbon nanotubes. Macromolecular Rapid Communications 26(5), 412-416.

Chung T, Rorno-Uribe A, Mather PT (2008). Two-way reversible shape memory in a semicrystalline network. Macromolecules 41(1), 184-192.

Cordier P, Tournilhac F, Soulié-Ziakovic C, Leibler L (2008). Self-healing and thermoreversible rubber from supramolecular assembly. Nature 451(7181), 977-980.

De Gennes PG (1971). Reptation of a polymer chain in the presence of fixed obstacles. The Journal of Chemical Physics 55(2), 572-579.

Di Maio D, Hunt CP (2009). Monitoring the Growth of the alpha Phase in Tin Alloys by Electrical Resistance Measurements. Journal of Electronic Materials 38(9), 1874-1880.

Dietsch B, Tong T (2007). A review - Features and benefits of shape memory polymers (SMPs). Journal of Advanced Materials 39(2), 3-12.

Dong JW, Xie JQ, Lu J, Adelmann C, Palmstrom CJ, Cui J, Pan Q, Shield TW, James RD, McKernan S (2004). Shape memory and ferromagnetic shape memory effects in single-crystal Ni2MnGa thin films. Journal of Applied Physics 95(5), 2593-2600.

Du HY, Zhang JH (2010). Solvent induced shape recovery of shape memory polymer based on chemically cross-linked poly(vinyl alcohol). Soft Matter 6(14), 3370-3376.

Fan K, Huang WM, Wang CC, Ding Z, Zhao Y, Purnawali H, Liew KC, Zheng LX (2011). Water-responsive shape memory hybrid: Design concept and demonstration. Express Polymer Letters 5(5), 409-416.

Feuchtwanger J, Asua E, Garcia-Arribas A, Etxebarria V, Barandiaran JM (2009). Ferromagnetic shape memory alloys for positioning with nanometric resolution. Applied Physics Letters 95(5).

Funakubo H (1987) 'Shape memory alloys.' (Gordon and Breach Science Publishers: New York)

Gojny FH, Wichmann MHG, Fiedler B, Kinloch IA, Bauhofer W, Windle AH, Schulte K (2006). Evaluation and identification of electrical and thermal conduction mechanisms in carbon nanotube/epoxy composites. Polymer 47(6), 2036-2045.

Gong JP (2010). Why are double network hydrogels so tough? Soft Matter 6(12), 2583-2590.

Guion J, Teisseire M (1991). Nucleation of Sodium-Acetate Trihydrate in Thermal Heat-Storage Cycles. Solar Energy 46(2), 97-100.

Gunes IS, Jana SC (2008). Shape memory polymers and their nanocomposites: A review of science and technology of new multifunctional materials. Journal of Nanoscience and Nanotechnology 8(4), 1616-1637.

Haertling GH (1999). Ferroelectric ceramics: History and technology. Journal of the American Ceramic Society 82(4), 797-818.

Havens E, Snyder EA, Tong TH (2005). Light-activated shape memory polymers and associated applications. Smart Structures and Materials 2005: Industrial and Commercial Applications of Smart Structures Technologies 5762, 48-55.

Hayashi S (1990). Technical report on preliminary investigation of shape memory polymers. Nagoya research and development center, Mitsubishi Heavy Industries Inc., Japan.

He XM, Rong LJ, Yan DS, Li YY (2004). TiNiNb wide hysteresis shape memory alloy with low niobium content. Materials Science and Engineering A 371(1-2), 193-197.

He Z, Satarkar N, Xie T, Cheng YT, Hilt JZ (2011). Remote controlled multishape polymer nanocomposites with selective radiofrequency actuations. Advanced Materials 23(28), 3192-3196.

Huang W (1999). Two-way behaviour of a nitinol torsion bar. Smart Structures and Materials 1999: Smart Materials Technologies 3675, 284-294.

Huang W (2002). On the selection of shape memory alloys for actuators. Materials & Design 23(1), 11-19.

Huang W, Toh W (2000). Training two-way shape memory alloy by reheat treatment. Journal of Materials Science Letters 19(17), 1549-1550.

Huang WM, Bin Y, Fu YQ (2011) 'Polyurethane Shape Memory Polymers.' (Taylor and Francis)

Huang WM, Ding Z, Wang CC, Wei J, Zhao Y, Purnawali H (2010a). Shape memory materials. Materials Today 13(7-8), 44-51.

Huang WM, Lee CW, Teo HP (2006). Thermomechanical behavior of a polyurethane shape memory polymer foam. Journal of Intelligent Material Systems and Structures 17(8-9), 753-760.

Huang WM, Liu QY, He LM, Yeo JH (2004). Micro NiTi-Si cantilever with three stable positions. Sensors and Actuators a-Physical 114(1), 118-122.

Huang WM, Yang B, An L, Li C, Chan YS (2005). Water-driven programmable polyurethane shape memory polymer: Demonstration and mechanism. Applied Physics Letters 86(11).

Huang WM, Yang B, Zhao Y, Ding Z (2010b). Thermo-moisture responsive polyurethane shape-memory polymer and composites: a review. Journal of Materials Chemistry 20(17), 3367-3381.

Jiang HY, Kelch S, Lendlein A (2006). Polymers move in response to light. Advanced Materials 18(11), 1471-1475.

Kersey FR, Loveless DM, Craig SL (2007). A hybrid polymer gel with controlled rates of cross-link rupture and self-repair. Journal of the Royal Society Interface 4(13), 373-380.

Kim BK (2008). Shape memory polymers and their future developments. Express Polymer Letters 2(9), 614-614.

Kirkby EL, Michaud VJ, Manson JAE, Sottos NR, White SR (2009). Performance of self-healing epoxy with microencapsulated healing agent and shape memory alloy wires. Polymer 50(23), 5533-5538.

Klimek L, Pietrzyk B (2004). Electron backscatter diffraction as a useful method for alloys microstructure characterization. Journal of Alloys and Compounds 382(1-2), 17-23.

Koerner H, Price G, Pearce NA, Alexander M, Vaia RA (2004). Remotely actuated polymer nanocomposites - stress-recovery of carbon-nanotube-filled thermoplastic elastomers. Nature Materials 3(2), 115-120.

Krupa I, Mikova G, Luyt AS (2007). Phase change materials based on low-density polyethylene/paraffin wax blends. European Polymer Journal 43(11), 4695-4705.

Kudva JN, Sanders B, Pinkerton-Florance J, Garcia E Overview of the DARPA/AFRL/NASA Smart Wing Phase 2 program. In 'Smart Structures and Materials 2001-Industrial and Commercial Applications of Smart Structures Technologies-, March 5, 2001 - March 8, 2001', 2001, Newport Beach, CA, United states, pp. 383-389

Kunzelman J, Chung T, Mather PT, Weder C (2008). Shape memory polymers with built-in threshold temperature sensors. Journal of Materials Chemistry 18(10), 1082-1086.

Lagoudas DC (2008) 'Shape memory alloys modeling and engineering applications.' (Springer: New York; London)

Lee HM, Jo YJ, Y. H., Jung I, Choi CS, Kim I (2011). Synthesis and characterization of low temperature Sn nanoparticles for the fabrication of highly conductive ink. Nanotechnology 22(22).

Lee KM, Knight PT, Chung T, Mather PT (2008). Polycaprolactone-POSS chemical/physical double networks. Macromolecules 41(13), 4730-4738.

Lendlein A (2010) 'Shape-Memory Polymers.' (Springer-Verlag Berlin Heidelberg: Berlin, Heidelberg)

Lendlein A, Behl M, Hiebl B, Wischke C (2010). Shape-memory polymers as a technology platform for biomedical applications. Expert Review of Medical Devices 7(3), 357-379.

Lendlein A, Jiang HY, Junger O, Langer R (2005). Light-induced shape-memory polymers. Nature 434(7035), 879-882.

Lendlein A, Kelch S (2002). Shape-memory polymers. Angewandte Chemie-International Edition 41(12), 2034-2057.

Lendlein A, Langer R (2002). Biodegradable, elastic shape-memory polymers for potential biomedical applications. Science 296(5573), 1673-1676.

Leng J, Du S (2010) 'Shape-memory polymers and multifunctional composites.' (CRC Press/Taylor & Francis: Boca Raton)

Leng JS, Huang WM, Lan X, Liu YJ, Du SY (2008a). Significantly reducing electrical resistivity by forming conductive Ni chains in a polyurethane shape-memory polymer/carbon-black composite. Applied Physics Letters 92(20).

Leng JS, Lan X, Liu YJ, Du SY, Huang WM, Liu N, Phee SJ, Yuan Q (2008b). Electrical conductivity of thermoresponsive shape-memory polymer with embedded micron sized Ni powder chains. Applied Physics Letters 92(1).

Li FK, Zhu W, Zhang X, Zhao CT, Xu M (1999). Shape memory effect of ethylene-vinyl acetate copolymers. Journal of Applied Polymer Science 71(7), 1063-1070.

Li Y, Hu ZB, Chen YY (1997). Shape memory gels made by the modulated gel technology. Journal of Applied Polymer Science 63(9), 1173-1178.

Liang C, Rogers CA, Malafeew E (1997). Investigation of shape memory polymers and their hybrid composites. Journal of Intelligent Material Systems and Structures 8(4), 380-386.

Lin CZ, Guo LJ (2007). Experimental study of drop deformation and breakup in simple shear flows. Chinese Journal of Chemical Engineering 15(1), 1-5.

Lin HC, Wu SK (1992). Strengthening Effect on Shape Recovery Characteristic of the Equiatomic Tini Alloy. Scripta Metallurgica Et Materialia 26(1), 59-62.

Liu C, Mather PT High thermal conductivity shape memory polymers. In 'ANTEC 2004 - Annual Technical Conference Proceedings, May 16, 2004 - May 20, 2004', 2004, Chicago, IL., United states, pp. 3080-3084

Liu C, Qin H, Mather PT (2007). Review of progress in shape-memory polymers. Journal of Materials Chemistry 17(16), 1543-1558.

Liu FS, Ding Z, Li Y, Xu HB (2005). Phase transformation behaviors and mechanical properties of TiNiMo shape memory alloys. Intermetallics 13(3-4), 357-360.

Liu YN, Tan GS (2000). Effect of deformation by stress-induced martensitic transformation on the transformation behaviour of NiTi. Intermetallics 8(1), 67-75.

Luo X, Mather PT (2009). Preparation and characterization of shape memory elastomeric composites. Macromolecules 42(19), 7251-7253.

Luo X, Mather PT (2010). Triple-shape polymeric composites (TSPCs). Advanced Functional Materials 20(16), 2649-2656.

Luyt AS, Krupa I (2008). Thermal behaviour of low and high molecular weight paraffin waxes used for designing phase change materials. Thermochimica Acta 467(1-2), 117-120.

Ma J, Karaman I, Noebe RD (2010). High temperature shape memory alloys. International Materials Reviews 55(5), 257-315.

Mabe JH, Calkins FT, Butler GW Boeing's variable geometry Chevron, morphing aerostructure for jet noise reduction. In '47th AIAA/ASME/ASCE/AHS/ASC Structures, Structural Dynamics and Materials Conference, May 1, 2006 - May 4, 2006', 2006, Newport, RI, United states, pp. 6457-6475

Mahmud AS, Liu YN, Nam TH (2008). Gradient anneal of functionally graded NiTi. Smart Materials & Structures 17(1).

Maitland DJ, Metzger MF, Schumann D, Lee A, Wilson TS (2002). Photothermal properties of shape memory polymer micro-actuators for treating stroke. Lasers in Surgery and Medicine 30(1), 1-11.

Maitland DJ, Small Iv W, Singhal P, Hwang W, Rodriguez JN, Clubb F, Wilson TS Design and realization of biomedical devices based on shape memory polymers. In '2009 MRS Spring Meeting, April 14, 2009 - April 17, 2009', 2009, San Francisco, CA, United states, pp. 79-91

Mather PT, Chung T, Rorno-Uribe A (2008). Two-way reversible shape memory in a semicrystalline network. Macromolecules 41(1), 184-192.

Mather PT, Luo XF, Rousseau IA (2009). Shape Memory Polymer Research. Annual Review of Materials Research 39, 445-471.

Mather PT, Qin HH (2009). Combined One-Way and Two-Way Shape Memory in a Glass-Forming Nematic Network. Macromolecules 42(1), 273-280.

Michaeli W, Pfefferkorn T (2006). Material and processing behaviour of thermoplastics filled with low melting metals. Plastics, Rubber and Composites 35(9), 380-386.

Mighri F, Huneault MA (2006). In situ visualization of drop deformation, erosion, and breakup in high viscosity ratio polymeric systems under high shearing stress conditions. Journal of Applied Polymer Science 100(4), 2582-2591.

Mitsumata T, Gong JP, Osada Y (2001). Shape memory functions and motility of amphiphilic polymer gels. Polymers for Advanced Technologies 12(1-2), 136-150.

Miyazaki S, Fu YQ, Huang WM (2009) 'Thin Film Shape Memory Alloys Fundamentals and Device Applications.' (Cambridge University Press: Leiden)

Mohr R, Kratz K, Weigel T, Lucka-Gabor M, Moneke M, Lendlein A (2006). Initiation of shape-memory effect by inductive heating of magnetic nanoparticles in thermoplastic polymers. Proceedings of the National Academy of Sciences of the United States of America 103(10), 3540-3545.

Naumann R, Emons HH (1989). Results of Thermal-Analysis for Investigation of Salt Hydrates as Latent Heat-Storage Materials. Journal of Thermal Analysis 35(3), 1009-1031.

Osada Y, Matsuda A (1995). Shape-Memory in Hydrogels. Nature 376(6537), 219-219.

Osada Y, Okuzaki H, Hori H (1992). A Polymer Gel with Electrically Driven Motility. Nature 355(6357), 242-244.

Ota S (1981). Current Status of Irradiated Heat-Shrinkable Tubing in Japan. Radiation Physics and Chemistry 18(1-2), 81-87.

Otsuka K, Ren XB (1999). Recent developments in the research of shape memory alloys. Intermetallics 7(5), 511-528.

Plumbridge WJ (2007). Tin pest issues in lead-free electronic solders. Journal of Materials Science-Materials in Electronics 18(1-3), 307-318.

Pretsch T (2010). Triple-shape properties of a thermoresponsive poly(ester urethane). Smart Materials & Structures 19(1).

Ratna D, Karger-Kocsis J (2008). Recent advances in shape memory polymers and composites: a review. Journal of Materials Science 43(1), 254-269.

Raynor GV, Smith RW (1958). The Transition Temperature of the Transition between Grey and White Tin. Proceedings of the Royal Society of London Series a-Mathematical and Physical Sciences 244(1236), 101-109.

Razzaq MY, Anhalt M, Frormann L, Weidenfeller B (2007). Thermal, electrical and magnetic studies of magnetite filled polyurethane shape memory polymers. Materials Science and Engineering A 444(1-2), 227-235.

Ren X, Otsuka K (1997). Origin of rubber-like behaviour in metal alloys. Nature 389(6651), 579-582.

Rodriguez ED, Luo X, Mather PT (2011). Linear/network poly(-caprolactone) blends exhibiting shape memory assisted self-healing (SMASH). ACS Applied Materials and Interfaces 3(Compendex), 152-161.

Rousseau IA (2008). Challenges of Shape Memory Polymers: A Review of the Progress Toward Overcoming SMP's Limitations. Polymer Engineering and Science 48(11), 2075-2089.

Rousseau IA, Mather PT (2003). Shape memory effect exhibited by smectic-c liquid crystalline elastomers. Journal of the American Chemical Society 125(50), 15300-15301.

Schurch KE, Ashbee KHG (1977). A near perfect shape-memory ceramic material. Nature 266(5604), 706-707.

Sepe MP (1998) 'Dynamic mechanical analysis for plastics engineering.' (Plastics Design Library: Norwich, N.Y.)

Sijbesma RP, Beijer FH, Brunsveld L, Folmer BJB, Hirschberg JHKK, Lange RFM, Lowe JKL, Meijer EW (1997). Reversible polymers formed from self-complementary monomers using quadruple hydrogen bonding. Science 278(5343), 1601-1604.

Sivakova S, Bohnsack DA, Mackay ME, Suwanmala P, Rowan SJ (2005). Utilization of a combination of weak hydrogen-bonding interactions and phase segregation to yield highly thermosensitive supramolecular polymers. Journal of the American Chemical Society 127(51), 18202-18211.

Small Iv W, Metzger MF, Wilson TS, Maitland DJ (2005). Laser-activated shape memory polymer microactuator for thrombus removal following ischemic stroke: Preliminary in vitro analysis. IEEE Journal on Selected Topics in Quantum Electronics 11(4), 892-901.

Small W, Singhal P, Wilson TS, Maitland DJ (2010). Biomedical applications of thermally activated shape memory polymers. Journal of Materials Chemistry 20(17), 3356-3366.

Styrkas AD (2003). Mechanisms of the allotropic transition of Sn. Inorganic Materials 39(8), 806-810.

Sun L, Huang WM (2010). Mechanisms of the multi-shape memory effect and temperature memory effect in shape memory polymers. Soft Matter 6(18), 4403-4406.

Sun L, Huang WM, Ding Z, Zhao Y, Wang CC, Purnawali H, Tang C (2012). Stimulus-responsive shape memory materials: A review. Materials & Design 33, 577-640.

Sun L, Huang WM, Wang CC, Zhao Y, Ding Z, Purnawali H (2011). Optimization of the shape memory effect in shape memory polymers. Journal of Polymer Science, Part A: Polymer Chemistry 49(16), 3574-3581.

Sutou Y, Kainuma R, Ishida K (1999). Effect of alloying elements on the shape memory properties of ductile Cu-Al-Mn alloys. Materials Science and Engineering a-Structural Materials Properties Microstructure and Processing 273, 375-379.

Swain MV (1986). Shape Memory Behavior in Partially-Stabilized Zirconia Ceramics. Nature 322(6076), 234-236.

Thompson SA (2000). An overview of nickel-titanium alloys used in dentistry. International Endodontic Journal 33(4), 297-310.

Thongruang W, Spontak RJ, Balik CM (2002). Correlated electrical conductivity and mechanical property analysis of high-density polyethylene filled with graphite and carbon fiber. Polymer 43(8), 2279-2286.

Tobushi H, Matsui R, Hayashi S, Shimada D (2004). The influence of shape-holding conditions on shape recovery of polyurethane-shape memory polymer foams. Smart Materials & Structures 13(4), 881-887.

Tobushi H, Okumura K, Endo M, Hayashi S (2001). Thermomechanical properties of polyurethane-shape memory polymer foam. Journal of Intelligent Material Systems and Structures 12(4), 283-287.

Tobushi H, Pieczyska E, Ejiri Y, Sakuragi T (2009). Thermomechanical Properties of Shape-Memory Alloy and Polymer and Their Composites. Mechanics of Advanced Materials and Structures 16(3), 236-247.

Toensmeier PA (2005). Shape memory polymers reshape product design. Plastics Engineering 61(3), 10-11.

Toohey KS, Sottos NR, Lewis JA, Moore JS, White SR (2007). Self-healing materials with microvascular networks. Nature Materials 6(8), 581-585.

Varma-Nair M, Wesson JP, Wunderlich B (1989). The thermal properties of polysiloxanes poly(dimethyl siloxane) and poly(diethyl siloxane). Journal of Thermal Analysis 35(6), 1913-1939.

Wache HM, Tartakowska DJ, Hentrich A, Wagner MH (2003). Development of a polymer stent with shape memory effect as a drug delivery system. Journal of Materials Science-Materials in Medicine 14(2), 109-112.

Wang XF, Wang YL, Jin ZH (2002). Electrical conductivity characterization and variation of carbon fiber reinforced cement composite. Journal of Materials Science 37(1), 223-227.

Wei LL, Ohsasa K (2010). Supercooling and Solidification Behavior of Phase Change Material. Isij International 50(9), 1265-1269.

Wei ZG, Sandstrom R, Miyazaki S (1998a). Shape-memory materials and hybrid composites for smart systems - Part I Shape-memory materials. Journal of Materials Science 33(15), 3743-3762.

Wei ZG, Sandstrom R, Miyazaki S (1998b). Shape memory materials and hybrid composites for smart systems - Part II Shape-memory hybrid composites. Journal of Materials Science 33(15), 3763-3783.

White SR, Sottos NR, Geubelle PH, Moore JS, Kessler MR, Sriram SR, Brown EN, Viswanathan S (2001). Autonomic healing of polymer composites. Nature 409(6822), 794-797.

Wool RP (2008). Self-healing materials: A review. Soft Matter 4(Compendex), 400-418.

Wunderlich B (2000). Teaching thermal analysis of polymeric materials. Journal of Thermal Analysis and Calorimetry 59(1-2), 7-19.

Xi Y, Ishikawa H, Bin YZ, Matsuo M (2004). Positive temperature coefficient effect of LMWPE-UHMWPE blends filled with short carbon fibers. Carbon 42(8-9), 1699-1706.

Xie CY, Sen LW, Hsu TY (1996). Two-way shape memory effect in a NiAl-Fe alloy. Scripta Materialia 35(3), 345-348.

Xie T (2010). Tunable polymer multi-shape memory effect. Nature 464(7286), 267-270.

Xie T, Xiao XC, Cheng YT (2009). Revealing Triple-Shape Memory Effect by Polymer Bilayers. Macromolecular Rapid Communications 30(21), 1823-1827.

Xu HB, Ma YQ, Jiang CB (2003). A high-temperature shape-memory alloy Ni54Mn25Ga21. Applied Physics Letters 82(19), 3206-3208.

Xue LA, Dai SY, Li Z (2010). Biodegradable shape-memory block co-polymers for fast self-expandable stents. Biomaterials 31(32), 8132-8140.

Yang B (2007) Influence of moisture in polyurethane shape memory polymers and their electrical conductive composites. PhD Thesis, Nanyang Technological University, Singapore

Yang B, Huang WM, Li C, Chor JH (2005). Effects of moisture on the glass transition temperature of polyurethane shape memory polymer filled with nano-carbon powder. European Polymer Journal 41(5), 1123-1128.

Yang B, Huang WM, Li C, Lee CM, Li L (2004). On the effects of moisture in a polyurethane shape memory polymer. Smart Materials and Structures 13(1), 191-195.

Yang B, Huang WM, Li C, Li L (2006). Effects of moisture on the thermomechanical properties of a polyurethane shape memory polymer. Polymer 47(4), 1348-1356.

Yoshii Y, Kuraoka M, Sengoku K, Ohachi T (2002). Induction time and three-electrode current vs. voltage characteristics for electrical nucleation of concentrated solutions of sodium acetate trihydrate. Journal of Crystal Growth 237-239(1-4 I), 414-418.

Yuan YC, Yin T, Rong MZ, Zhang MQ (2008). Self healing in polymers and polymer composites. Concepts, realization and outlook: A review. Express Polymer Letters 2(4), 238-250.

Zalba B, Marín JM, Cabeza LF, Mehling H (2003). Review on thermal energy storage with phase change: Materials, heat transfer analysis and applications. Applied Thermal Engineering 23(3), 251-283.

Zhang CS, Ni QQ (2007). Bending behavior of shape memory polymer based laminates. Composite Structures 78(2), 153-161.

Zhang J, Feng SY (2003). Temperature effects of electrical resistivity of conductive silicone rubber filled with carbon blacks. Journal of Applied Polymer Science 90(14), 3889-3895.

Zhang JH, Du HY (2010). Solvent induced shape recovery of shape memory polymer based on chemically cross-linked poly(vinyl alcohol). Soft Matter 6(14), 3370-3376.

Zhang Y, Broekhuis AA, Picchioni F (2009). Thermally self-healing polymeric materials: The next step to recycling thermoset polymers? Macromolecules 42(6), 1906-1912.

Zhao Y, Wang CC, Huang WM, Purnawali H (2011). Buckling of poly(methyl methacrylate) in stimulus-responsive shape recovery. Applied Physics Letters 99(13), 131911-3.

Zheng XT, Zhou SB, Xiao Y, Yu XJ, Li XH, Wu PZ (2009). Shape memory effect of poly(D,L-lactide)/Fe3O4 nanocomposites by inductive heating of magnetite particles. Colloids and Surfaces B-Biointerfaces 71(1), 67-72.

Zhou W, Wang ZL (2007) 'Scanning microscopy for nanotechnology techniques and applications.' (Springer: New York; London)

Zhou YM, Xue DZ, Ding XD, Otsuka K, Sun J, Ren XB (2009). High temperature strain glass in Ti-50(Pd50-xCrx) alloy and the associated shape memory effect and superelasticity. Applied Physics Letters 95(15).

Zotzmann J, Behl M, Hofmann D, Lendlein A (2010). Reversible triple-shape effect of polymer networks containing polypentadecalactone- and poly(ε-caprolactone)-segments. Advanced Materials 22(31), 3424-3429.

Appendix

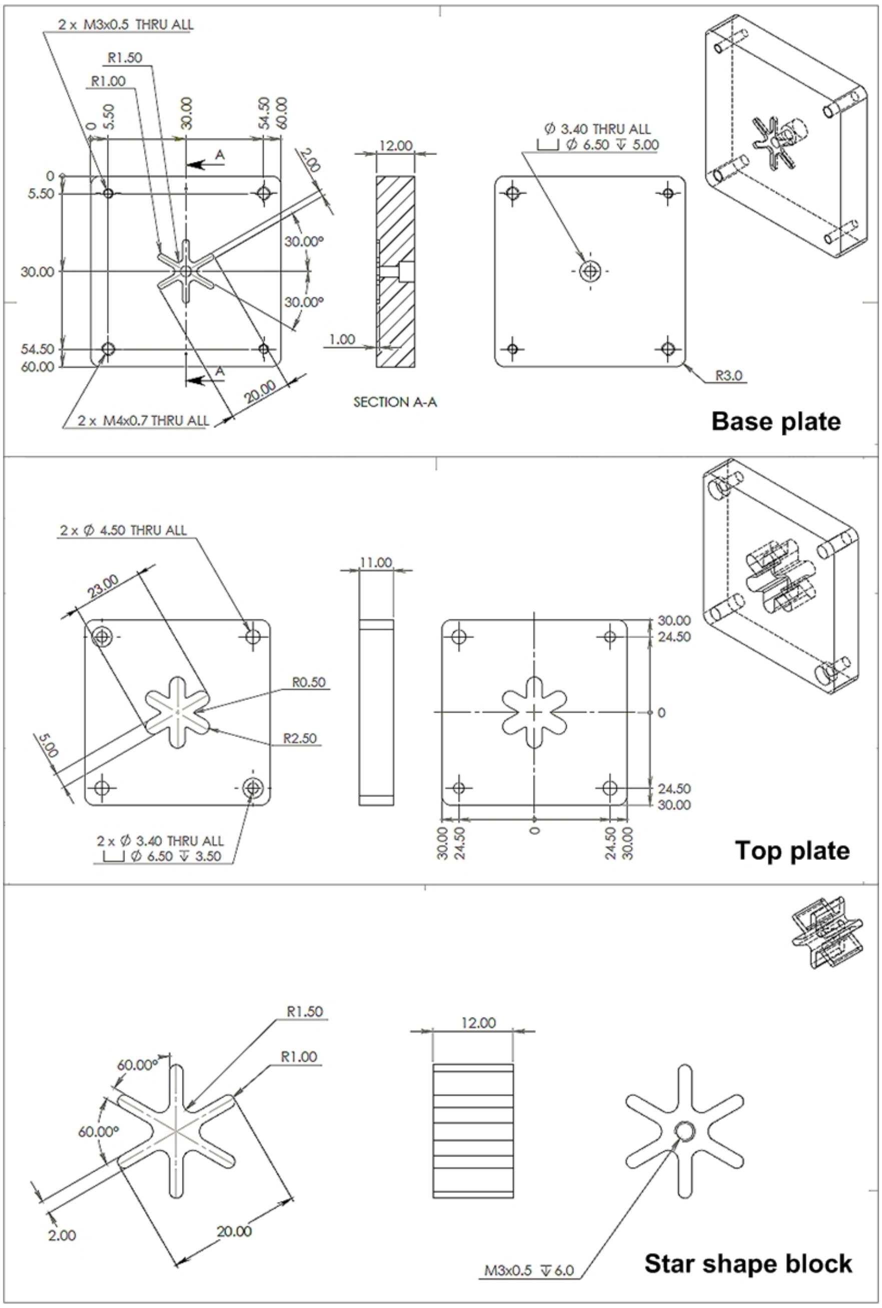

Figure A1 Design graph of star-shaped mold.

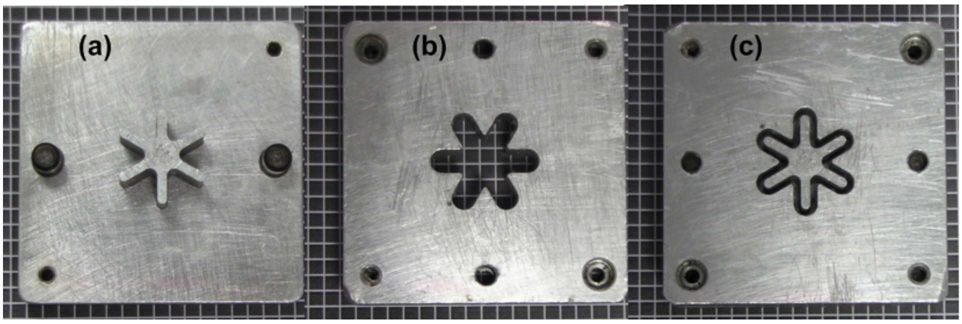

Figure A2 Images of star-shaped mold. (a) Bottom part, (b) top part, (c) assembled.

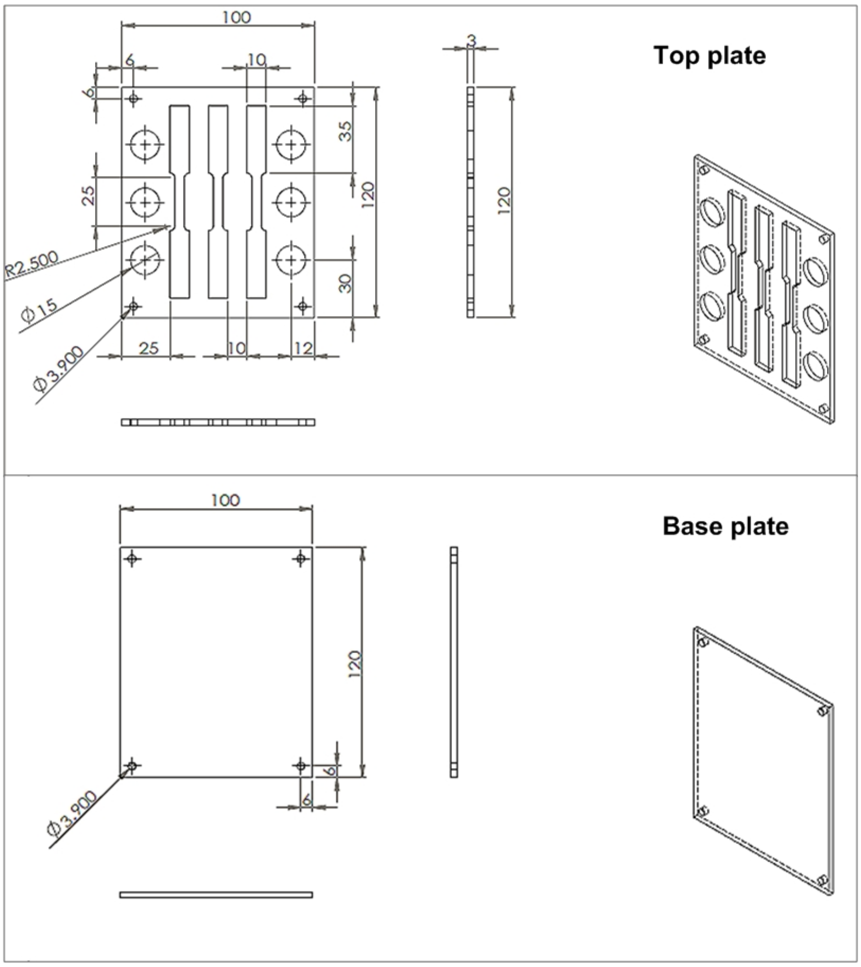

Figure A3 Design graph of dog-bone/round disk shaped mold.

Figure A4 Image of dog-bone/round disk shaped mold.

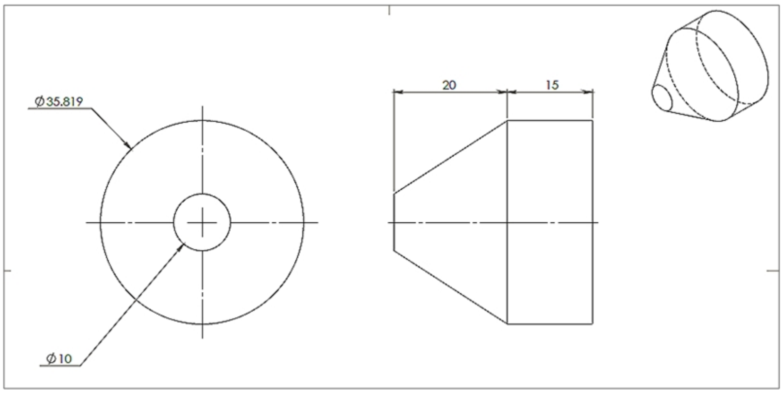

Figure A5 Design graph of shaft for expansion of star-shaped sample.

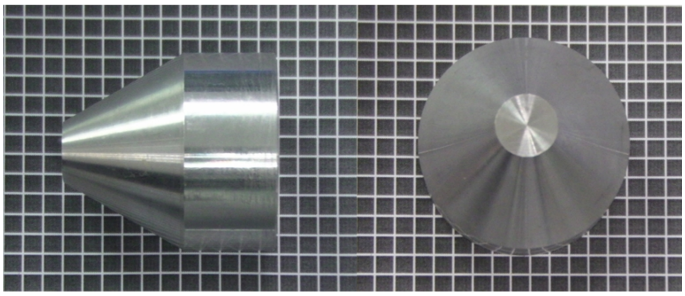

Figure A6 Images of shaft for expansion of star-shaped sample (side view and top view).

Publications

1. Huang WM, Ding Z, Wang CC, Wei J, Zhao Y, Purnawali H (2010). Shape memory materials. Materials Today 13(7-8), 44-51.
2. Sun L, Huang WM, Ding Z, Zhao Y, Wang CC, Purnawali H, Tang C (2012). Stimulus-responsive shape memory materials: A review. Materials & Design 33, 577-640.
3. Wang CC, Huang WM, Ding Z, Zhao Y, Purnawali H Cooling-/water-responsive shape memory hybrids. Composites Science and Technology, in press.
4. Fan K, Huang WM, Wang CC, Ding Z, Zhao Y, Purnawali H, Liew KC, Zheng LX (2011). Water-responsive shape memory hybrid: Design concept and demonstration. Express Polymer Letters 5(5), 409-416.
5. Sun L, Huang WM, Wang CC, Zhao Y, Ding Z, Purnawali H (2011). Optimization of the shape memory effect in shape memory polymers. Journal of Polymer Science, Part A: Polymer Chemistry 49(16), 3574-3581.
6. Huang WM, Yang B, Zhao Y, Ding Z (2010). Thermo-moisture responsive polyurethane shape-memory polymer and composites: a review. Journal of Materials Chemistry 20(17), 3367-3381.
7. Purnawali H, Xu WW, Zhao Y, Ding D, Wang CC, Huang WM and Fan H, Poly(methyl methacrylate) (PMMA) for active disassembly, Smart Materials and Structures, in press
8. Sun L, Huang WM, Lim CK, Ding Z, Purnawali H. Crack closure and shape restoration using NiTi shape-memory alloy. In '2011 International Conference on Civil Engineering and Building Materials, CEBM 2011, July 29, 2011 - July 31, 2011', 2011, Kunming, China, pp. 721-724